

POLITECNICO DI TORINO

SCUOLA DI DOTTORATO
Dottorato di Ricerca in Fluidodinamica - XXVII ciclo

PhD Dissertation

**A variable kinematic one-dimensional model for
aeroelasticity and dynamic analysis of multi-layered
rotors**



MATTEO FILIPPI

Tutor
Prof. Erasmo Carrera

PhD Coordinator
Prof. Gaetano Iuso

March 2015

*Alla mia Famiglia.
Ad Alessia.*

Ringraziamenti

Giunto al termine di un traguardo così importante mi sento in dovere di ringraziare tutti coloro che mi sono stati vicini. Un doveroso grazie va al Professor Erasmo Carrera che, con estrema professionalità e preparazione, mi ha giornalmente supportato e consigliato in questa attività di ricerca. Un sentito ringraziamento va a tutto il gruppo MUL²: Alfonso, Enrico, Marco, Mirella, Stefano, Tommaso, Alberto, Federico, Alessandro e Marianna. Grazie ragazzi! Per ultimi, ma non per importanza, un sentito grazie ai miei più cari amici Fabry, Sara, Rik, Raffy, Miky, Bax, Samu, Ettore, Massimo e Erika.

Abstract

Flutter is one of the most known instability phenomena. This condition occurs when a given structure exhibits sustained, harmonic oscillations, sometimes leading to catastrophic events. The prediction of flutter represents a crucial point for a correct and safe design. When fluid-structure interactions produce dynamic instability, flutter analyses require accurate descriptions of body deformations and aerodynamic loads. To this end, aerodynamic theories have been coupled with structural models to develop aeroelastic analysis tools, whose reliability is the results of a trade-off between the accuracy and the computational efficiency.

From a computational point of view, the most efficient formulation is based on the 1D assumption, where the problem is reduced to a set of variables that only depends on the beam-axis coordinate. Besides the well-known classical beam theories, several refined kinematic models have been proposed, to study the stability of rotating blades and shafts. However, when these structures are highly deformable or the material distribution involves non-classical structural couplings, 2D and 3D solutions are still required.

Within this work we propose an advanced 1D formulation to analyse the stability of rotating structures. The higher-order beam theories are obtained using the Carrera Unified Formulation (CUF), which allows to derive, at least theoretically, an infinite number of kinematic models. The Equations of Motion (EoM) for shafts and blades include the Coriolis term and the centrifugal effects (spin softening and geometrical stiffening). For the subsonic flow regime, aerodynamic loads are defined following the unsteady strip theories proposed by Theodorsen and Loewy. For the supersonic regime, the linear Piston theory is extended to structures rotating in compressed air flow. The Finite Element Method (FEM) is used to solve the weak form of the EoM.

Firstly, to evaluate the accuracy of 1D CUF elements, static and free-vibration analysis are carried out on compact and thin-walled structures of isotropic, orthotropic and functionally graded materials. Then, higher-order elements are used to study the dynamics of laminated shafts, thin cylinders, discs and blades, which rotate about the longitudinal and transverse axis. Results show the improved performance of the 1D CUF theories compared to 2D and 3D solutions.

In order to evaluate the proposed aeroelastic formulation, we test different wing configurations, including thin-walled box beams. The effects of the sweep angle and the lamination scheme on flutter conditions are evaluated, and results are compared with plate solutions, experimental tests and aeroelastic analysis carried out with the Doublet Lattice Method (DLM). Moreover, comparisons between Theodorsen and Loewy aerodynamic theories are presented

for a realistic rotary-wing model. In the last numerical examples, the linear Piston Theory is used to describe the dynamics of thin plates with different aspect-ratio surrounded by compressed air. For this cases, results are compared with an existing solution based on a non-linear plate theory.

Sommario

Il flutter è sicuramente il più conosciuto fenomeno di instabilità dinamica. Quando tale instabilità si verifica, la struttura presenta armoniche e auto-sostenute vibrazioni che, in casi sfortunati, possono provocare il collasso della stessa. La previsione della condizione di flutter è pertanto un punto cruciale per una corretta e sicura progettazione. Quando l'instabilità è dovuta ad interazioni tra la struttura e il flusso circostante, le analisi aerelastiche richiedono descrizioni accurate del campo di deformazione e delle distribuzioni di forze aerodinamiche a cui il corpo è assoggettato. A tal fine, teorie aerodinamiche e strutturali vengono accoppiate in modelli aeroelastici, le cui affidabilità sono il risultato di un compromesso tra l'accuratezza dei modelli e il loro effettivo costo computazionale.

L'approssimazione unidimensionale, certamente la più efficiente, prevede la riduzione del problema reale (definito in tre dimensioni) ad un set di variabili dipendenti da una solo parametro. La dinamica e la stabilità di alberi e superfici portanti in rotazione sono state largamente studiate con l'uso delle teorie trave, concepite secondo le classiche assunzioni di Eulero-Bernoulli e Timoshenko o basate su ipotesi cinematiche meno stringenti. Tuttavia, quando tali strutture sono altamente deformabili o la distribuzione del materiale causa accoppiamenti strutturali tra differenti modi di deformazione, ci si deve affidare alle soluzioni bi- e tridimensionali, con un conseguente aumento del costo computazionale.

Questa tesi si propone di fornire una formulazione 1D avanzata per lo studio della stabilità delle strutture rotanti in presenza o meno di un fluido circostante. Le teorie unidimensionali vengono concepite secondo la Carrera Unified Formulation (CUF), la quale consente di derivare un numero teoricamente infinito di modelli cinematici. Le equazioni del moto di alberi e travi rotanti includono, oltre al termine di Coriolis, lo 'spin softening' e la rigidità geometrica dovuta all'effetto centrifugo. I carichi aerodinamici in regime di flusso subsonico vengono definiti tramite le teorie instazionarie proposte da Theodorsen e Loewy. In regime supersonico, invece, le forze aerodinamiche agenti su piastre rotanti in un flusso di fluido compresso vengono calcolate secondo la 'piston theory' lineare. Le equazioni di governo vengono risolte con il metodo degli elementi finiti.

Al fine di valutare l'accuratezza degli elementi CUF 1D, numerose analisi statiche e di vibrazioni libere sono state effettuate su strutture in materiale isotropo, ortotropo e funzionalmente graduato. Successivamente, gli stessi elementi sono utilizzati per valutare la dinamica di una vasta gamma di strutture rotanti, comprendente alberi compatti laminati, cilindri e dischi sottili e pale. I risultati sono confrontati con soluzioni bi- e tridimensionali, confermando l'efficacia dell'approccio adottato.

Il modello aeroelastico proposto viene testato considerando diverse configurazioni alari, tra cui travi laminate in materiale ortotropo a parete sottile. Gli effetti dell'angolo di freccia e dello schema di laminazione sulle condizioni di flutter vengono attentamente analizzati. I risultati proposti sono confrontati con soluzioni bidimensionali, evidenze sperimentali e con valori ottenuti tramite l'impiego del Dou-

blet Lattice Method. Inoltre, viene studiata la risposta aeroelastica di una realistica pala di elicottero in rotazione tramite gli approcci instazionari di Theodorsen (esteso al caso rotante) e Loewy. Infine, è presentato lo studio aeroelastico di piastre rotanti in un flusso supersonico di aria compressa.

Contents

1	Introduction	13
1.1	Flutter and aeroelastic tools	13
1.2	Structural models for rotary-wings	15
1.3	Structural models for spinning shafts	16
1.4	Carrera Unified Formulation	18
2	Structural models	21
2.1	Preliminaries: geometry and material arrays	21
2.2	Carrera unified formulation	23
2.2.1	Equivalent-Single Layer Approach: ESL	23
2.2.2	The Layer-Wise Approach: LW	25
2.3	The Finite Element formulation	26
3	Carrera Unified Formulation in Rotordynamics	29
3.1	Hamilton's Principle and Lagrange's Equations	29
3.1.1	The structural stiffness matrix and the loading vector in CUF form	30
3.2	Dynamics of spinning structures	31
3.2.1	The Kinetic Energy	32
3.2.2	The Centrifugal Potential Energy	32
3.2.3	Stiffness and Damping due to bearings	34
3.2.4	The Equations of Motion	34
3.3	Dynamics of centrifugally stiffened structures	36
3.3.1	The Kinetic Energy	37
3.3.2	The Centrifugal Potential Energy	37
3.3.3	The Equations of Motion	37
4	Aeroelastic models	39
4.1	2-D steady and unsteady aerodynamic theories for fixed-wing	39
4.1.1	External work for the fixed-wing configuration	40
4.2	2-D unsteady aerodynamic theory for rotating lifting surfaces	41
4.2.1	External work for the rotary-wing configuration	43
4.3	Panel Flutter of rotating plates: Piston Theory	44
4.3.1	External work for a rotating structure	44
5	Numerical Results and discussion	47
5.1	Static Analyses	49
5.1.1	Laminated compact beams	51

5.1.2	Functionally Graded Structures	56
5.2	Free-Vibration Analyses	61
5.2.1	Laminated compact beams	61
5.2.2	The Functionally Graded cylinder	65
5.2.3	Thick metallic and composite cylinders	68
5.3	The spinning structures	74
5.3.1	Classical beam theories	74
5.3.2	Higher order beam theories for spinning composite shafts	78
5.3.3	Highly deformable spinning structures	86
5.4	The centrifugally stiffened structures	97
5.5	Flutter Analyses	102
5.5.1	Wing structures	102
5.5.2	Centrifugally stiffened beams	111
5.6	Rotating plates in a supersonic flow	116
6	Conclusions	123
6.1	Outline and contribution to the literature	123
6.2	Future works	125

Chapter 1

Introduction

According to Collar's definition, aeroelasticity is "the study of the mutual interaction that takes place within the triangle of the inertial, elastic, and aerodynamic forces acting on structural members exposed to an airstream, and the influence of this study on design". In the past, the fluid-structure interaction (FSI) has brought to catastrophic events due to sudden failures of bridges, airplanes, helicopters etc. A correct and safe design must require, therefore, an accurate prediction of aeroelastic phenomena. Unfortunately, FSI analyses are, in most cases, too computationally expensive, hence a trade off between accuracy and cost is often mandatory.

This thesis aims to present simple tools for the study of the dynamics and stability of shafts and blades. Simple aeroelastic formulations based on higher-order beam theories and unsteady strip approaches are proposed for flutter predictions.

1.1 Flutter and aeroelastic tools

Flutter is defined as the dynamic instability of an elastic body in an airstream that is subjected to large lateral aerodynamic loads and it is one of the most important aeroelastic phenomena. The flutter condition, defined by the critical speed (V_F) and by a circular frequency (ω_F) occurs when a given structure exhibits sustained, harmonic oscillations. In order to predict the borderline condition, it is paramount to know the interactions between elastic deformations and aerodynamic loads imposed by fluid motion. To this end, many aeroelastic theories have been developed. The aeroelastician usually needs information on two- and three-dimensional external flows and, in order to simplify the mathematical theories, a number of assumptions are usually made.

Fixed-wing aeroelasticity

A number of aerodynamic approaches was presented in the first half of the twentieth century by important aerodynamicists such as Cicala (Cicala, 1934-1935), Ellenberger (Ellenberger, 1936), Kussner (Kussner, 1936), Burgers with von Karman (von Karman and Burgers, 1943) and, in particular, Theodorsen (Theodorsen, 1935). The proposed strip theories and their modifications, properly combined with simplified structural models, have allowed simple but reliable tools to be developed. For instance, on the basis of beam-plate approach, in which the bending stiffness, the torsional stiffness and the secondary stiffnesses (bending-torsion, warping etc.) are reduced to the beam equivalent stiffnesses (EI , GJ , K etc.), wings (Guo et al., 2003, 2006; Qin

and Librescu, 1985) and bridge decks (Banerjee, 2003) were accurately studied. Unfortunately, this structural approach is no longer considered reliable when further couplings occur due to the distribution of the materials. For this reason, more refined theories have been developed. Over the years, Librescu *et al.* considered various aspects related to FSI such as divergence conditions of swept-forward wings (Librescu and Khdeir, 1988), effects of external stores (Gem and Librescu, 1998) and aeroelastic tailoring of composite structures (Gem and Librescu, 2000)-(Qin and Librescu, 2003) on both static and dynamic stability, the response to gust (Qin *et al.*, 2002) and blast loadings (Marzocca *et al.*, 2002). In most of these papers, the wing cross-section was either rectangular or biconvex, and the non-classical effects, such as warping deformations, transverse shear and non-uniform torsion were included in a sophisticated beam theory. Recently, the same structural model was used in (Ji-Seok *et al.*, 2013) and (Masjedi and Ovesy, 2014) where an attempt was made to suppress the instability and a number of interesting considerations on the different structural constitutive assumptions was presented, respectively. In particular, since the computation of the bending and torsional stiffnesses depends on the choice of the constitutive equations, Masjedi and Ovesy (2014) showed that the results of aeroelastic analyses can differ to a great extent, even as much as 40%. Moreover, other improvements were proposed by Patil *et al.* in (Cesnik *et al.*, 1996)-(Patil, 1997). The cross-sectional stiffnesses of composite box beams were first computed by means of an asymptotically correct formulation and then included in a non-linear beam modeling framework. The effectiveness of this approach was pointed out in (Palacios and Epureanu, 2011), where Palacios *et al.* dealt with the aeroelastic behaviour of highly flexible wings.

In the 1970s, the development of three dimensional aerodynamic panel/lifting surface methods enabled prediction of flutter conditions and gust responses of new structural configurations. For instance, the Doublet Lattice Method (DLM)(Albano and Rodden, 1969) and its refinements (Rodden *et al.*, 1998) were extensively used for the study of non-planar configurations (Kalman *et al.*, 1970), non-conventional planform shaped wings (Lan, 1979) and complex wing/tail interactions in both subsonic and supersonic flow (Yurkovich, 2003). Panel theories have been usually combined with bi-dimensional structural models for the description of the above complex structures. Nowadays, the rapid increase of the computational power has motivated the development in the area of computational fluid dynamics (CFD). Over the last 30 years, the CFD-based aeroelasticity progressed from full potential theories to problems governed by the Navier-Stokes equations. Recent works offer interesting overviews of CFD-aeroelastic tools (Bennet and Edwards, 1998; Huttshell *et al.*, 2001) furthermore providing useful information about the emerging trends in the aeroelasticity field (Livne, 2003). From a structural point of view, the CFD simulations can be coupled with finite element models, in which non-linear elements may be used in order to include either geometrical effects or large deformations. A detailed paper about non-linear structural models can be found in Demasi and Livne (2009).

Rotating blade aeroelasticity

As far as the aeroelasticity of rotary-wings is concerned, the basic problem becomes more complex due to the geometric nonlinearities that must be taken into account in both elastic and aerodynamic terms. This need has driven the development of suitable structural and aerodynamic theories as confirmed by the considerable number of articles available in the literature. Almost 50 years ago, Loewy (1969) provided a thorough overview on a wide range of topics related to the dynamics and aeroelasticity of rotary-wings such as flap-lag flutter, pitch-lag flut-

ter and ground and air resonance. Although being more limited in scope, other contributions on the study of classical flutter conditions and unsteady aerodynamic theories were proposed by Ham (1973) and Dat (1973), respectively. In that period, the aerodynamic models for the instability predictions were basically extensions of steady and quasi-steady strip theories conceived for fixed-wings. The first important rotary-wing unsteady approach for hover, based on Theodorsen's model, was proposed by Loewy (1957). Although in an approximate manner, this theory takes into account the effect of the spiral returning wake beneath the rotor. More details about Loewy's theory will be provided in next sections. Other valuable aerodynamic models were proposed on the basis of Greenberg's theory (Greenberg, 1947). According to this approach, a pulsating velocity variation and a constant pitch angle were included in Theodorsen's model. These modifications were extended to the case of rotary-wings by Friedmann and Yuan (1977), in which Theodorsen's theory, Loewy's theory for both incompressible and compressible flows and Possio's theory were used for the coupled flap-lag-torsional aeroelastic problem of a rotor blade in hover. The authors pointed out that the above modifications should be included to realistically reproduce the aeroelasticity of rotary-wings, where the assumptions commonly used in deriving strip theories (1 - cross sections are assumed to perform only simple harmonic pitching and plunging oscillations about a zero equilibrium position; 2 - the velocity of oncoming airflow is constant; 3 - usual potential small-disturbance unsteady aerodynamics are assumed to apply) are intrinsically violated. The modified strip theory with the quasi-steady approximation was used to study the stability of composite helicopter blades with swept tips both in hover and in forward flight (Yuan and Friedmann, 1995). The swept-tip blades were modeled by means of non-linear 1D finite element with the inclusion of transverse shear deformations and out-of-plane warping. These results were recently used to verify the accuracy of a nonlinear structural formulation valid for slender, homogeneous and twisted blades (Piccione et al., 2010). Other analyses on advanced geometry blades were carried out in (Bir and Chopra, 1994) with the purpose of evaluating the effects of sweep and droop on both rotor aeroelastic stability and rotorcraft aeromechanical stability. The evolution of the mechanics of helicopter blades, focusing on the aeroelastic and aerodynamic issues, was extensively discussed in (Conlisk, 1997; Friedmann, 2004; Friedmann and Hodges, 1977, 2003).

Although the aeroelasticity of large wind turbine blades is inherently different, several related aeroelastic problems were solved using rotary-wing theories (Friedmann, 1976; Kaza and C.E., 1976, May; Ormiston, 1973). Also in this case, interesting reviews are available (Friedmann, 1980; Hansen et al., 2006; Rasmussen et al., 2003), in which the response problems of an isolated wind turbine blade and a complete rotor/tower configuration were detailed discussed.

1.2 Structural models for rotary-wings

A thorough understanding of the dynamics of rotating blades is the starting point for the study of fatigue effects, forced-response and flutter instability, which occur in airplane engines, helicopters and turbomachinery. The modelling of rotating structures is usually made with beam formulations. Many researchers addressed the problem of the rotating beam by simplifying both equations of motion and displacement formulations. For instance, Banerjee (2000); Banerjee et al. (2006), Ozge and Kaya (2006), Mei (2008) and Hodges and Rutkowski (1981) limited their studies to the flexural vibrations of both uniform and tapered Euler-Bernoulli rotating beams using, respectively, the Dynamic Stiffness Method, the Differential Transform Method and a variable-order finite element approach. The assumption that the beam deforms only in bending mode is restrictive, since the coupling between the axial deformation and the lagwise

motion can be significant. To take into account this coupling the introduction of the Coriolis force becomes mandatory. For this reason, Huang et al. (2010) solved the complete motion equations of Euler beams using the power series solution, and the Finite Element Method (Tsai et al., 2011). Improvements were achieved with the introduction of enhanced displacement fields over the blade cross-section. Several studies were conducted on the development of theories for the rotating structures based on the Timoshenko model, where the Coriolis term was (Stoykov and Ribeiro, 2013) or was not considered (Banerjee, 2001; Lee and Kuo, 1993; Rao and Gupta, 2001; Yoo et al., 2005). In all these works, the generic rotating blade is assumed to be a compact structure constituted by isotropic material or by orthotropic laminae. However, the design of advanced rotor blades was strongly affected by the advent of composite materials, which combine a high specific strength and stiffness with simplified formability. These properties produce light and efficient blades, whose dynamic characteristics usually involve phenomena that cannot be detected by the use of classical models. For this reason, a considerable number of refined theories were introduced with the purpose of describing the rotating composite blade behaviour. For instance, Song *et al.* presented in (Song and Librescu, 1997b) a structural model encompassing transverse shear, secondary warping deriving from the assumption of the non-uniform torsion along the longitudinal axis and the effect of the heterogeneity of the materials. They observed that, by discarding the Coriolis term, the equations described separately the flap-lag deformation and the extension-twist motion, and within this context, they examined the ply orientation effects. Contrary to this ad-hoc formulation, Chandiramani et al. (2002) provided a geometrically nonlinear theory for analyzing the rotating composite thin-walled box beam, in which the non-classical effects were captured in a general way. The linearized equations of motion were solved with the Modified Galerkin Method and the Coriolis term was disregarded. Additionally, the authors extended their formulation to pre-twisted composite blades (Chandiramani et al., 2003). Interesting studies on controlling thin-walled composite blades via piezoelectric patches were presented in (Na et al., 2003; Song et al., 2002). Jung et al. (2001) developed a one-dimensional finite element based on a mixed variational approach in which both displacement and force formulations were used. The walls of the structures considered were modelled as shell and the global deformation was described by the Timoshenko beam model. This model is suitable for composite structures with open and closed contour. Detailed reviews about the dynamics of rotating composite blades are provided in (Hodges, 1990; Jung et al., 1999).

1.3 Structural models for spinning shafts

This section aims to provide an overview (even if not comprehensive) of structural theories used to analyse the dynamics of spinning structures.

The classical beam theory proposed by Euler and Bernoulli has been adopted by many researchers. For instance, Bauer (1980) presented an analytical approach to investigate the vibrational behaviour of a beam rotating with constant speed about its longitudinal axis for all boundary conditions. About ten years later, Chen and Liao (1991) used the assumed-modes approximate method to evaluate how the dynamic behavior of a rotating slender beam is affected by the ratio of moments of inertia of the cross-section and the pre-twisted angle. Furthermore, by using the same structural model, Banerjee and Su (2004) solved the differential equations of motion by extending the field of application of the Dynamic Stiffness Method (DSM) to rotating structures. Unfortunately, these solutions are inadequate for short and stubby bodies in which rotary inertia and shear deformations are important. In order to take into account these effects,

more refined theories have been widely employed. In fact, Zu and Han presented analytical solutions for free flexural vibrations of a spinning, finite Timoshenko beam subjected to a moving load for the six classical boundary conditions (Jean Wu-Zheng and P.S. Han, 1992). To consider elastic supports, Choi et al. (2000) presented an efficient and accurate quadrature method to investigate the dynamics of a spinning shearable beam. On the other hand, in the framework of DSM, Curti (Curti et al., 1991), (Curti et al., 1992) analyzed the vibrational behaviour of moderate thick shafts by adding rotatory inertia and shear deformation effects to Euler-Bernoulli's model. In (Sheu and Yang, 2005), the authors showed that both whirl and critical speeds can be analytically expressed as a function of a geometric parameter (slenderness ratio) of a Rayleigh beam. Furthermore, this parameter limits the number of critical speeds.

Several experimental tests demonstrated the advantages of orthotropic materials over their isotropic counterparts (Bauchau, 1981; Zinberg and Symmonds, 1970; Zorzi and Giordano, 1985). As a consequence, the design of rotors has demanded the development of adequate and reliable structural models. For instance, Bert and Kim developed one-dimensional models, based on Euler-Bernoulli (Bert and Kim, 1992) and Bresse-Timoshenko (Bert and Kim, 1995) theories, which included bending-twisting coupling. The critical speeds were in good agreement with the results obtained through both shell and experimental approaches. Naturally, when shear effects become important, results obtained with the Euler-Bernoulli theory are not accurate. In (Chen and Peng, 1998), the authors investigated the stability of composite spinning cylinders subjected to compressive loads using Timoshenko's model and the equivalent modulus beam theory (EMBT). Critical speeds and effects due to a disk location were also studied under these assumptions. Another contribution was made by Chang et al. (2004), who developed a simple first-order shear deformation theory for shafts supported by bearings modeled as springs and viscous dampers. The constitutive relations were derived directly from the equations of 3D continuum mechanics using coordinate transformations.

To overcome the limitations of the equivalent modulus approach, Singh and Gupta (1996) first proposed a refined beam formulation derived from a layerwise shell theory (LBT) and then, in (Gubran and Gupta, 2005), presented a modified EMBT that included bending-twisting, shear-normal and bending-stretching coupling effects. The obtained results were used by Sino et al. (2008) to assess their simplified homogenized beam theory (SHBT), where the stiffness parameters are evaluated using an energy formulation that takes into account several contributions, such as Young's modulus, the shear modulus, the distance from the shaft axis and the thickness of each rotor layer. The results were in good agreement with those presented by Gupta *et al.*. Other attempts have also been made to improve displacement theories. Among these formulations, Librescu *et al.* provided a higher order model which incorporates the warping and torsion of thin-walled anisotropic spinning structures. Critical speeds as well as stability were investigated considering thin-walled boxes (Song and Librescu, 1997a; Song et al., 2000) and cylinders (Na et al., 2006). When the assumptions of beam theories are too restrictive, two- and three-dimensional formulations become useful. For instance, in (Kim and Bert, 1993), the authors compared a number of shell theories (Loo's, Morley's, Love's, Donnell's and Sanders's theories) to determine the critical speeds of the shaft examined in (Zinberg and Symmonds, 1970). All these models yielded accurate results, except Donnell's theory, which was not effective for long shafts. Another example is (Ramezani and Ahmadian, 2009), in which the layerwise theory was combined with the Wave Propagation Approach for rotating laminated shells under different boundary conditions. Interesting results were presented in (Zhao et al., 2002), in which the dynamics of rotating cross-ply laminated cylinders was considered. The structure was reinforced with stringers and rings whose stiffness was considered either

separately or smeared over the shell surface. As expected, the number of stiffeners had a remarkable effect on the backward and forward frequencies. Moreover, in (Chatelet et al., 2002), a disk-shaft assembly was discretized with shell finite elements, considering a cyclic symmetry of the structure; three analyses were carried out with different numbers of degrees of freedom. This assumption allowed a considerable reduction of the computational cost. Comprehensive overviews of rotor dynamic phenomena and classical analysis approaches can be found in (Genta, 2005; Hua et al., 2005; Rao, 1985).

1.4 Carrera Unified Formulation

Carrera's Unified Formulation (CUF) offers a procedure to obtain refined structural models, in which the order and the type of theories are free input parameters. CUF was first developed for plate and shell theories. A comprehensive description of possible approaches for laminated plates and shells based on both displacement and transverse stress assumptions were provided in Carrera (2002, 2003). Later, Ballhause et al. (2004) investigated the static and dynamic behavior of multilayered plates embedding piezo-layers. The results show that CUF is able to lead to a quasi-3D description of the global and local characteristics of piezoelectric plates. Other assessments were presented in (Carrera, 2004), where the vibrational free response of homogeneous and multilayered simply supported plates was evaluated. Carrera et al. (2007) used CUF to analyze multi-field problems related to multilayered plates subjected to thermal, mechanical and electric loads. In (Carrera et al., 2008), same analyses were performed also considering a magnetic load. Moreover, Carrera and Giunta carried out failure analyses for simply supported, isotropic and orthotropic plates using the failure criteria developed by Von Mises (Carrera and Giunta, 2008), Tsai-Hu, Tsai-Hill, Hoffman and Hashin (Carrera and Giunta, 2009). Regarding functionally graded materials (FGM), Brischetto investigated plates subjected to a transverse mechanical load (Brischetto and Carrera, 2010) using CUF and Reissner's mixed variational theory. Within the same topic, Neves *et al.* provided static, free vibration and buckling analysis of FGM plates (Neves et al., 2012b) and shells (Neves et al., 2012a) by means of a meshless technique.

In the latest years, CUF has been extended to the beam model. Carrera and Giunta tested the performance of higher-order 1D theories, using N -order Taylor type expansions of the section coordinates in order to define the displacement variables (Carrera and Giunta, 2010). The study was carried out on isotropic beams with rectangular and I-shaped cross-sections and the governing differential equations were solved via Navier type closed-form solution. In (Carrera et al., Sept. 2009), displacement unknowns were expanded using N -order Lagrange polynomials, which were defined on a set of sampling points belonging to the section. Carrera et al. (2010a) analysed the static behavior of a beam with an airfoil-like section subjected to a bending load using Taylor-like elements. The authors demonstrated that the use of higher-order theories improves the flexibility of the beam element as well as the accuracy of the displacement, stress and strain distributions over the cross-section. Beam formulation was also employed to analyse the static behavior of thin-walled structures, bridge-like cross-sections (Carrera et al., 2012b), furthermore, to present buckling and static analyses of laminated composite beams (Ibrahim et al., 2012),(Catapano et al., 2011). As for the Taylor-like model, it has been shown that the number of terms that should be retained for each of the considered beam theories is closely related to the problem addressed. A comprehensive discussion of this issue is proposed by Carrera and Petrolo (2011a). As far as free-vibrational analyses are concerned, the dynamic characteristics of different beam sections and wing model are presented in (Carrera et al.,

2011b, 2012a; Petrolo et al., 2012). Other investigations have been carried out on hollow cylindrical reinforced structures (Carrera et al., 2013f), laminated composite (Giunta et al., 2013) and functionally graded beams (Giunta et al., 2011). Besides Taylor- and Lagrange-based expansions, several displacement theories obtained by means of combinations of different functions (trigonometric, exponential, hyperbolic etc.) have been recently tested on laminated structures made of either composite (Carrera et al., 2013b,d) or functionally graded (Daoud et al., 2014) materials. Other encouraging results have also been obtained in the rotordynamics field by analyzing both rotating blades (Carrera et al., 2013c) and spinning shafts (Carrera and Filippi, 2014; Carrera et al., 2013a) (some results are reported in this thesis). Regarding structure-fluid interactions, CUF elements have already been used with both Vortex (Carrera et al., 2013e; Varello et al., 2011, 2013) and Doublet (Pagani et al., 2014; Petrolo, 2012, 2013) Lattice method and, for supersonic flows, with the Piston theory (Carrera and Zappino, 2014b; Carrera et al., 2014c).

Many other papers exploit the features of CUF, but for a thorough and clear description we refer to (Carrera et al., 2014a, 2011a).

Chapter 2

Structural models

In this chapter, Carrera's Unified Formulation (CUF) is presented. This formulation allows, at least theoretically, the definition of an infinite number of structural theories going beyond the assumptions of the classical refined beam models. The number and the kind of functions used within the displacement field are input parameters of the formulation and determine the class of the 1D theory. A number of Equivalent-Single Layer (ESL) theories and the Layer-Wise (LW) approach are briefly discussed in the following.

2.1 Preliminaries: geometry and material arrays

We introduce the transposed displacement vector

$$\mathbf{u}(x, y, z) = \{ u_x \quad u_y \quad u_z \}^T \quad (2.1)$$

where x , y , and z are orthonormal axes, as shown in Fig.2.1. The cross-section of the structure

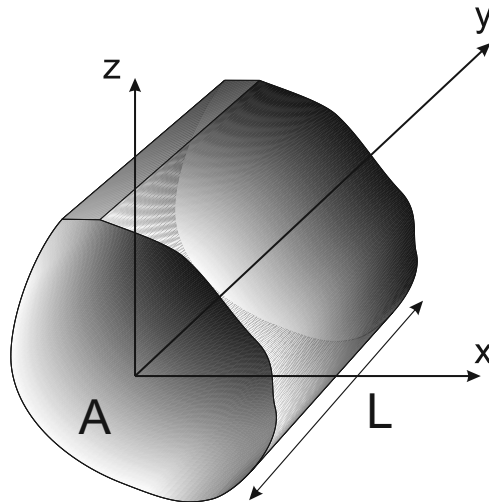


Figure 2.1 Structural reference system

is A and the longitudinal axis is $0 \leq y \leq L$. The stress, σ , and strain, ϵ , components are grouped as

$$\begin{aligned} \sigma_p &= \{ \sigma_{zz} \quad \sigma_{xx} \quad \sigma_{zx} \}^T, & \epsilon_p &= \{ \epsilon_{zz} \quad \epsilon_{xx} \quad \epsilon_{zx} \}^T \\ \sigma_n &= \{ \sigma_{zy} \quad \sigma_{xy} \quad \sigma_{yy} \}^T, & \epsilon_n &= \{ \epsilon_{zy} \quad \epsilon_{xy} \quad \epsilon_{yy} \}^T \end{aligned} \quad (2.2)$$

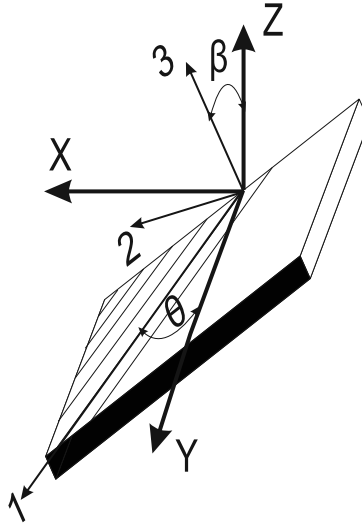


Figure 2.2 Physical and material reference system

The subscript "n" stands for those terms lying on the cross-section, while "p" stands for the terms lying on planes which are orthogonal to A.

The strains are obtained as

$$\begin{aligned}\epsilon_p &= D_p \mathbf{u} \\ \epsilon_n &= D_n \mathbf{u} = (D_{np} + D_{ny}) \mathbf{u}\end{aligned}\quad (2.3)$$

where D_p and D_n are differential operators whose explicit expressions are

$$D_p = \begin{bmatrix} 0 & 0 & \frac{\partial}{\partial z} \\ \frac{\partial}{\partial x} & 0 & 0 \\ \frac{\partial}{\partial z} & 0 & \frac{\partial}{\partial x} \end{bmatrix}, \quad D_{np} = \begin{bmatrix} 0 & \frac{\partial}{\partial z} & 0 \\ 0 & \frac{\partial}{\partial x} & 0 \\ 0 & 0 & 0 \end{bmatrix}, \quad D_{ny} = \begin{bmatrix} 0 & 0 & \frac{\partial}{\partial y} \\ \frac{\partial}{\partial y} & 0 & 0 \\ 0 & \frac{\partial}{\partial y} & 0 \end{bmatrix}\quad (2.4)$$

Constitutive laws are introduced to obtain the stress components,

$$\boldsymbol{\sigma} = \tilde{\mathbf{C}} \boldsymbol{\epsilon}\quad (2.5)$$

On the basis of Eq.s 2.2, the previous equation becomes

$$\begin{aligned}\sigma_p &= \tilde{\mathbf{C}}_{pp} \epsilon_p + \tilde{\mathbf{C}}_{pn} \epsilon_n \\ \sigma_n &= \tilde{\mathbf{C}}_{np} \epsilon_p + \tilde{\mathbf{C}}_{nn} \epsilon_n\end{aligned}\quad (2.6)$$

Both laminated box beams and cylinders can be considered constituted by a certain number of either straight or curved plates of orthotropic material, whose material coordinate systems (1,2,3) generally do not coincide with the physical coordinate system (x,y,z) (see Fig.2.2). Using this approach, the matrices of material coefficients of the generic material k are:

$$\tilde{\mathbf{C}}_{pp}^k = \begin{bmatrix} \tilde{C}_{11}^k & \tilde{C}_{12}^k & \tilde{C}_{14}^k \\ \tilde{C}_{12}^k & \tilde{C}_{22}^k & \tilde{C}_{24}^k \\ \tilde{C}_{14}^k & \tilde{C}_{24}^k & \tilde{C}_{44}^k \end{bmatrix}, \quad \tilde{\mathbf{C}}_{pn}^k = \begin{bmatrix} \tilde{C}_{15}^k & \tilde{C}_{16}^k & \tilde{C}_{13}^k \\ \tilde{C}_{25}^k & \tilde{C}_{26}^k & \tilde{C}_{23}^k \\ \tilde{C}_{45}^k & \tilde{C}_{46}^k & \tilde{C}_{43}^k \end{bmatrix}, \quad \tilde{\mathbf{C}}_{nn}^k = \begin{bmatrix} \tilde{C}_{55}^k & \tilde{C}_{56}^k & \tilde{C}_{35}^k \\ \tilde{C}_{56}^k & \tilde{C}_{66}^k & \tilde{C}_{36}^k \\ \tilde{C}_{35}^k & \tilde{C}_{36}^k & \tilde{C}_{33}^k \end{bmatrix}\quad (2.7)$$

On the other hand, for the FG materials (FGM), the matrices of material coefficients are

$$\tilde{\mathbf{C}}_{pp}^k = \begin{bmatrix} \tilde{C}_{11}^k & \tilde{C}_{12}^k & 0 \\ \tilde{C}_{12}^k & \tilde{C}_{22}^k & 0 \\ 0 & 0 & \tilde{C}_{66}^k \end{bmatrix}, \quad \tilde{\mathbf{C}}_{pn}^k = \begin{bmatrix} 0 & 0 & \tilde{C}_{13}^k \\ 0 & 0 & \tilde{C}_{23}^k \\ 0 & 0 & 0 \end{bmatrix}, \quad \tilde{\mathbf{C}}_{nn}^k = \begin{bmatrix} \tilde{C}_{55}^k & 0 & 0 \\ 0 & \tilde{C}_{44}^k & 0 \\ 0 & 0 & \tilde{C}_{33}^k \end{bmatrix} \quad (2.8)$$

where the Young's modulus (E) and Poisson's ratio (ν) depend on the coordinates (x, y, z) of the considered point.

For the sake of completeness, the explicit forms of the coefficients of the matrices $\tilde{\mathbf{C}}$ are reported in Appendix A.

Models with constant and linear distributions of the in-plane displacement components, u_x and u_z , require modified material coefficients to overcome Poisson locking (see (Carrera et al., 2011a)). The correction process is based on the assumption of null transverse normal stresses, σ_{xx} and σ_{zz} , while the corresponding strain components, ϵ_{xx} and ϵ_{zz} , are accordingly calculated and substituted in the σ_{yy} and σ_{xy} expressions. These coefficients are used in the aforementioned linear cases. A more comprehensive analysis of the effect of Poisson locking and its correction can be found in Carrera et al. (2010b) and Carrera and Petrolo (2011b).

2.2 Carrera unified formulation

The unified formulation of the beam cross-section displacement field is described by an expansion of generic functions

$$\mathbf{u}(x, y, z, t) = F_\tau(x, z) \mathbf{u}_\tau(y, t), \quad \tau = 1, 2, \dots, M \quad (2.9)$$

where $F_\tau(x, z)$ are functions of the cross-section coordinates x and z , $\mathbf{u}_\tau(y, t)$ is the displacement vector, and M stands for the number of terms of the expansion. According to the generalized Einstein notation, the repeated subscript τ indicates summation. The choice of F_τ and M is arbitrary, meaning that different base functions of any-order can be taken into account to model the kinematic field of a beam above the cross-section.

2.2.1 Equivalent-Single Layer Approach: ESL

The ESL approach provides a homogenization of the cross-sectional properties of the structure through summation of the contributions of each constituent part. This process yields an unique set of variables for the whole structure. Following this procedure, a number of different displacement theories has been considered in this work and some examples are outlined below.

Taylor-like expansions: TE 1D class

The first class considered uses Taylor-like expansions, which are obtained by means of 2D polynomials $x^i z^j$ (i and j are positive integers). These models have been used in many applications and their capabilities have been widely discussed in the literature. For sake of completeness, Eqs.2.10 and 2.11 show the TE models of second (TE2) and third (TE3) order, respectively

$$\begin{aligned} u_x &= u_{x1} + x u_{x2} + z u_{x3} + x^2 u_{x4} + xz u_{x5} + z^2 u_{x6} \\ u_y &= u_{y1} + x u_{y2} + z u_{y3} + x^2 u_{y4} + xz u_{y5} + z^2 u_{y6} \\ u_z &= u_{z1} + x u_{z2} + z u_{z3} + x^2 u_{z4} + xz u_{z5} + z^2 u_{z6} \end{aligned} \quad (2.10)$$

$$\begin{aligned}
u_x &= u_{x_1} + x u_{x_2} + z u_{x_3} + x^2 u_{x_4} + xz u_{x_5} + z^2 u_{x_6} + x^3 u_{x_7} + x^2 z u_{x_8} + xz^2 u_{x_9} + z^3 u_{x_{10}} \\
u_y &= u_{y_1} + x u_{y_2} + z u_{y_3} + x^2 u_{y_4} + xz u_{y_5} + z^2 u_{y_6} + x^3 u_{y_7} + x^2 z u_{y_8} + xz^2 u_{y_9} + z^3 u_{y_{10}} \\
u_z &= u_{z_1} + x u_{z_2} + z u_{z_3} + x^2 u_{z_4} + xz u_{z_5} + z^2 u_{z_6} + x^3 u_{z_7} + x^2 z u_{z_8} + xz^2 u_{z_9} + z^3 u_{z_{10}}
\end{aligned} \tag{2.11}$$

Regarding Eq.2.11, the refined expansion has 27 generalized displacement variables: three constant, six linear, nine parabolic and twelve cubic terms. The classical beam theories can be derived as particular cases of the first order Taylor-like expansion (TE1). Indeed, to obtain the first-order shear deformation theory (TBT) of Eq.2.12, the linear terms, u_{x_2} , u_{x_3} , u_{z_2} , u_{z_3} can be neglected, and $\theta(y)$ and $\phi(y)$ are assumed equal to u_{y_2} and u_{y_3} . On the other hand, the Euler-Bernoulli (EBBT) beam model requires an additional condition resulting in the penalization of ϵ_{xy} and ϵ_{zy} . This condition can be imposed using a penalty technique in the constitutive equations.

$$\begin{aligned}
u_x &= u_{0x}(y) \\
u_y &= u_{0y}(y) + \theta(y)x + \phi(y)z \\
u_z &= u_{0z}(y)
\end{aligned} \tag{2.12}$$

Advanced Theories based on Trigonometric and Exponential Expansions

Other ESL theories are obtained adopting trigonometric and exponential functions. In these cases, the displacement fields become

$$\begin{aligned}
u_x &= \sin\left(\frac{\pi x}{a}\right) u_{x_1} + \cos\left(\frac{\pi x}{a}\right) u_{x_2} + \sin\left(\frac{\pi z}{b}\right) u_{x_3} + \cos\left(\frac{\pi z}{b}\right) u_{x_4} + \sin\left(2\frac{\pi x}{a}\right) u_{x_5} + \dots \\
u_y &= \sin\left(\frac{\pi x}{a}\right) u_{y_1} + \sin\left(\frac{\pi x}{a}\right) u_{y_2} + \sin\left(\frac{\pi z}{b}\right) u_{y_3} + \cos\left(\frac{\pi z}{b}\right) u_{y_4} + \sin\left(2\frac{\pi x}{a}\right) u_{y_5} + \dots \\
u_z &= \sin\left(\frac{\pi x}{a}\right) u_{z_1} + \sin\left(\frac{\pi x}{a}\right) u_{z_2} + \sin\left(\frac{\pi z}{b}\right) u_{z_3} + \cos\left(\frac{\pi z}{b}\right) u_{z_4} + \sin\left(2\frac{\pi x}{a}\right) u_{z_5} + \dots
\end{aligned}$$

and

$$\begin{aligned}
u_x &= e^{\left(\frac{x}{a}\right)} u_{x_1} + e^{\left(\frac{z}{b}\right)} u_{x_2} + e^{\left(2\frac{x}{a}\right)} u_{x_3} + e^{\left(2\frac{z}{b}\right)} u_{x_4} + \dots \\
u_y &= e^{\left(\frac{x}{a}\right)} u_{y_1} + e^{\left(\frac{z}{b}\right)} u_{y_2} + e^{\left(2\frac{x}{a}\right)} u_{y_3} + e^{\left(2\frac{z}{b}\right)} u_{y_4} + \dots \\
u_z &= e^{\left(\frac{x}{a}\right)} u_{z_1} + e^{\left(\frac{z}{b}\right)} u_{z_2} + e^{\left(2\frac{x}{a}\right)} u_{z_3} + e^{\left(2\frac{z}{b}\right)} u_{z_4} + \dots
\end{aligned}$$

where a, b are the main cross-section dimensions.

Advanced zig-zag Theories

Murakami (1986) introduced his function in the first order shear deformation theory with the purpose of reproducing the zig-zag shape for the displacements of laminated plates. Due to the intrinsic anisotropy of multilayered structures, the first derivative of the displacement variables in the z – *direction* is discontinuous. The above function is able to describe the aforementioned discontinuity (see Fig.2.3).

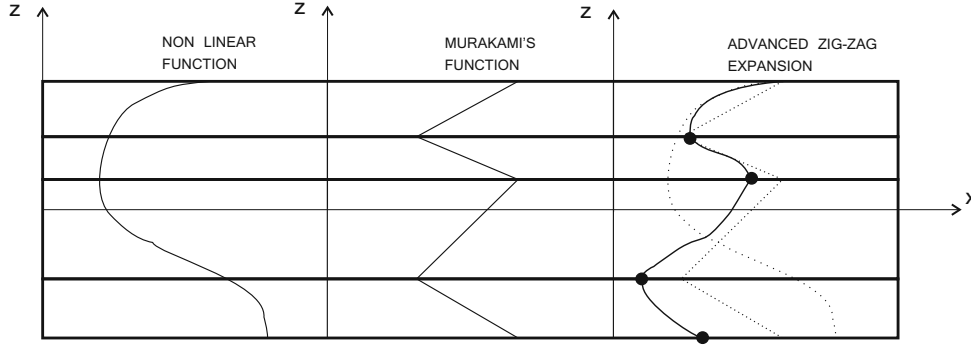


Figure 2.3 Physical and material reference system

Using the zig-zag function within the CUF framework, in the following, all theories containing this term are identified with the exponent (z^z). For example, $TE2^{zz}$:

$$\begin{aligned} u_x &= u_{x_1} + x u_{x_2} + z u_{x_3} + x^2 u_{x_4} + xz u_{x_5} + z^2 u_{x_6} + (-1)^k \zeta_k u_{x_7z} \\ u_y &= u_{y_1} + x u_{y_2} + z u_{y_3} + x^2 u_{y_4} + xz u_{y_5} + z^2 u_{y_6} + (-1)^k \zeta_k u_{y_7z} \\ u_z &= u_{z_1} + x u_{z_2} + z u_{z_3} + x^2 u_{z_4} + xz u_{z_5} + z^2 u_{z_6} + (-1)^k \zeta_k u_{z_7z} \end{aligned}$$

where $\zeta_k = 2z_k/h_k$ is a non-dimensional layer coordinate and h_k the thickness of the k^{th} -layer. The exponent k changes the sign of the zig-zag term in each layer.

Advanced Theories based on Miscellaneous Expansions

To further improve the kinematic model, we can combine the different functions, therefore obtaining miscellaneous expansions. One expansion is given below:

$$\begin{aligned} u_x &= u_{x_1} + x u_{x_2} + z u_{x_3} + x^2 u_{x_4} + xz u_{x_5} + z^2 + e^{(1\frac{x}{a})} u_{x_6} + e^{(1\frac{z}{b})} u_{x_7} + \sin\left(3\frac{\pi x}{a}\right) u_{x_8} \\ u_y &= u_{y_1} + x u_{y_2} + z u_{y_3} + x^2 u_{y_4} + xz u_{y_5} + z^2 + e^{(1\frac{x}{a})} u_{y_6} + e^{(1\frac{z}{b})} u_{y_7} + \sin\left(3\frac{\pi x}{a}\right) u_{y_8} \\ u_z &= u_{z_1} + x u_{z_2} + z u_{z_3} + x^2 u_{z_4} + xz u_{z_5} + z^2 + e^{(1\frac{x}{a})} u_{z_6} + e^{(1\frac{z}{b})} u_{z_7} + \sin\left(3\frac{\pi x}{a}\right) u_{z_8} \end{aligned}$$

Further cases will be directly described in the numerical discussion.

2.2.2 The Layer-Wise Approach: LW

According to the LW approach, a different set of variables may be assumed for each part that constitutes the structure. Therefore, the homogenization process is only conducted in correspondence to the shared interfaces between two cross-sectional regions. Although the Lagrange 1D class can be also used in the ESL framework, its main feature is the capability to provide an accurate component-wise description (therefore layer-wise) of the structure.

Lagrange expansion (LE) 1D class

LE models use Lagrange polynomials to build 1D higher-order theories and the isoparametric

formulation is exploited to deal with arbitrary shaped geometries. For the nine-point element (L9) (see Fig.2.4), the interpolation functions are given by

$$\begin{aligned}
 F_\tau &= \frac{1}{4}(r^2 + r r_\tau)(s^2 + s s_\tau) & \tau = 1, 3, 5, 7 \\
 F_\tau &= \frac{1}{2}s_\tau^2(s^2 - s s_\tau)(1 - r^2) + \frac{1}{2}r_\tau^2(r^2 - r r_\tau)(1 - s^2) & \tau = 2, 4, 6, 8 \\
 F_\tau &= (1 - r^2)(1 - s^2) & \tau = 9
 \end{aligned} \tag{2.13}$$

where r and s range from -1 to $+1$. The displacement field given by an L9 element is

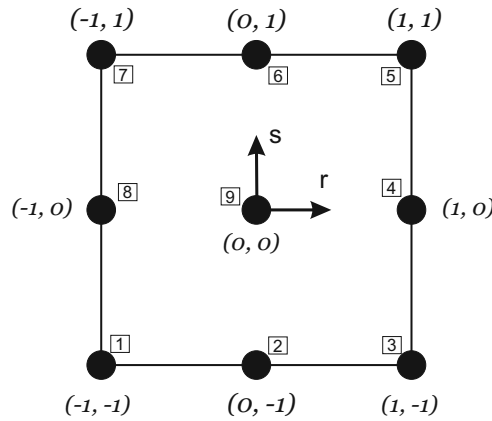


Figure 2.4 Cross-section L9 element

$$\begin{aligned}
 u_x &= F_1 u_{x_1} + F_2 u_{x_2} + F_3 u_{x_3} + F_4 u_{x_4} + F_5 u_{x_5} + F_6 u_{x_6} + F_7 u_{x_7} + F_8 u_{x_8} + F_9 u_{x_9} \\
 u_y &= F_1 u_{y_1} + F_2 u_{y_2} + F_3 u_{y_3} + F_4 u_{y_4} + F_5 u_{y_5} + F_6 u_{y_6} + F_7 u_{y_7} + F_8 u_{y_8} + F_9 u_{y_9} \\
 u_z &= F_1 u_{z_1} + F_2 u_{z_2} + F_3 u_{z_3} + F_4 u_{z_4} + F_5 u_{z_5} + F_6 u_{z_6} + F_7 u_{z_7} + F_8 u_{z_8} + F_9 u_{z_9}
 \end{aligned} \tag{2.14}$$

where u_{x_1}, \dots, u_{z_9} are the displacement variables of the problem and they represent the translational displacement components of each of the nine points of the L9 element. This means that LE models provide elements that only have displacement variables. According to Carrera and Petrolo (2011b), the beam cross-section can be discretized using several L-elements for extra refinements, as shown in Fig.2.5 where two L9 elements are assembled.

For further details on Lagrange 1D models, we refer to (Carrera and Petrolo, 2011b,c) where L3, L4, L6 and L16 sets are also described.

2.3 The Finite Element formulation

The governing equations of a system can be derived by means of different variational principles of Mechanics such as the Principle of Virtual Displacements (PVD), D'Alembert's Principle and Hamilton's Principle. Regardless of the chosen procedure, with the use of CUF, all contributions in the governing equations (mass, stiffness, damping and loading arrays) are written in terms of 'fundamental nuclei', whose forms are independent of the order of models. In order to overcome the limitations of the analytical approaches, the weak form of the governing equations is solved using the Finite Element method (FE). The generalized displacement vector (see Eq.2.9) is given by :

$$\mathbf{u}_\tau(y, t) = N_i(y) \mathbf{q}_{\tau i}(t) \tag{2.15}$$

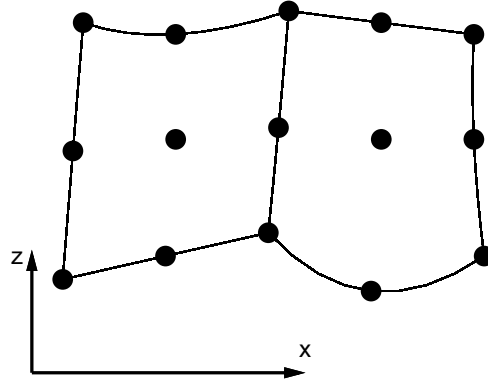


Figure 2.5 Two assembled L9 elements in actual geometry.

where N_i are the shape functions and $\mathbf{q}_{\tau i}(t)$ is the nodal displacement vector:

$$\mathbf{q}_{\tau i}(t) = \{ q_{u_{x\tau i}} \quad q_{u_{y\tau i}} \quad q_{u_{z\tau i}} \}^T \quad i = 1, \dots, N_{node} \quad (2.16)$$

with ' N_{node} ' as the number of nodes of the element. Hereafter, the vector dependencies on time (t) and spatial coordinates (x,y,z) will be omitted. Here three different finite elements are considered to provide a linear (B2), a quadratic (B3) and a cubic (B4) interpolation of the displacement variable along the beam axis. The lagrangian shape functions of the B2, B3 and B4 elements are thus defined as,

$$N_1 = \frac{1}{2}(1-r), \quad N_2 = \frac{1}{2}(1+r), \quad \begin{cases} r_1 = -1 \\ r_2 = +1 \end{cases}$$

$$N_1 = \frac{1}{2}r(r-1), \quad N_2 = \frac{1}{2}r(r+1), \quad N_3 = -(1+r)(1-r), \quad \begin{cases} r_1 = -1 \\ r_2 = +1 \\ r_3 = 0 \end{cases} \quad (2.17)$$

$$N_1 = -\frac{9}{16}(r + \frac{1}{3})(r - \frac{1}{3})(r - 1), \quad N_2 = \frac{9}{16}(r + \frac{1}{3})(r - \frac{1}{3})(r + 1), \quad \begin{cases} r_1 = -1 \\ r_2 = +1 \\ r_3 = -\frac{1}{3} \\ r_4 = +\frac{1}{3} \end{cases}$$

$$N_3 = +\frac{27}{16}(r + 1)(r - \frac{1}{3})(r - 1), \quad N_4 = -\frac{27}{16}(r + 1)(r + \frac{1}{3})(r - 1), \quad \begin{cases} r_1 = -1 \\ r_2 = +1 \\ r_3 = -\frac{1}{3} \\ r_4 = +\frac{1}{3} \end{cases}$$

where the natural coordinate, r , varies from -1 to $+1$ and r_i indicates the position of the node within the natural beam boundaries.

Chapter 3

Carrera Unified Formulation in Rotordynamics

In this chapter, the equations of motion (EoM) for rotating structures in CUF form are derived by means of Hamilton's Principle. Then, the fundamental nucleus expression of each term in the equations are provided.

3.1 Hamilton's Principle and Lagrange's Equations

The general form of Hamilton's Principle states that the variation of the kinetic and potential energy and the variation of the work exerted by non-conservative forces must equal zero during any time interval. It may be expressed as

$$\int_{t_0}^{t_1} \delta (T - U) dt + \int_{t_0}^{t_1} \delta W_{nc} dt = 0 \quad (3.1)$$

where δ refers to kinematically admissible perturbations during the indicated time interval and

- T: Total Kinetic Energy of the system
- U: Total Potential Energy of the system, including both strain energy and potential of any conservative external forces
- W_{nc} : Work done by non-conservative forces acting on the system, including any arbitrary external loads

The application of this variational concept leads directly to the EoM for any given system. If we express the energies in terms of generalised coordinates

$$T = T(q_1, \dots, q_n, \dot{q}_1, \dots, \dot{q}_n, t) \quad U = U(q_1, \dots, q_n, t) \quad \delta W_{nc} = Q_1 \delta q_1 + \dots + Q_n \delta q_n \quad (3.2)$$

where ' Q_k ' are the generalised forces, the energy variations can be presented as

$$\delta T = \sum_{k=1}^n \left(\frac{\partial T}{\partial q_k} \delta q_k + \frac{\partial T}{\partial \dot{q}_k} \delta \dot{q}_k \right) \quad \delta U = \sum_{k=1}^n \left(\frac{\partial U}{\partial q_k} \delta q_k \right) \quad \delta W_{nc} = \sum_{k=1}^n (Q_k \delta q_k) \quad (3.3)$$

Substituting Eqs.3.3 into Eq.3.1, we obtain

$$\int_{t_1}^{t_2} \left[\sum_{k=1}^n \left(\frac{\partial T}{\partial q_k} \delta q_k + \frac{\partial T}{\partial \dot{q}_k} \delta \dot{q}_k \right) - \sum_{k=1}^n \left(\frac{\partial U}{\partial q_k} \delta q_k \right) + \sum_{k=1}^n (Q_k \delta q_k) \right] \quad (3.4)$$

Integration by parts on the time-dependent terms yields

$$\int_{t_1}^{t_2} \left[\sum_{k=1}^n \left(\frac{\partial T}{\partial q_k} - \frac{d}{dt} \left(\frac{\partial T}{\partial \dot{q}_k} \right) - \frac{\partial U}{\partial q_k} + Q_k \right) \delta q_k \right] dt = 0 \quad (3.5)$$

Finally, since the variation must be arbitrary and independent, we obtain Lagrange's equations that directly lead to EoM.

$$\frac{d}{dt} \left(\frac{\partial T}{\partial \dot{q}_k} \right) - \frac{\partial T}{\partial q_k} + \frac{\partial U}{\partial q_k} = Q_k \quad (3.6)$$

The solutions of Eq.3.6 are the stationary points of Eq.3.1.

3.1.1 The structural stiffness matrix and the loading vector in CUF form

In order to derive the expressions of stiffness matrix and loading vector, we consider a structure subjected to a generic concentrate load \mathbf{P} applied at (x^p, y^p, z^p) , while its kinetic energy is assumed null.

$$\mathbf{P} = \{P_x \quad P_y \quad P_z\}^T \quad (3.7)$$

The potential energy can be expressed as

$$U = \frac{1}{2} \int_V (\mathbf{u}^T \mathbf{D}^T \mathbf{C} \mathbf{D} \mathbf{u}) dV \quad (3.8)$$

where \mathbf{u} is the displacement vector of Eq.2.1, \mathbf{D} is the matrix of linear differential operators and \mathbf{C} is the matrix of material coefficients. Substituting Eqs.3.7 and 3.8 in Eq.3.1 we obtain

$$\int_{t_0}^{t_1} \left(\int_V \delta \mathbf{u}^T (\mathbf{D}^T \mathbf{C} \mathbf{D}) \mathbf{u} dV - \delta \mathbf{u}^T \mathbf{P} \right) dt = 0 \quad (3.9)$$

Then, introducing the CUF (Eq2.9) and FE (Eq.2.15) approximations, Eq.3.9 becomes

$$\int_{t_0}^{t_1} \left(\delta \mathbf{q}_{\tau i}^T \mathbf{K}^{ij\tau s} \mathbf{q}_{s j} - \delta \mathbf{q}_{\tau i}^T \tilde{\mathbf{P}}^{i\tau} \right) dt = 0 \quad (3.10)$$

where $\mathbf{K}^{ij\tau s}$ and $\tilde{\mathbf{P}}^{i\tau}$ are the structural stiffness matrix and the loading vector in terms of the fundamental nuclei, whose expressions are reported below

$$\begin{aligned}
 \mathbf{K}^{ij\tau s} = & I_l^{ij} \triangleleft \mathbf{D}_{np}^T(F_\tau \mathbf{I}) \left[\tilde{\mathbf{C}}_{np}^k \mathbf{D}_p(F_s \mathbf{I}) + \tilde{\mathbf{C}}_{nn}^k \mathbf{D}_{np}(F_s \mathbf{I}) \right] + \\
 & + \mathbf{D}_p^T(F_\tau \mathbf{I}) \left[\tilde{\mathbf{C}}_{pp}^k \mathbf{D}_p(F_s \mathbf{I}) + \tilde{\mathbf{C}}_{pn}^k \mathbf{D}_{np}(F_s \mathbf{I}) \right] \triangleright + \\
 & + I_l^{ij,y} \triangleleft \left[\mathbf{D}_{np}^T(F_\tau \mathbf{I}) + \mathbf{D}_p^T(F_\tau \mathbf{I}) \tilde{\mathbf{C}}_{pn}^k \right] F_s \triangleright + \mathbf{I}_{Ay} \\
 & + I_l^{i,yj} \mathbf{I}_{Ay}^T \triangleleft F_\tau \left[\tilde{\mathbf{C}}_{np}^k \mathbf{D}_p(F_s \mathbf{I}) + \tilde{\mathbf{C}}_{nn}^k \mathbf{D}_{np}(F_s \mathbf{I}) \right] \triangleright + \\
 & + I_l^{i,yj,y} \mathbf{I}_{Ay}^T \mathbf{I}_{Ay} \triangleleft F_\tau \tilde{\mathbf{C}}_{nn}^k F_s \triangleright
 \end{aligned} \tag{3.11}$$

$$\tilde{\mathbf{P}}^{i\tau} = N_i(y^p) F_\tau(x^p, z^p) \mathbf{P}$$

where

$$\mathbf{I}_{Ay} = \begin{bmatrix} 0 & 0 & 1 \\ 1 & 0 & 0 \\ 0 & 1 & 0 \end{bmatrix} \quad \triangleleft \dots \triangleright = \int_A \dots dA \tag{3.12}$$

$$\left(I_l^{ij}, I_l^{ij,y}, I_l^{i,yj}, I_l^{i,yj,y} \right) = \int_l \left(N_i N_j, N_i N_{j,y}, N_{i,y} N_j, N_{i,y} N_{j,y} \right) dy \tag{3.13}$$

For the sake of completeness, in Appendix B, the nine components of the fundamental nucleus of the matrix $\mathbf{K}^{ij\tau s}$ are written in an explicit form. We refer to (Carrera et al., 2014b) for a detailed discussion on the computation of loading vector. It must be noted that

1. $\mathbf{K}^{ij\tau s}$ does not depend on the expansion order.
2. $\mathbf{K}^{ij\tau s}$ does not depend on the choice of the F_τ expansion polynomials.

These are the key-points of CUF which permits, with only nine statements, to implement any-order of multiple class theories.

After a classical assembly procedure, which has been illustrated in Sec.2.3, and applying Eq.3.6 we obtain the following algebraic problem

$$\tilde{\mathbf{K}} \mathbf{q} = \tilde{\mathbf{P}} \tag{3.14}$$

where $\tilde{\mathbf{k}}$, $\tilde{\mathbf{P}}$ and \mathbf{q} indicate the global stiffness matrix, the loading and the unknown vectors, respectively.

3.2 Dynamics of spinning structures

When a structure is rotating, inertial forces and moments are observed. We consider a beam that is free to rotate about its longitudinal axis with a constant spin-speed Ω and supported by N_b bearings. In this case, Hamilton's Principle can be expressed as

$$\delta \int_{t_0}^{t_1} (T - (U + U_{\sigma_0}) + W_b) dt = 0 \tag{3.15}$$

where the terms ' W_b ' and ' U_{σ_0} ' are the contributions due to the bearings and centrifugal effect, respectively. Following the procedure described in Sec.3.1.1, we derive the variations of the different energetic contributions.

3.2.1 The Kinetic Energy

Figure 3.1 shows the rotating reference frame and the cross-section of the beam.

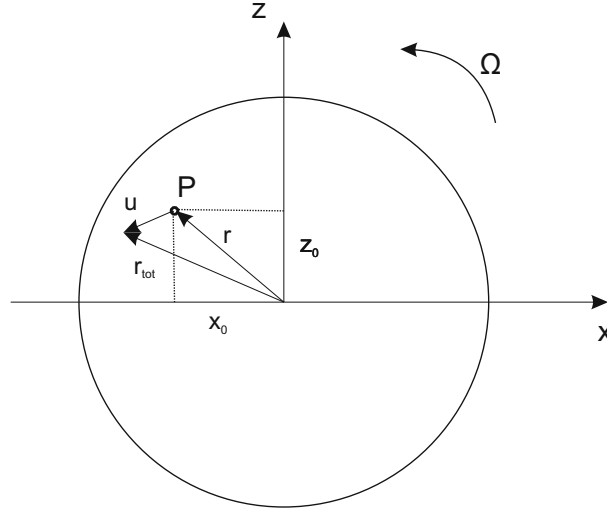


Figure 3.1 Sketch of the rotating reference frame.

The absolute velocity of the point P is the sum of relative and transfer velocities.

$$\mathbf{v}_{abs} = \mathbf{v}_{rel} + \mathbf{v}_{tr} = \dot{\mathbf{u}} + \boldsymbol{\Omega} \times \mathbf{r}_{tot} \quad (3.16)$$

$$\boldsymbol{\Omega} = \begin{bmatrix} 0 & 0 & \Omega \\ 0 & 0 & 0 \\ -\Omega & 0 & 0 \end{bmatrix}$$

where $\mathbf{r}_{tot} = \mathbf{r} + \mathbf{u}$ is the distance of P from the neutral axis. Hence, the kinetic energy of the whole structure is

$$T = \frac{1}{2} \int_V \rho (\dot{\mathbf{u}}^T \dot{\mathbf{u}} + 2\mathbf{u}^T \boldsymbol{\Omega}^T \dot{\mathbf{u}} + \mathbf{u}^T \boldsymbol{\Omega}^T \boldsymbol{\Omega} \mathbf{u} + 2\dot{\mathbf{u}}^T \boldsymbol{\Omega} \mathbf{r} + 2\mathbf{u}^T \boldsymbol{\Omega}^T \boldsymbol{\Omega} \mathbf{r} + \mathbf{r}^T \boldsymbol{\Omega}^T \boldsymbol{\Omega} \mathbf{r}) dV \quad (3.17)$$

3.2.2 The Centrifugal Potential Energy

The geometrical potential energy, U_{σ_0} , is fundamental when a highly deformable structure is rotating.

$$U_{\sigma_0} = \int_V (\boldsymbol{\sigma}_0^T \boldsymbol{\epsilon}_{nl}) dV \quad (3.18)$$

This term depends on non-linear term components of the strain field $\boldsymbol{\epsilon}_{nl}$ and the pre-stress $\boldsymbol{\sigma}_0$. The $\boldsymbol{\sigma}_0$ distribution is function of the structure characteristics and it is therefore, changed according to the studied problem.

The pre-stress field for axial-symmetric structures is typically provided in terms of circumferential ($\sigma_{\delta\delta}$), radial (σ_{rr}) and axial (σ_{yy}) contributions that, written in a cartesian coordinate system, are

$$\begin{aligned}
 \sigma_{0_{xx}} &= \sigma_{\delta\delta} \sin(\delta)^2 + \sigma_{rr} \cos(\delta)^2 \\
 \sigma_{0_{yy}} &= \sigma_{yy} \\
 \sigma_{0_{zz}} &= \sigma_{\delta\delta} \cos(\delta)^2 + \sigma_{rr} \sin(\delta)^2 \\
 \sigma_{0_{xz}} (= \sigma_{0_{zx}}) &= \sigma_{rr} \sin(\delta) \cos(\delta) - \sigma_{\delta\delta} \sin(\delta) \cos(\delta)
 \end{aligned}$$

In the case of a thin-walled cylinder, the only initial stress acts in the circumferential direction and it is assumed equal to

$$\sigma_0 = \rho\Omega^2 R_m, \quad (3.19)$$

where ' ρ ' is the density and ' R_m ' is the mean radius. Conversely, for a deformable blade, the centrifugal pre-stress acts along the radial direction and its expression is

$$\sigma_0 = \Omega^2 \rho \left[r_h R + \frac{1}{2} R^2 - r_h r - \frac{1}{2} r^2 \right] \quad (3.20)$$

where ' R ' is the maximum distance from the hub, whose radius is ' r_h '. Regarding a thin hollow disk, the radial ' σ_r^Ω ' and circumferential ' σ_c^Ω ' contributions are defined by Manson's equations

$$\begin{aligned}
 \sigma_r^\Omega &= \sigma_0 \frac{(3+\nu)}{8} \left[1 + \frac{D_i^2}{D_e^2} - \frac{D_i^2}{D^2} - \frac{D^2}{D_e^2} \right] \\
 \sigma_c^\Omega &= \sigma_0 \frac{(3+\nu)}{8} \left[1 + \frac{D_i^2}{D_e^2} + \frac{D_i^2}{D^2} - \frac{(1+3\nu)}{(3+\nu)} \frac{D^2}{D_e^2} \right]
 \end{aligned} \quad (3.21)$$

in which ' D_i ' and ' D_e ' are the inner and external diameters of the disk, respectively. The term σ_0 coincides with Eq.3.19.

Regardless of the considered structure, the geometrical potential energy is defined as

$$U_{\sigma_0} = \int_V \sigma_{0_{xx}} \epsilon_{xx}^{nl} + \sigma_{0_{zz}} \epsilon_{zz}^{nl} + \sigma_{0_{xz}} \epsilon_{xz}^{nl} + \sigma_{0_{zx}} \epsilon_{zx}^{nl} dV \quad (3.22)$$

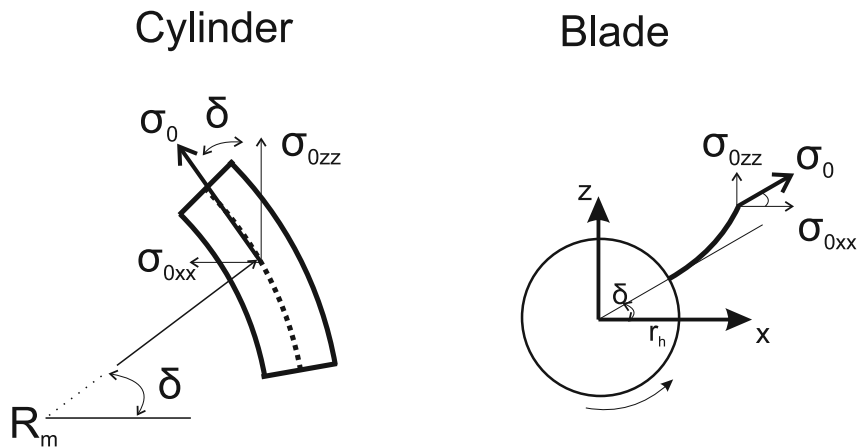


Figure 3.2 The centrifugal stiffness.

3.2.3 Stiffness and Damping due to bearings

The N_b bearings are modeled as springs and viscous dampers, therefore, the term W_b is expressed as

$$W_b = \sum_{p=1}^{N_b} \mathbf{u}^T \mathbf{K}_b^p \mathbf{u} + \dot{\mathbf{u}}^T \mathbf{C}_b^p \mathbf{u} \quad (3.23)$$

Considering the generic p -th bearing whose coordinates are (x_b, y_b, z_b) , the stiffness and damping coefficients are

$$\mathbf{K}_b^p = \begin{bmatrix} k_{xx}^p & k_{xy}^p & k_{xz}^p \\ k_{yx}^p & k_{yy}^p & k_{yz}^p \\ k_{zx}^p & k_{zy}^p & k_{zz}^p \end{bmatrix}, \quad \mathbf{C}_b^p = \begin{bmatrix} c_{xx}^p & c_{xy}^p & c_{xz}^p \\ c_{yx}^p & c_{yy}^p & c_{yz}^p \\ c_{zx}^p & c_{zy}^p & c_{zz}^p \end{bmatrix} \quad (3.24)$$

3.2.4 The Equations of Motion

Similarly to the static case of Sec.3.1.1, introducing the CUF (Eq.2.9) and FE (Eq.2.15) approximations and substituting Eqs.3.8, 3.17, 3.22 and 3.23 in Eq.3.15, we obtain

$$\int_{t_0}^{t_1} \left(\delta \mathbf{q}_{\tau i}^T \mathbf{M}^{ij\tau s} \ddot{\mathbf{q}}_{sj} + \delta \mathbf{q}_{\tau i}^T \mathbf{G}_{TOT}^{ij\tau s} \dot{\mathbf{q}}_{sj} + \delta \mathbf{q}_{\tau i}^T \mathbf{K}_{TOT}^{ij\tau s} \mathbf{q}_{sj} + \delta \mathbf{q}_{\tau i}^T \mathbf{F}_{\Omega}^{i\tau} \mathbf{r} \right) dt = 0 \quad (3.25)$$

where

$$\begin{aligned} \mathbf{G}_{TOT}^{ij\tau s} &= \mathbf{G}_{\Omega}^{ij\tau s} + \mathbf{G}_b^{ij\tau s} \\ \mathbf{K}_{TOT}^{ij\tau s} &= \mathbf{K}^{ij\tau s} + \mathbf{K}_b^{ij\tau s} + \mathbf{K}_{\Omega}^{ij\tau s} + \mathbf{K}_{\sigma_0}^{ij\tau s} \end{aligned} \quad (3.26)$$

In addition to the mass matrix $\mathbf{M}^{ij\tau s}$ and the stiffness matrix $\mathbf{K}^{ij\tau s}$, the rotation introduces the following terms

- the Coriolis matrix $\mathbf{G}^{ij\tau s}$
- the matrix of bearing damping $\mathbf{G}_b^{ij\tau s}$
- the matrix of bearing stiffness $\mathbf{K}_b^{ij\tau s}$
- the matrix of spin softening $\mathbf{K}_{\Omega}^{ij\tau s}$
- the matrix of centrifugal stiffening $\mathbf{K}_{\sigma_0}^{ij\tau s}$
- the load vector $\mathbf{F}_{\Omega}^{i\tau}$

As previously done for the stiffness matrix $\mathbf{K}^{ij\tau s}$, the *fundamental nuclei* related to the above matrices are reported below

$$\begin{aligned}
 M^{ij\tau s} &= I_l^{ij} \langle (F_\tau \rho^k \mathbf{I} F_s) \rangle \\
 \mathbf{G}_\Omega^{ij\tau s} &= I_l^{ij} \langle (F_\tau \rho^k \mathbf{I} F_s) \rangle \triangleright 2\Omega \\
 \mathbf{G}_b^{ij\tau s} &= \sum_{p=1}^{N_b} N_i(y_b^p) F_\tau(x_b^p, z_b^p) \mathbf{C}_b^p F_s(x_b^p, z_b^p) N_j(y_b^p) \\
 \mathbf{K}_b^{ij\tau s} &= \sum_{p=1}^{N_b} N_i(y_b^p) F_\tau(x_b^p, z_b^p) \mathbf{K}_b^p F_s(x_b^p, z_b^p) N_j(y_b^p) \\
 \mathbf{K}_\Omega^{ij\tau s} &= -I_l^{ij} \langle (F_\tau \rho^k \mathbf{I} F_s) \rangle \triangleright \Omega^T \Omega \\
 \mathbf{K}_{\sigma_0}^{ij\tau s} &= I_l^{ij} \langle (F_{\tau,x} \sigma_{0xx} \mathbf{I} F_{s,x}) + (F_{\tau,z} \sigma_{0zz} \mathbf{I} F_{s,z}) + \\
 &\quad + (F_{\tau,x} \sigma_{0xz} \mathbf{I} F_{s,z}) + (F_{\tau,z} \sigma_{0zx} \mathbf{I} F_{s,x}) \rangle \\
 \mathbf{F}_\Omega^{i\tau} &= I_l^i \Omega^T \Omega \langle F_\tau \mathbf{I} \rho r \rangle
 \end{aligned} \tag{3.27}$$

where

$$\mathbf{I} = \begin{bmatrix} 1 & 0 & 0 \\ 0 & 1 & 0 \\ 0 & 0 & 1 \end{bmatrix} \tag{3.28}$$

$$\langle \dots \rangle = \int_A \dots dA \tag{3.29}$$

$$\left(I_l^i, I_l^{ij}, I_l^{ij,y}, I_l^{i,yj}, I_l^{i,yj,y} \right) = \int_l \left(N_i, N_i N_j, N_i N_{j,y}, N_{i,y} N_j, N_{i,y} N_{j,y} \right) dy \tag{3.30}$$

and $\mathbf{r} = \{x_P, 0, z_P\}^T$ is the distance of a generic point P on the cross-section from the neutral axis. In matrix form, the new *fundamental nuclei* are

$$\begin{aligned}
 \mathbf{G}_\Omega^{ij\tau s} &= \Omega \begin{bmatrix} 0 & 0 & -2 I_l^{i,j} \langle F_\tau \rho F_s \rangle \\ 0 & 0 & 0 \\ 2 I_l^{i,j} \langle F_\tau \rho F_s \rangle & 0 & 0 \end{bmatrix} \\
 \mathbf{K}_\Omega^{ij\tau s} &= \Omega^2 \begin{bmatrix} -I_l^{i,j} \langle F_\tau \rho F_s \rangle & 0 & 0 \\ 0 & 0 & 0 \\ 0 & 0 & -I_l^{i,j} \langle F_\tau \rho F_s \rangle \end{bmatrix} \\
 \mathbf{K}_{\sigma_0}^{ij\tau s} &= \Omega^2 \begin{bmatrix} I_l^{ij} K_{\sigma_0} & 0 & 0 \\ 0 & I_l^{ij} (K_{\sigma_0}) & 0 \\ 0 & 0 & I_l^{ij} K_{\sigma_0} \end{bmatrix} \\
 \mathbf{F}_\Omega^{i\tau} &= \Omega^2 \begin{bmatrix} I_l^i \langle F_\tau \rho x_P \rangle \\ 0 \\ I_l^i \langle F_\tau \rho z_P \rangle \end{bmatrix}
 \end{aligned} \tag{3.31}$$

To obtain the natural frequencies and the normal modes of the rotor, we solve the homogeneous equation:

$$\mathbf{M} \ddot{\mathbf{q}} + \mathbf{G}_{TOT} \dot{\mathbf{q}} + \mathbf{K}_{TOT} \mathbf{q} = 0 \quad (3.32)$$

Assuming a periodic function as solution

$$\mathbf{q} = \bar{\mathbf{q}} e^{i\omega t} \quad (3.33)$$

Substituting Eq.3.33 and its derivative in Eq.3.32, we obtain

$$\bar{\mathbf{q}} e^{i\omega t} [\mathbf{K}_{TOT} + \mathbf{G}_{TOT} i\omega - \mathbf{M} \omega^2] = 0 \quad (3.34)$$

The quadratic eigenvalues problem (QEP) of generic order R in Eq.3.34 is transformed in a classical linear system of order $2 \times R$:

$$\begin{cases} \mathbf{M} \ddot{\mathbf{q}} + \mathbf{G}_{TOT} \dot{\mathbf{q}} + \mathbf{K}_{TOT} \mathbf{q} = 0 \\ -\dot{\mathbf{q}} + \dot{\mathbf{q}} = 0 \end{cases} \quad (3.35)$$

Now, introducing:

$$\mathbf{a} = \begin{Bmatrix} \mathbf{q} \\ \dot{\mathbf{q}} \end{Bmatrix} \quad \dot{\mathbf{a}} = \begin{Bmatrix} \dot{\mathbf{q}} \\ \ddot{\mathbf{q}} \end{Bmatrix} \quad (3.36)$$

the equations of motion assume the form:

$$\frac{\mathbf{R}}{\mathbf{T}} - \frac{1}{i\omega} \mathbf{I} = 0 \quad (3.37)$$

where:

$$\mathbf{T}^{-1} \mathbf{R} = \begin{bmatrix} (\mathbf{K}_{TOT})^{-1}(\mathbf{G}_{TOT}) & (\mathbf{K}_{TOT})^{-1}(\mathbf{M}) \\ -\mathbf{I} & \mathbf{0} \end{bmatrix} \quad (3.38)$$

The problem in Eq.3.38 is in the classical form and can be solved with the standard eigensolvers.

3.3 Dynamics of centrifugally stiffened structures

We consider, in this section, a structure that is rotating about the z-axis as shown in Fig.3.3. In this case, the work done by supports is not taken into account, therefore, Hamilton's principle becomes

$$\delta \int_{t_0}^{t_1} (T - (U + U_{\sigma_0})) dt = 0 \quad (3.39)$$

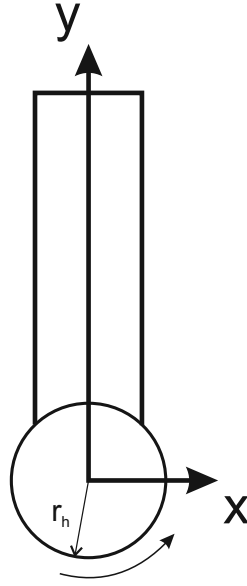


Figure 3.3 Sketch of a centrifugally stiffened structure.

3.3.1 The Kinetic Energy

The constant rotational speed matrix is

$$\mathbf{\Omega} = \begin{bmatrix} 0 & -\Omega & 0 \\ \Omega & 0 & 0 \\ 0 & 0 & 0 \end{bmatrix}$$

Hence, the kinetic energy of the whole structure becomes

$$T = \frac{1}{2} \int_V \rho (\dot{\mathbf{u}}^T \dot{\mathbf{u}} + 2\mathbf{u}^T \mathbf{\Omega}^T \dot{\mathbf{u}} + \mathbf{u}^T \mathbf{\Omega}^T \mathbf{\Omega} \mathbf{u} + 2\dot{\mathbf{u}}^T \mathbf{\Omega} \mathbf{r} + 2\mathbf{u}^T \mathbf{\Omega}^T \mathbf{\Omega} \mathbf{r}) dV \quad (3.40)$$

3.3.2 The Centrifugal Potential Energy

Although the ' σ_0 ' distribution is the same of Eq.3.20, the expression of the centrifugal potential energy involves non-linear strain terms that are different from the previous case

$$U_{\sigma_0} = \frac{1}{2} \int_V \sigma_0 (u_{x,y}^2 + u_{y,y}^2 + u_{z,y}^2) dV \quad (3.41)$$

It should be noted that, despite the non-linear contribution ' $u_{y,y}$ ' is usually omitted in the literature, its role may be important due to the coupling between axial and chordwise motions.

3.3.3 The Equations of Motion

Once again introducing the CUF (Eq.2.9) and FE (Eq.2.15) approximations and substituting Eqs.3.8, 3.40 and 3.41 Eq.3.39, we obtain

$$\int_{t_0}^{t_1} \left(\delta \mathbf{q}_{\tau i}^T \mathbf{M}^{ij\tau s} \ddot{\mathbf{q}}_{s j} + \delta \mathbf{q}_{\tau i}^T \mathbf{G}_{TOT}^{ij\tau s} \dot{\mathbf{q}}_{s j} + \delta \mathbf{q}_{\tau i}^T \mathbf{K}_{TOT}^{ij\tau s} \mathbf{q}_{s j} + \delta \mathbf{q}_{\tau i}^T \mathbf{F}_{\Omega}^{i\tau} \mathbf{r} \right) dt = 0 \quad (3.42)$$

where

$$\mathbf{G}_{TOT}^{ij\tau s} = \mathbf{G}_{\Omega}^{ij\tau s} \quad (3.43)$$

$$\mathbf{K}_{TOT}^{ij\tau s} = \mathbf{K}_{\Omega}^{ij\tau s} + \mathbf{K}_{\sigma_0}^{ij\tau s}$$

The *fundamental nuclei* $\mathbf{G}_{\Omega}^{ij\tau s}$ and $\mathbf{K}_{\Omega}^{ij\tau s}$ have been already defined in Sec.3.2.4, while $\mathbf{K}_{\sigma_0}^{ij\tau s}$ is reported below

$$\mathbf{K}_{\sigma_0}^{ij\tau s} = I_{l\sigma_0}^{i,yj,y} \langle (F_{\tau}\rho\mathbf{I}F_s) \rangle \Omega^T \Omega \quad (3.44)$$

$$\mathbf{F}_{\Omega}^{i\tau} = I_{ly}^i \Omega^T \Omega \langle F_{\tau}\mathbf{I}\rho \rangle$$

where

$$I_{ly}^i, I_{l\sigma_0}^{i,yj,y} = \int_l y N_i, \sigma_0 N_{i,y} N_{j,y} dy \quad (3.45)$$

In this case, the *fundamental nuclei* in matrix form yield

$$\mathbf{G}_{\Omega}^{ij\tau s} = \Omega \begin{bmatrix} 0 & -2I_l^{i,j} \langle F_{\tau}\rho F_s \rangle & 0 \\ 2I_l^{i,j} \langle F_{\tau}\rho F_s \rangle & 0 & 0 \\ 0 & 0 & 0 \end{bmatrix}$$

$$\mathbf{K}_{\Omega}^{ij\tau s} = \Omega^2 \begin{bmatrix} -I_l^{i,j} \langle F_{\tau}\rho F_s \rangle & 0 & 0 \\ 0 & -I_l^{i,j} \langle F_{\tau}\rho F_s \rangle & 0 \\ 0 & 0 & 0 \end{bmatrix}$$

$$\mathbf{K}_{\sigma_0}^{ij\tau s} = \Omega^2 \begin{bmatrix} I_{l\sigma_0}^{i,yj,y} \langle (F_{\tau}\rho\mathbf{I}F_s) \rangle & 0 & 0 \\ 0 & I_{l\sigma_0}^{i,yj,y} \langle (F_{\tau}\rho\mathbf{I}F_s) \rangle & 0 \\ 0 & 0 & I_{l\sigma_0}^{i,yj,y} \langle (F_{\tau}\rho\mathbf{I}F_s) \rangle \end{bmatrix} \quad (3.46)$$

$$\mathbf{F}_{\Omega}^{i\tau} = \Omega^2 \begin{bmatrix} 0 \\ I_{ly}^i \langle F_{\tau}\rho \rangle \\ 0 \end{bmatrix}$$

Following the procedure explained in Sec.3.2.4, we obtain the natural frequencies and normal modes solving Eq.3.38.

The proposed formulation allows to write EoM in a fully three-dimensional form for both spinning and centrifugally stiffened structures. Performance of the 1D-CUF elements in rotordynamics has been evaluated in the result section.

Chapter 4

Aeroelastic models

In this chapter, the expressions of the external work exerted by aerodynamic loads are derived in CUF form. The aerodynamic loads are defined according to steady and unsteady theories for subsonic and supersonic flow regimes.

4.1 2-D steady and unsteady aerodynamic theories for fixed-wing

Theodorsen was the first to propose a complete solution for a thin airfoil that undergoes harmonic lateral oscillations in an incompressible fluid. Adopting the assumptions of the small-disturbance theory, Theodorsen considered a flat plate with a control surface which could move in vertical translation $h(t)$ and rotate about the axis at $x = ba$ through by angle $\alpha(t)$. The final expression of the lift for a unit of span, due to both translation and rotation as derived in (Bisplinghoff et al., 1996), is

$$L = \pi\rho_a b^2 [\ddot{h} + U\dot{\alpha} - ba\ddot{\alpha}] + 2\pi\rho_a U b C(k) \left[\dot{h} + U\alpha + b \left(\frac{1}{2} - a \right) \dot{\alpha} \right] \quad (4.1)$$

where ' U ' is the free-stream velocity, ' b ' the semichord, ' ρ_a ' the air density and ' $C(k)$ ' the deficiency lift function, which depends on the *reduced frequency* $k = \frac{\omega U}{b}$. ' a ' defines the position of the rotation axis with respect to the center of the section and it is dependent on the support condition, the lamination scheme and the applied load. Due to the difficulty in defining its correct value for swept and asymmetric laminated structures, the elastic offset ' a ' is assumed to be null. Theodorsen identified the term ' $C(k)$ ' as a Hankel function of the second kind, which is, in turn, comprised of Bessel functions of the first and second kinds (Rodden, 2012),(Bisplinghoff et al., 1996)

$$C(k) = F(k) + iG(k) = \frac{H_1^{(2)}(k)}{H_1^{(2)}(k) + iH_0^{(2)}(k)} \quad (4.2)$$

A simplified expression of Theodorsen's function was proposed by R.T. Jones in 1940, who presented an exponential approximation of Wagner's indicial solution (1925)

$$C(k) \cong 1 - \frac{0.165}{1 - (0.0455/k)i} - \frac{0.335}{1 - (0.3/k)i} \quad (4.3)$$

The first contribution in Eq.4.1, contains the virtual mass (or noncirculatory) terms that acts as a form of inertia of the fluid surrounding the airfoil and, since the single and doubly-

differentiated terms relative to the mass properties of the structure are small, they are usually neglected. The remaining terms determine the value of the lift and represent the circulatory part. The steady-state simplification can be easily obtained by replacing the function $C(k)$ with the unitary value and omitting the term containing $\dot{\alpha}$.

$$L \cong 2\pi\rho_a U b [\dot{h} + U\alpha] \quad (4.4)$$

For the special purpose of correcting the sectional lift coefficient ' C_L ' to account for the influence of the aspect ratio ('AR= $\frac{2L_w}{c_m}$ ') and the sweep angle (' Λ '), Diederich's approximation is used

$$c_{l\alpha} = \frac{dC_L}{d\alpha} = \frac{\pi AR}{\pi AR + c_{l\alpha 0} \cos(\Lambda)} c_{l\alpha 0} \cos(\Lambda) \quad (4.5)$$

where ' L_w ' is the length of the wing, ' c ' is the mean chord (see Fig.5.38) and ' $c_{l\alpha 0}$ ' is the lift-curve slope, which is equal to 2π . Finally, since the quantity ' $b\pi'$ ' may be approximated with the integral $\int_{-b}^b \sqrt{\frac{b-x}{b+x}} dx$, which is able to reproduce the distribution of pressure over a slightly inclined, thin and uncambered airfoil, Eqs.4.1 and 4.4 become, respectively,

$$L = \frac{2\pi AR \cos(\Lambda)}{\pi AR + 2\pi \cos(\Lambda)} \int_{-b}^b \sqrt{\frac{b-x}{b+x}} dx \rho_a U C(k) \left[\dot{h} + U\alpha + b \left(\frac{1}{2} - a \right) \dot{\alpha} \right] \quad (4.6)$$

$$L \cong \frac{2\pi AR \cos(\Lambda)}{\pi AR + 2\pi \cos(\Lambda)} \int_{-b}^b \sqrt{\frac{b-x}{b+x}} dx \rho_a U [\dot{h} + U\alpha] \quad (4.7)$$

4.1.1 External work for the fixed-wing configuration

The equations of motion of a generic structure oscillating in an incompressible flow can be derived directly using Hamilton's Principle (Eq.3.1). The external work generated by lift can be written as

$$\delta L_{ext} = \int_y \int_x \delta u_z(x, y, z_{top}) L(x, y, z_{top}) dx dy \quad (4.8)$$

where ' z_{top} ' is the upper z-coordinate of the cross-section that, according to Eq.4.1, becomes

$$\delta L_{ext} = cost \left[\int_y \int_x \delta \mathbf{u}^T \sqrt{\frac{b-x}{b+x}} I_L \dot{\mathbf{u}} + \delta \mathbf{u}^T \sqrt{\frac{b-x}{b+x}} I_L \mathbf{u}_{,x} + \delta \mathbf{u}^T b \left(\frac{1}{2} - a \right) \sqrt{\frac{b-x}{b+x}} I_L \dot{\mathbf{u}}_{,x} \right] dx dy \quad (4.9)$$

where

$$\dot{h} = \dot{u}_z \quad \alpha = \frac{du_z}{dx} = u_{z,x} \quad \dot{\alpha} = \dot{u}_{z,x}$$

and

$$I_L = \begin{bmatrix} 0 & 0 & 0 \\ 0 & 0 & 0 \\ 0 & 0 & 1 \end{bmatrix} \quad cost = \frac{2\pi AR \cos(\Lambda)}{\pi AR + 2\pi \cos(\Lambda)} \rho_a U C(k)$$

By introducing Eqs.2.9 and 2.15 into Eq.4.9, we obtain

$$\delta L_{ext} = \delta \mathbf{q}_{\tau i}^T \mathbf{D}_L^{ij\tau s} \dot{\mathbf{q}}_{sj} + \delta \mathbf{q}_{\tau i}^T \mathbf{K}_L^{ij\tau s} \mathbf{q}_{sj} + \delta \mathbf{q}_{\tau i}^T \mathbf{D}_{Lm}^{ij\tau s} \dot{\mathbf{q}}_{sj} \quad (4.10)$$

where $\mathbf{D}_L^{ij\tau s}$, $\mathbf{K}_L^{ij\tau s}$, $\mathbf{D}_{Lm}^{ij\tau s}$ and $\mathbf{F}_L^{i\tau}$ are the aerodynamic contributions. The first and the third matrices introduce damping into the system, whereas the third matrix represents the aerodynamic stiffness. The last term is a forcing vector that can be overlooked in free-vibration analyses. The aforementioned matrices, written in terms of fundamental nuclei

$$\begin{aligned} \mathbf{D}_L^{ij\tau s} &= cost I_l^{ij} \triangleleft \left(\sqrt{\frac{b-x}{b+x}} F_{\tau}(x, z_{top}) \mathbf{I}_L F_s(x, z_{top}) \right) \triangleright_x \\ \mathbf{K}_L^{ij\tau s} &= cost I_l^{ij} \triangleleft \left(\sqrt{\frac{b-x}{b+x}} F_{\tau,x}(x, z_{top}) \mathbf{I}_L F_s(x, z_{top}) \right) \triangleright_x \quad \triangleleft \dots \triangleright_x = \int_{-b}^b \dots dx \\ \mathbf{D}_{Lm}^{ij\tau s} &= cost I_l^{ij} b \left(\frac{1}{2} - a \right) \triangleleft \left(\sqrt{\frac{b-x}{b+x}} F_{\tau,x}(x, z_{top}) \mathbf{I}_L F_s(x, z_{top}) \right) \triangleright_x \end{aligned} \quad (4.11)$$

Similarly to rotordynamics equations, the quadratic eigenvalue problem (QEP) of generic order R is transformed into a classical linear system of $2 \times R$ order:

$$\begin{cases} \mathbf{M} \ddot{\mathbf{q}} + (\mathbf{D}_L + \mathbf{D}_{Lm}) \dot{\mathbf{q}} + (\mathbf{K} + \mathbf{K}_L) \mathbf{q} = 0 \\ -\dot{\mathbf{q}} + \dot{\mathbf{q}} = 0 \end{cases} \quad (4.12)$$

introducing

$$\mathbf{a} = \begin{Bmatrix} \mathbf{q} \\ \dot{\mathbf{q}} \end{Bmatrix} \quad \dot{\mathbf{a}} = \begin{Bmatrix} \dot{\mathbf{q}} \\ \ddot{\mathbf{q}} \end{Bmatrix} \quad (4.13)$$

the equations of motion assume the form of Eq.3.37 where

$$\mathbf{T}^{-1} \mathbf{R} = \begin{bmatrix} (\mathbf{K} + \mathbf{K}_L)^{-1} (\mathbf{D}_L + \mathbf{D}_{Lm}) & (\mathbf{K} + \mathbf{K}_L)^{-1} \mathbf{M} \\ -\mathbf{I} & \mathbf{0} \end{bmatrix} \quad (4.14)$$

Since the aerodynamic matrices depend on the reduced frequency ' k ', the solutions are found by means of an iterative procedure (Nguyen, 2009). The frequencies are introduced by trial and error for any speed in the considered range, until Eq.3.37 is obtained. The flutter velocity is determined when the real part of one eigenvalue is null.

4.2 2-D unsteady aerodynamic theory for rotating lifting surfaces

According to Bielawa (1992), the general expression for the lift distribution on a rotary-wing yields

$$\frac{dL}{dy} = \pi \rho_a b^2 \Omega^2 \left[\frac{\ddot{h}}{\Omega^2} + \frac{\dot{\alpha}}{\Omega} - ba \frac{\ddot{\alpha}}{\Omega} \right] + 2\pi \rho_a b \Omega^2 C(k) \left[\frac{\dot{h}}{\Omega} + y\alpha + b \left(\frac{1}{2} - a \right) \frac{\dot{\alpha}}{\Omega} \right] \quad (4.15)$$

where, in this case, the reduced frequency ' k ' is

$$k = \frac{b}{3R} \frac{\omega}{\Omega}$$

In their study, the authors stated that this approach is limited as it relies on Theodorsen problem. However, it can be easily generalized as the unsteadiness is essentially described by the lift deficiency function. Hence, choosing different expressions of ' $C(k)$ ', it is possible to define several motion conditions. Since the rotating structure aerodynamic is more complex than its fixed-wing counterpart, it is useful to consider the physics of the flowfield near the rotor. The rotor vertical speed (' V_z ') and its thrust ($\propto C_T$) generate an inflow velocity through the disk that can be expressed as

$$u = \Omega R \left[\frac{V_z}{2} + \sqrt{\frac{V_z^2}{4} + \frac{C_T}{2}} \right]$$

In the general case, the rotor blade develops oscillating loads, which generate a radial distribution of vorticity blown downward at velocity ' u '. The wake can be described via models with increasing levels of complexity but, historically, the first successful attempt to incorporate the "returning wake" into the unsteady aerodynamics problem was proposed by Loewy (Loewy, 1957). The aerodynamic actions on a reference blade strongly depend on the shed vorticity of the previous revolutions as shown in Fig.4.1.

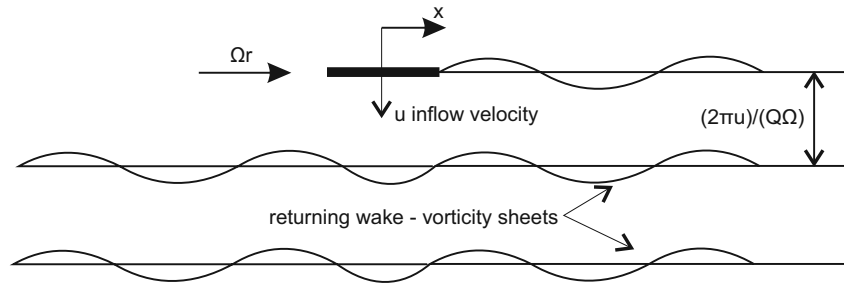


Figure 4.1 Schematic of the Loewy problem (Bielawa, 1992).

According to Loewy's theory, the returning wake is modelled as an infinite number of layers, which are equally spaced by a fixed distance, ' h_l ' semi-chords. Here, the factor ' h_l ' quantify the contribution of the underlying vortices to the lift distribution on the reference blade. The main difference with respect to Theodorsen's model lies in the form of the lift-deficiency function, which is (Dowell et al., 2004):

$$C'(k, m, h_l) = \frac{H_1^{(2)}(k) + 2J_1(k) W(km, h_l)}{H_1^{(2)}(k) + iH_0^{(2)}(k) + 2[J_1(k) + iJ_0(k)]W(km, h_l)} \quad (4.16)$$

where ' $J_n(k)$ ' and ' $H_n^{(2)}(k)$ ' are the first-kind Bessel and second-kind Hankel functions of order n , respectively. The wake weighting function ' $W(k, m, h_l)$ ' for a rotor with ' Q ' blades is defined as

$$W(k, m, h) = \frac{1 + \sum_{q=1}^{Q-1} (e^{kh_l Q} e^{i2\pi m})^{Q-q} e^{i\Phi_q}}{e^{kh_l Q} e^{i2\pi m} - 1} \quad (4.17)$$

where ' m ' and ' Φ_q ' are the ratio of oscillatory frequency to rotational frequency ($=\omega/\Omega$) and the phase angle between the q^{th} blade and the reference blade. Due to periodicity, Eq.4.17 can be expressed following the formulation for a single-blade rotor with the modified values ' \hat{m} ' and ' \hat{h} ':

$$W(k\hat{m}, \hat{h}) = \frac{1}{e^{k\hat{h}Q} e^{i2\pi\hat{m}} - 1} \quad \hat{m} = \frac{\omega}{Q\Omega} \quad \hat{h} = \frac{2\pi\lambda_0}{Q(b/r)} \quad (4.18)$$

where λ_0' is the inflow ratio ($\simeq \sqrt{C_T/2}$) and r' is a generic radial distance. Influence of the frequency ratio and the spacing factor on the Loewy's deficiency function is shown in Fig.4.2. As expected, Loewy's function $C(k)$ coincide with Theodorsen's expression for high values of spacing factor \hat{h}' .

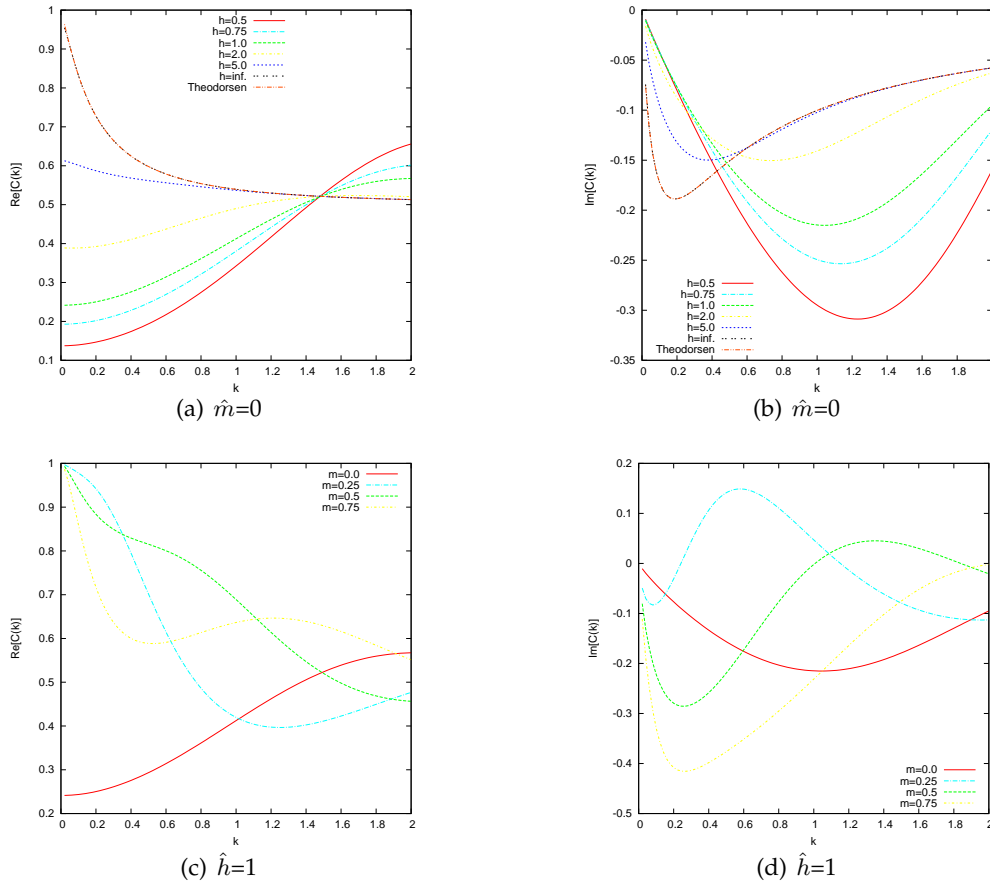


Figure 4.2 Real and Imaginary parts of the Loewy function vs ' k ' as functions of inflow parameter \hat{h} (a,b) and frequency ratio \hat{m} (c,d).

4.2.1 External work for the rotary-wing configuration

The external work defined in Eq.4.9 for a rotating blade is

$$\delta L_{ext} = \text{cost} \left[\int_y \int_x \delta \mathbf{u}^T \Omega y \sqrt{\frac{b-x}{b+x}} I_L \dot{\mathbf{u}} + \delta \mathbf{u}^T \Omega^2 y^2 \sqrt{\frac{b-x}{b+x}} I_L \mathbf{u}_{,x} dx dy \right] + \text{cost} \left[\int_y \int_x \delta \mathbf{u}^T \Omega y \sqrt{\frac{b-x}{b+x}} I_L b \left(\frac{1}{2} - a \right) \dot{\mathbf{u}}_{,x} dx dy \right] \quad (4.19)$$

where

$$\mathbf{I}_L = \begin{bmatrix} 0 & 0 & 0 \\ 0 & 0 & 0 \\ 0 & 0 & 1 \end{bmatrix} \quad cost = \frac{2\pi AR \cos(\Lambda)}{\pi AR + 2\pi \cos(\Lambda)} \rho_a C(k)$$

Introducing, again, the CUF and FEM approximations, we obtain Eq.4.10. The *fundamental nuclei* of the damping and stiffness aerodynamic matrices are

$$\begin{aligned} \mathbf{D}_L^{ij\tau s} &= cost \Omega I_{l_y}^{ij} \triangleleft \left(\sqrt{\frac{b-x}{b+x}} F_\tau(x, z_{top}) \mathbf{I}_L F_s(x, z_{top}) \right) \triangleright_x \\ \mathbf{K}_L^{ij\tau s} &= cost \Omega^2 I_{l_y,2}^{ij} \triangleleft \left(\sqrt{\frac{b-x}{b+x}} F_{\tau,x}(x, z_{top}) \mathbf{I}_L F_s(x, z_{top}) \right) \triangleright_x \quad \triangleleft \dots \triangleright_x = \int_{-b}^b \dots dx \\ \mathbf{D}_{Lm}^{ij\tau s} &= cost \Omega I_{l_y}^{ij} b \left(\frac{1}{2} - a \right) \triangleleft \left(\sqrt{\frac{b-x}{b+x}} F_{\tau,x}(x, z_{top}) \mathbf{I}_L F_s(x, z_{top}) \right) \triangleright_x \end{aligned} \quad (4.20)$$

Velocity varies linearly along the span, therefore yielding the integrals along the y -direction

$$\left(I_{l_y}^{ij}, I_{l_y,2}^{ij} \right) = \int_l \left(y N_i N_j, y^2 N_i N_j \right) dy$$

A solution is obtained following the procedure presented in Sec.4.2.1.

4.3 Panel Flutter of rotating plates: Piston Theory

In this section, the first-order piston theory is applied to rotating structures. Despite its simplicity, the piston theory provides accurate results in the supersonic range, with a Mach number 'M' (= 'flow speed' / 'speed of sound (V_s)') greater than $\sqrt{2}$. The flow on the panel is modelled as a one-dimensional flow in a channel (in a piston) and, no solutions for shock waves downstream of the plate are provided. According to (Carrera and Zappino, 2014a), the local differential pressure 'P' produced by the fluid over the rotating plate surface is

$$P(x, y, z_{top}) = \left(\frac{\rho_a U^2}{\beta} \right) \alpha + \frac{\rho_a U}{\beta} \left(\frac{M^2 - 2}{M^2 - 1} \right) \dot{h} \quad (4.21)$$

where

$$\begin{aligned} \alpha &= \frac{du_z}{dx} & \dot{h} &= \dot{u}_z \\ M &= \frac{U}{V_s} & U &= \Omega \bar{y} & \beta &= \sqrt{M^2 - 1} \end{aligned}$$

4.3.1 External work for a rotating structure

As previously done, the work due to the external loading is written as

$$\delta L_{ext} = \int_y \int_x \delta u_z(x, y, z_{surf}) P(x, y, z_{surf}) dx dy \quad (4.22)$$

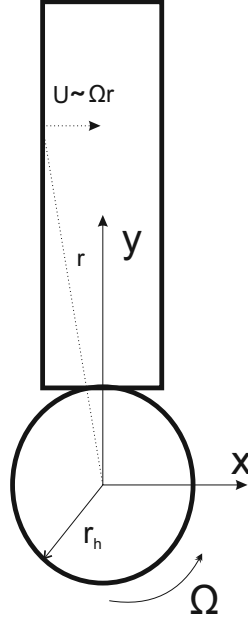


Figure 4.3 Geometry of the rotating plate.

where $'z_{surf}'$ is the z -coordinate of the flow-wetted surface. Substituting Eq.4.21 and introducing both CUF and FE approximations, Eq.4.22 becomes

$$\delta L_{ext} = \int_y \int_x \delta \mathbf{u}^T \left(\frac{\rho_a U^2}{\beta} \right) \mathbf{I}_L \mathbf{u}_{,x} + \mathbf{u}^T \left(\frac{\rho_a U}{\beta} \right) \left(\frac{M^2 - 2}{M^2 - 1} \right) \mathbf{I}_L \dot{\mathbf{u}} \, dx \, dy \quad (4.23)$$

From Eq. 4.23, introducing Eq.s 2.9 and 2.15, we obtain

$$\delta L_{ext} = \delta \mathbf{q}_{\tau i}^T \mathbf{K}_L^{ij\tau s} \dot{\mathbf{q}}_{sj} + \delta \mathbf{q}_{\tau i}^T \mathbf{D}_L^{ij\tau s} \dot{\mathbf{q}}_{sj} \quad (4.24)$$

where $\mathbf{K}_L^{ij\tau s}$ and $\mathbf{D}_L^{ij\tau s}$ are the aerodynamic damping and stiffness contributions, respectively. Writing these matrices in terms of fundamental nuclei

$$\begin{aligned} \mathbf{K}_L^{ij\tau s} &= I_l^{ij} \triangleleft \left(\left(\frac{\rho_a U^2}{\beta} \right) F_{\tau,x}(x, z_{surf}) \mathbf{I}_L F_s(x, z_{top}) \right) \triangleright_x \\ \mathbf{L}_L^{ij\tau s} &= I_l^{ij} \triangleleft \left(\left(\frac{\rho_a U}{\beta} \right) \left(\frac{M^2 - 2}{M^2 - 1} \right) F_{\tau}(x, z_{surf}) \mathbf{I}_L F_s(x, z_{top}) \right) \triangleright_x \end{aligned} \quad \triangleleft \dots \triangleright_x = \int_{-b}^b \dots \, dx \quad (4.25)$$

Finally, we obtain

$$\mathbf{T}^{-1} \mathbf{R} = \begin{bmatrix} (\mathbf{K} + \mathbf{K}_L + \mathbf{K}_{\Omega} + \mathbf{K}_{\sigma 0})^{-1} (\mathbf{D}_L + \mathbf{G}_{\Omega}) & (\mathbf{K} + \mathbf{K}_L + \mathbf{K}_{\Omega} + \mathbf{K}_{\sigma 0})^{-1} \mathbf{M} \\ -\mathbf{I} & \mathbf{0} \end{bmatrix} \quad (4.26)$$

Chapter 5

Numerical Results and discussion

This chapter aims to present a number of numerical results obtained with the 1D-CUF finite elements. Firstly, static and free-vibration analyses are carried out on structures made of orthotropic and FG materials. Several geometries are studied including compact and thin-walled cross-sections with open and closed profile. Secondly, the results derived by the dynamic analyses of rotating structures are shown highlighting the differences between the classical and refined theories. Finally, the flutter phenomenon for fixed and rotating systems is evaluated for subsonic and supersonic flows.

Nomenclature used to denote various expansions

Using the ESL approach, several expansions are evaluated and listed in Table 5.1. In the following, abbreviations stand for

- functions with single trigonometric factor:

$$\begin{aligned} sx &= \sin\left(m\frac{\pi x}{a}\right) & cx &= \cos\left(m\frac{\pi x}{a}\right) & sz &= \sin\left(n\frac{\pi z}{b}\right) & cz &= \cos\left(n\frac{\pi z}{b}\right) \\ sd &= \sin\left(m\frac{\pi xz}{ab}\right) & cd &= \cos\left(m\frac{\pi xz}{ab}\right) \end{aligned}$$

- functions with two trigonometric factors:

$$\begin{aligned} cc &= \cos\left(m\frac{\pi x}{a}\right) \cos\left(n\frac{\pi z}{b}\right) & cs &= \cos\left(m\frac{\pi x}{a}\right) \sin\left(n\frac{\pi z}{b}\right) \\ sc &= \sin\left(m\frac{\pi x}{a}\right) \cos\left(n\frac{\pi z}{b}\right) & ss &= \sin\left(m\frac{\pi x}{a}\right) \sin\left(n\frac{\pi z}{b}\right) \end{aligned}$$

- hyperbolic functions:

$$chx = \cosh(mx) \quad shx = \sinh(mx) \quad chz = \cosh(nz) \quad shz = \sinh(nz)$$

- exponential functions:

$$expx = e^{(mx)} \quad expz = e^{(nz)}$$

◦ polynomial functions:

$$xz = x^m z^n \quad z = z^n$$

The indexes m and n indicate summation, and they represent different parameters according to the adopted functions. For trigonometric functions, m and n are the half-wave numbers

$$sx = \sin\left(m\frac{\pi x}{a}\right) = \sum_{m=1}^N \sin\left(m\frac{\pi x}{a}\right) = \sin\left(\frac{\pi x}{a}\right) + \sin\left(2\frac{\pi x}{a}\right) + \dots + \sin\left(N\frac{\pi x}{a}\right)$$

$$cc = \cos\left(m\frac{\pi x}{a}\right) \cos\left(n\frac{\pi z}{b}\right) = \sum_{m=0}^N \sum_{n=0}^N \cos\left(m\frac{\pi x}{a}\right) \cos\left(n\frac{\pi z}{b}\right)$$

For exponential and polynomial functions, n and m represent exponents:

$$expx = e^{mx} = \sum_{m=1}^N e^{mx} = 1 + e^x + e^{2x} + \dots + e^{Nx}$$

$$xz = \sum_{n=1}^N \sum_{m=1}^{n-1} x^{n-m} z^m = xz + x^2 z + xz^2 + x^3 z + x^2 z^2 + xz^3 + \dots + x^{N-1} z + \dots + xz^{N-1}$$

On the bases of these explicit formulations, the expansions introduced in Tab.5.1 can be written in the extended form

E1-N:

$$\mathbf{u}(x, y, z, t) = \mathbf{u}_1(y, t) + \sin\left(m\frac{\pi x}{a}\right) \mathbf{u}_{(2m)}(y, t) + \sin\left(m\frac{\pi z}{b}\right) \mathbf{u}_{(2m+1)}(y, t)$$

E2-N:

$$\mathbf{u}(x, y, z, t) = \mathbf{u}_1(y, t) + \sin\left(m\frac{\pi x}{a}\right) \mathbf{u}_{(4m-2)}(y, t) + \sin\left(m\frac{\pi z}{b}\right) \mathbf{u}_{(4m-1)}(y, t) + \\ + \cos\left(m\frac{\pi x}{a}\right) \mathbf{u}_{(4m)}(y, t) + \cos\left(m\frac{\pi z}{b}\right) \mathbf{u}_{(4m+1)}(y, t)$$

E3-N:

$$\mathbf{u}(x, y, z, t) = \mathbf{u}_1(y, t) + \sin\left(m\frac{\pi x}{a}\right) \mathbf{u}_{(6m-4)}(y, t) + \sin\left(m\frac{\pi z}{b}\right) \mathbf{u}_{(6m-3)}(y, t) + \\ + \cos\left(m\frac{\pi x}{a}\right) \mathbf{u}_{(6m-2)}(y, t) + \cos\left(m\frac{\pi z}{b}\right) \mathbf{u}_{(6m-1)}(y, t) + \\ + \sin\left(m\frac{\pi xz}{ab}\right) \mathbf{u}_{(6m)}(y, t) + \cos\left(m\frac{\pi xz}{ab}\right) \mathbf{u}_{(6m+1)}(y, t)$$

E4-N:

$$\mathbf{u}(x, y, z, t) = \mathbf{u}_1(y, t) + e^{(mx)} \mathbf{u}_{(2m)}(y, t) + e^{(mz)} \mathbf{u}_{(2m+1)}(y, t)$$

E5-N:

$$\mathbf{u}(x, y, z, t) = \mathbf{u}_1(y, t) + e^{(mx)} \mathbf{u}_{(4m)}(y, t) + e^{(mz)} \mathbf{u}_{(4m+1)}(y, t) + \\ + \sin\left(m\frac{\pi x}{a}\right) \mathbf{u}_{(4m-2)}(y, t) + \sin\left(m\frac{\pi z}{b}\right) \mathbf{u}_{(4m-1)}(y, t)$$

E6-N:

$$\mathbf{u}(x, y, z, t) = \mathbf{u}_1(y, t) + \sinh(mx) \mathbf{u}_{(4m-2)}(y, t) + \sinh(mz) \mathbf{u}_{(4m-1)}(y, t) + \\ + \cosh(mx) \mathbf{u}_{(4m)}(y, t) + \cosh(mz) \mathbf{u}_{(4m+1)}(y, t)$$

E7-N:

$$\mathbf{u}(x, y, z, t) = \mathbf{u}_1(y, t) + \sinh(mx) \mathbf{u}_{(6m-4)}(y, t) + \sinh(mz) \mathbf{u}_{(6m-3)}(y, t) + \\ + \cosh(mx) \mathbf{u}_{(6m-2)}(y, t) + \cosh(mz) \mathbf{u}_{(6m-1)}(y, t) + \\ + \sin\left(m\frac{\pi x}{a}\right) \mathbf{u}_{(6m)}(y, t) + \sin\left(m\frac{\pi z}{b}\right) \mathbf{u}_{(6m+1)}(y, t)$$

For the expansion E8 is shown explicitly

E8-3:

$$\mathbf{u}(x, y, z, t) = \mathbf{u}_1(y, t) + \sin\left(\frac{\pi x}{a}\right) \mathbf{u}_2(y, t) + \sin\left(\frac{\pi z}{b}\right) \mathbf{u}_3(y, t) + \\ + \sin\left(\frac{2\pi x}{a}\right) \mathbf{u}_4(y, t) + \sin\left(\frac{2\pi z}{b}\right) \mathbf{u}_5(y, t) + xz \mathbf{u}_6(y, t) + \\ + \sin\left(\frac{3\pi x}{a}\right) \mathbf{u}_7(y, t) + \sin\left(\frac{3\pi z}{a}\right) \mathbf{u}_8(y, t) + x^2 z \mathbf{u}_9(y, t) + \\ + xz^2 \mathbf{u}_{10}(y, t)$$

E9-N:

$$\mathbf{u}(x, y, z, t) = \cos\left(m\frac{\pi x}{a}\right) \cos\left(n\frac{\pi z}{b}\right) \mathbf{u}_{m,n}(y, t) + \cos\left(m\frac{\pi x}{a}\right) \sin\left(n\frac{\pi z}{b}\right) \mathbf{u}_{m,n}(y, t) + \\ + \sin\left(m\frac{\pi x}{a}\right) \cos\left(n\frac{\pi z}{b}\right) \mathbf{u}_{m,n}(y, t) + \sin\left(m\frac{\pi x}{a}\right) \sin\left(n\frac{\pi z}{b}\right) \mathbf{u}_{m,n}(y, t)$$

E10-N:

$$\mathbf{u}(x, y, z, t) = \mathbf{u}_1(y, t) + z^n \mathbf{u}_{n+1}(y, t)$$

If Taylor-like expansions are added to displacement fields, their order is specified by the subscript. For instance, the first component of $E2_2$ displacement field becomes

$$u_x = \cos t u_{x_1} + \sin\left(\frac{\pi x}{a}\right) u_{x_2} + \cos\left(\frac{\pi x}{a}\right) u_{x_3} + \sin\left(\frac{\pi z}{b}\right) u_{x_4} + \cos\left(\frac{\pi z}{b}\right) u_{x_5} + \\ + \sin\left(2\frac{\pi x}{a}\right) u_{x_6} + \cos\left(2\frac{\pi x}{a}\right) u_{x_7} + \sin\left(2\frac{\pi z}{b}\right) u_{x_8} + \cos\left(2\frac{\pi z}{b}\right) u_{x_9} + \\ + x u_{x_{10}} + z u_{x_{11}} + x^2 u_{x_{12}} + xz u_{x_{13}} + z^2 u_{x_{14}}$$

5.1 Static Analyses

Convergency Analysis

A cantilever beam with aspect-ratio equal to 100 is here considered. The material is aluminum with Young Modulus and Poisson ratio equal to 73 GPa and 0.34, respectively. The cross-section is square and a concentrated load ($F_z = -25 N$) is applied at the free tip. The reference solution is provided by the following formula

$$u_z(y = L) = \frac{F_z L^3}{3EI} \quad (5.1)$$

A convergence study is performed to investigate the effect of the number of the mesh elements and the order of the expansion on the transverse displacement evaluated at the loading point (see Tab.5.2). In this case, the convergence is achieved for n_e equal to 10.

Table 5.1 Expansions used in the analyses.

	<i>E1</i>	<i>E2</i>	<i>E3</i>	<i>E4</i>	<i>E5</i>	<i>E6</i>	<i>E7</i>	<i>E8</i>	<i>E9</i>	<i>E10</i>
<i>cost</i>	✓	✓	✓	✓	✓	✓	✓	✓	✓	✓
<i>sx</i>	✓	✓	✓		✓		✓	✓		
<i>cx</i>		✓	✓							
<i>sz</i>	✓	✓	✓		✓		✓	✓		
<i>cz</i>		✓	✓							
<i>sd</i>			✓							
<i>cd</i>			✓							
<i>exp_x</i>				✓	✓					
<i>exp_z</i>				✓	✓					
<i>sh_x</i>						✓	✓			
<i>ch_x</i>						✓	✓			
<i>sh_z</i>						✓	✓			
<i>ch_z</i>						✓	✓			
<i>cc</i>									✓	
<i>cs</i>									✓	
<i>sc</i>									✓	
<i>ss</i>									✓	
<i>xz</i>								✓		
<i>z</i>										✓

Table 5.2 Effect of the number (n_e) of elements B4 on $-u_z$ ($\times 10^{-3}$ [m]). Loading case: bending.

N	$n_e = 1$	$n_e = 5$	$n_e = 10$	$n_e = 30$
<i>CBT</i>	1.3703	1.3703	1.3703	1.3703
<i>FOBT</i>	1.3704	1.3704	1.3704	1.3704
<i>TE₁</i>	1.3704	1.3704	1.3704	1.3704
<i>TE₃</i>	1.2728	1.3442	1.3534	1.3597
<i>TE₅</i>	1.2840	1.3541	1.3627	1.3684
Ref.eq.(5.1)=1.3698				

CBT stands for Classical beam theory.

FOBT stands for First-order beam theory.

5.1.1 Laminated compact beams

This section shows the results obtained for cantilevered symmetric ($0^0/90^0/0^0$) and antisymmetric ($0^0/90^0$) cross-ply laminated beams constituted by orthotropic material. All laminae have the same thickness and, if not otherwise specified, the dimensionless material properties adopted are:

$$E_A/E_T = 25 \quad G_{AT}/G_{TT} = 2.5 \quad \nu_{AT} = 0.1 \quad \nu_{TT} = 0.3$$

where A refers to the fiber direction and T refers to the normal direction.

For sake of convenience, the results are presented in non-dimensional form:

$$\bar{u}_z = 100 \frac{bh^3 E_T}{q_0 L^4} u_z, \quad \bar{\sigma}_{ij} = \frac{\sigma_{ij}}{q_0}, \quad \text{with} \quad i, j = x, y, z$$

where L is the length of the beam, b and h the dimensions of the rectangular cross-section and q_0 the intensity of the distributed load. The structures are modelled with ten finite elements. The displacement of the tip, the stresses $\bar{\sigma}_{yy}$ and $\bar{\sigma}_{zz}$ are compared with those obtained by using the solid elements *HEX20* of *MSC NASTRAN*[©] (Tab.5.3 and 5.4). For both structures, it is worth noting that expansion *E4*, where exponential functions are used, leads to results that strongly agree with the reference solutions. With a comparable number of degrees of freedom, the expansion *E1* provides good results both in term of displacement and longitudinal stress $\bar{\sigma}_{yy}$ whereas, for stress $\bar{\sigma}_{zz}$, the solution appears inadequate. Furthermore, in the last column of Tab.5.3, the ratio between the CPU time using the expansion and Euler-Bernoulli theory is shown. These values give information about the real computational effort required by refined theories. Although the ratios can reach high values (200-300), the computation time with a common laptop is around few seconds.

The importance of the zig-zag function is evident in Figs.5.1 and 5.2 where distributions through-the-thickness of the non-dimensional stresses ($\bar{\sigma}_{yy}$, $\bar{\sigma}_{zz}$ and $\bar{\sigma}_{yz}$) are shown for several kinds of expansions. Figures labeled with (*a-c-e*) refer to expansions without the zig-zag term whereas figures (*b-d-f*) show the distributions when this term is included. Results demonstrate that the combination of different functions by introducing the discontinuity of the first derivative of displacements allows to obtain quasi-3D solutions with very low computational efforts.

Table 5.3 Non-dimensional displacements and stresses of a symmetric cross-ply beam under an uniform distributed load. σ_{yy} at $(b/2; 0; -0.367h)$ and σ_{zz} at $(b/2; L/2; h/2)$. $L/h = 4$

	N	$-\bar{u}_z$	$-\bar{\sigma}_{yy}^-$	$-\bar{\sigma}_{zz}^+$	DOFs	t/t_{CBT}
<i>Nastran</i>		17.9754	30.5844	1.0278	103920	
<i>EBBT</i>		6.2245	36.5184	0.0000	279	1
<i>FSDT</i>		14.0223	36.5184	0.0000	279	1
<i>TE1</i>		14.0224	36.5184	0.4958	279	4
	<i>zz</i>	17.3328	38.0646	0.4475	372	6
<i>TE2</i>		14.0154	36.3298	0.9368	558	13
	<i>zz</i>	17.3060	37.8849	1.0556	651	16
<i>TE3</i>		16.7647	28.3861	1.0439	930	33
	<i>zz</i>	17.7591	31.1710	1.0203	1023	40
<i>TE6</i>		17.1384	25.2949	0.9950	2604	271
	<i>zz</i>	17.8371	27.3629	1.0323	2697	273
<i>E1</i>	5	17.5913	31.1008	0.4238	1023	55
	5^{zz}	17.9017	30.0005	0.4251	1116	63
<i>E2</i>	5	17.5352	30.9342	0.9435	1953	148
	5^{zz}	17.8420	29.8032	0.9352	2046	161
<i>E4</i>	7	17.3130	26.6598	0.9450	1395	76
	7^{zz}	17.8397	26.2546	0.9135	1488	86
<i>E6</i>	4	17.4534	32.3089	0.9145	1581	100
	4^{zz}	17.8407	29.2543	0.9013	1674	122

Table 5.4 Non-dimensional displacements and stresses of an antisymmetric cross-ply beam under an uniform distributed load. σ_{yy} at $(b/2;0;-0.328h)$ and σ_{zz} at $(b/2;L/2;h/2)$. $L/h = 4$

	N	\bar{u}_z	$\bar{\sigma}_{yy}^-$	$-\bar{\sigma}_{yy}^+$	$-\bar{\sigma}_{zz}^+$	$DOFs$
<i>Nastran</i>		43.0937	36.1128	11.4270	1.0239	198300
<i>EBBT</i>		31.9645	50.0290	11.4394	0.0000	279
<i>FSDT</i>		40.8757	50.0290	11.4394	0.0000	279
<i>TE1</i>		40.8609	50.0290	11.4394	0.3887	279
	<i>zz</i>	41.2077	48.2077	13.0898	0.6001	372
<i>TE2</i>		40.9202	50.3749	13.2647	0.9811	558
	<i>zz</i>	41.0123	48.3814	13.6445	0.9270	651
<i>TE3</i>		41.6311	36.7505	12.8075	1.1380	930
	<i>zz</i>	41.6610	39.2040	11.2977	1.0460	1023
<i>TE6</i>		42.1657	33.9530	10.8486	0.9599	2604
	<i>zz</i>	42.2660	32.0183	10.7739	0.9232	2697
<i>E1</i>	5	41.0128	38.9804	12.0684	0.1919	1023
	<i>5^{zz}</i>	41.9098	37.8884	13.2106	0.4934	1116
<i>E2</i>	5	42.2677	38.8214	11.9479	0.9503	1953
	<i>5^{zz}</i>	42.3232	39.9750	11.8412	0.9267	2046
<i>E4</i>	7	42.2131	33.2601	11.7440	0.9671	1395
	<i>7^{zz}</i>	42.2895	31.5211	11.8038	0.9559	1488
<i>E6</i>	4	42.2211	36.4385	11.4997	0.8818	1581
	<i>4^{zz}</i>	42.3144	41.9019	11.1968	0.9304	1674

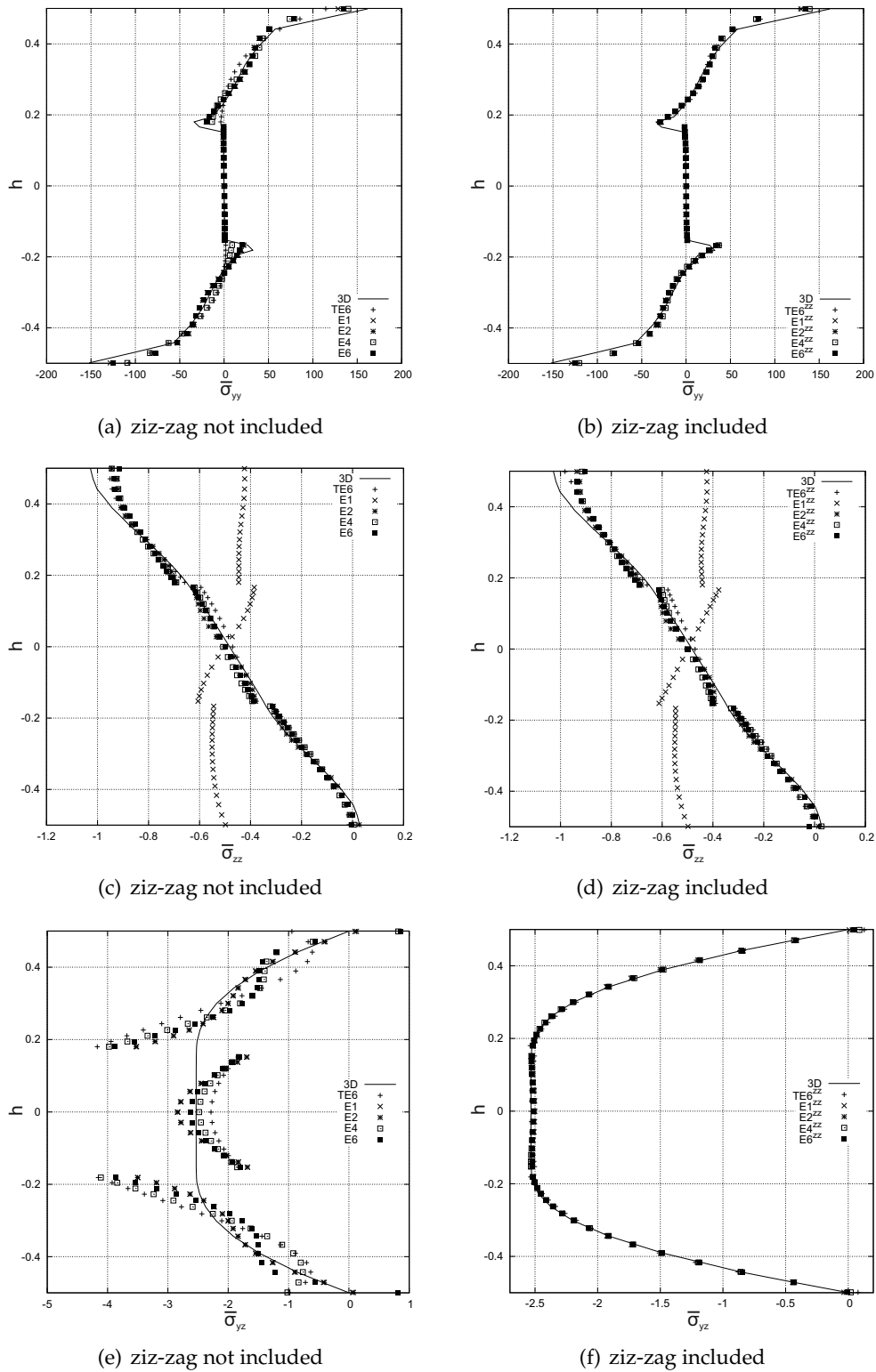
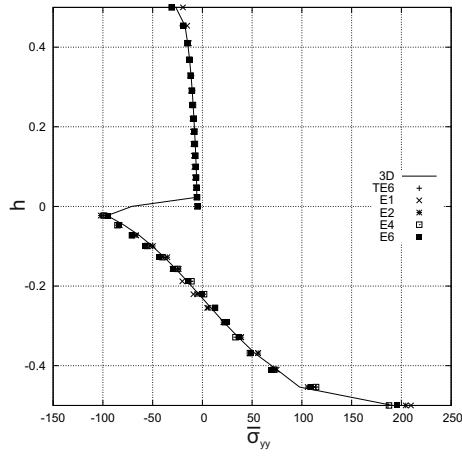
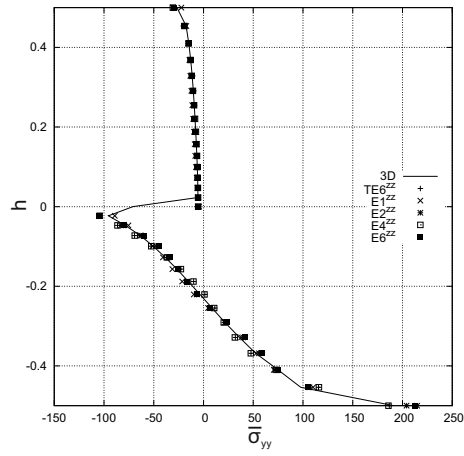


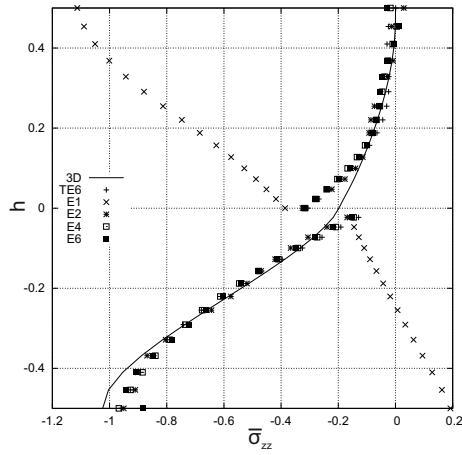
Figure 5.1 Distribution of stresses $\bar{\sigma}$ through-the-thickness of a symmetric cantilever beam ($L/h=4$).



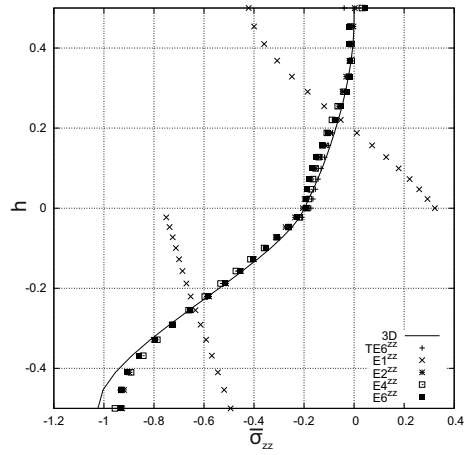
(a) ziz-zag not included



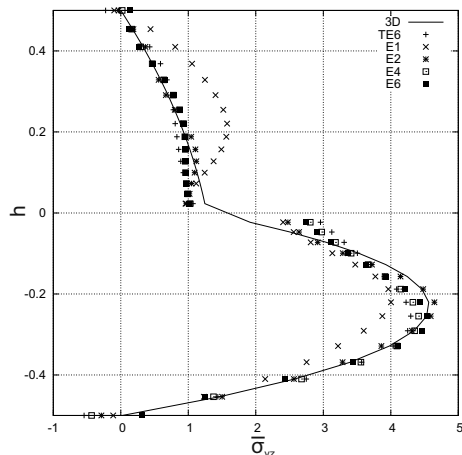
(b) ziz-zag included



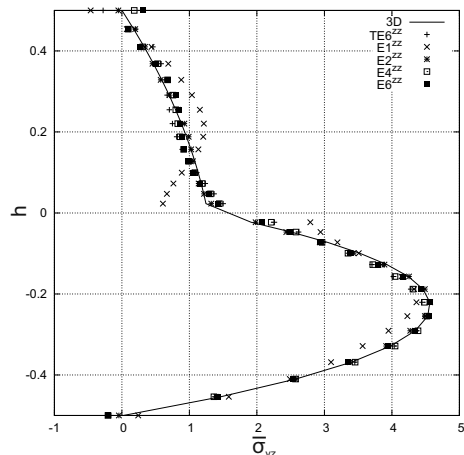
(c) ziz-zag not included



(d) ziz-zag included



(e) ziz-zag not included



(f) ziz-zag included

Figure 5.2 Distribution of stresses $\bar{\sigma}$ through-the-thickness of an anti-symmetric cantilever beam ($L/h=4$).

5.1.2 Functionally Graded Structures

The rectangular cross-section FG beam

First of all, a rectangular cross-section beam is considered to assess the theory. The aspect ratio of the cross-section (a/h) is assumed to be equal to 0.01 in order to neglect the effects in the width-wise direction. The structure is subjected to a sinusoidal pressure that can act either on the top (z_T) or bottom (z_B) surface, whose distribution is

$$p(x, y) = p_{zz} \sin\left(\frac{\pi}{L} y\right) \quad p_{zz} = 1 \quad (5.2)$$

where 'L' is the length of the beam. The Young's modulus $E(x, z)$ varies with the exponential law in Eq.5.3 so that the ratio $E(x, z_T)/E(x, z_B)=10$ with $E(x, z_B) = 1000$.

$$E(x, z) = E(x, z_B) e^{\alpha_1 x + \beta_1} e^{\alpha_2 z + \beta_2} \quad (5.3)$$

Two length-to-thickness ratios (L/h) are considered and the results are compared with those available in Giunta et al. (2010). In their analysis, Giunta *et al.* provided closed form solutions using CUF, and higher-order displacement theories were obtained adopting Taylor-type expansions: the relative results were validated by solutions available in the literature. The transverse displacement and stresses are reported in the following non-dimensional forms

$$\bar{u}_z = \frac{u_z}{h} \quad \bar{\sigma}_{ij} = \frac{\sigma_{ij}}{p_{zz}}$$

The structure is simply supported and it is modelled using ten 4-node beam (B4) elements. Tables 5.5 and 5.6 show the results for L/h equal to 10 and 2.5, respectively.

Table 5.5 Transverse displacement and stresses for $L/h = 10$, $\nu=0.25$ and loading acting at z_T

Theory	$10\bar{u}_z(L/2, z_B)$	$\bar{\sigma}_{yy}(L/2, -h/2)$	$\bar{\sigma}_{yz}(0, 0)$	DOF
EBBT Ref.(Giunta et al., 2010)	-4.0311	26.928	-	
FSDT Ref.(Giunta et al., 2010)	-4.0959	26.928	-2.5753	
TE3 Ref.(Giunta et al., 2010)	-4.0938	26.942	-4.3468	
TE7 Ref.(Giunta et al., 2010)	-4.0942	26.922	-4.4527	
EBBT	-4.0308	26.926	-	279
FSDT	-4.0955	26.926	-2.5816	279
TE3	-4.0934	26.940	-4.3530	930
TE7	-4.0938	26.920	-4.4588	3348
E2-5 ₂	-4.0938	26.922	-4.4587	2418
E10-4 ₂	-4.0938	26.923	-4.4583	930
E10-9 ₂	-4.0938	26.922	-4.4587	1395

EBBT: Euler-Bernoulli Beam Theory.

FSDT: First-order Shear Deformation Theory.

-: results not provided by the model.

As far as classical and TE beam models are concerned, the finite element solutions agree with the analytical approach for both cases. Moreover, Fig. 5.3 shows the stress distributions through the thickness of the shortest beam for different displacement models.

Table 5.6 Transverse displacement and stresses for $L/h = 2.5$, $\nu=0.3$ and loading acting at z_B

Theory	$\sigma_{yy}^-(L/2,-h/2)$	$\sigma_{yy}^-(L/2,h/2)$	$\sigma_{yz_{max}}^-$	DOF
EBBT Ref.(Giunta et al., 2010)	-1.6830	8.0363	-	
FSDT Ref.(Giunta et al., 2010)	-1.6830	8.0360	2.0359	
TE3 Ref.(Giunta et al., 2010)	-1.8354	8.5441	1.3554	
TE8 Ref.(Giunta et al., 2010)	-1.8175	8.4440	1.2822	
EBBT	-1.6830	8.0363	-	279
FSDT	-1.6830	8.0363	2.0362	279
TE3	-1.8355	8.5445	1.3548	930
TE8	-1.8175	8.4420	1.2807	4185
E2-5 ₂	-1.8615	8.3784	1.2750	2418
E10-4 ₂	-1.8620	8.3809	1.2753	930
E10-9 ₂	-1.8629	8.3827	1.2750	1395

EBBT: Euler-Bernoulli Beam Theory.

FSDT: First-order Shear Deformation Theory.

-: results not provided by the model.

It should be noted that the E10-4₂ expansion leads to accurate results with a very low number of degrees of freedom (DOF¹). This is due to the fact that the beam can be considered in a state of plane stress (in yz -plane), which allows to disregard the x -terms in the TE expansions since the transverse stresses are dominant over those along the width.

The multi-layer FG beam

A cantilevered three-layer beam is here considered. The length 'L', the width 'a' and the whole thickness 'h' of the structure are 2.5, 0.5 and 1 m, respectively. The layers are made of functionally graded materials, whose Young's moduli 'E(x,z)' follow three different gradation functions (linear, exponential and sigmoid):

$$-0.5 < z < -0.3 : E(z) = 400 \times 10^9 z + 270 \times 10^9 ;$$

$$-0.3 < z < 0.0 : E(z) = 150 \times 10^9 e^{\frac{z}{0.3} \left(\ln \left(\frac{250}{150} \right) \right) + \frac{250}{150}} ;$$

$$0.0 < z < 0.25 : E(z) = 250 \times 10^9 V(z) + 380 \times 10^9 (1 - V(z)) \text{ where } V(z) = 1 - \frac{1}{2} \left(1 - \frac{2(z-0.25)}{0.5} \right)^3$$

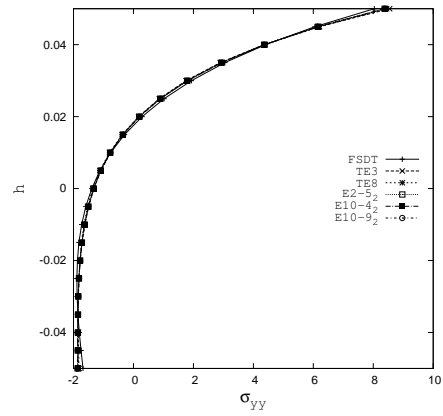
$$0.25 < z < 0.5 : E(z) = 250 \times 10^9 V(z) + 380 \times 10^9 (1 - V(z)) \text{ where } V(z) = \frac{1}{2} \left(1 + \frac{2(z-0.25)}{0.5} \right)^3$$

The Poisson's ratio is considered constant and equal to 0.25 for all layers and the structure undergoes to a distributed pressure equal to 1 MPa. The beam is modelled with ten 4-node finite elements along the y -axis. For comparison purposes, a finite element solution is provided, where solid elements HEX 8 are used. The mechanical properties are defined in the centroid of each element and, in order to correctly describe the materials distribution, 25, 10 and 50

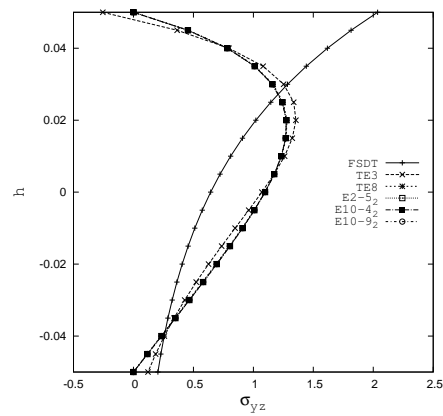
¹ DOF = $3 \times N_{nodes} \times T$, in which ' N_{nodes} ' is the number of structural nodes and 'T' the number of terms in the expansion.

elements are used along the length, the width and the thickness, respectively. The total number of degrees of freedom of the 3D model is therefore equal to 42075. Figures 5.4 show the transverse and axial displacements obtained with a number of beam theories in which polynomial, trigonometric as well as exponential functions are used. Because of shear effects, the transverse displacement has a non-linear variation along the thickness, and the beam results are slightly lower than the solid solution. Moreover, it is noteworthy that the FSDT predicts a constant value of u_z . The axial displacements in Fig. 5.4-b perfectly match the reference solution. Regarding the stress distributions, Fig.5.5 shows that the considered refined displacement theories lead to quite accurate results. However, slightly different stress distributions are presented in Fig.5.6.

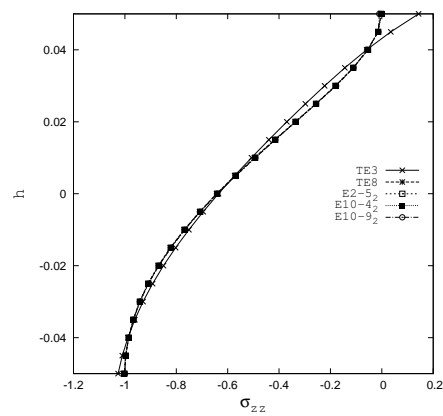
S



(a)



(b)



(c)

Figure 5.3 Stress distributions through the thickness. FGM beam aspect-ratio 2.5.

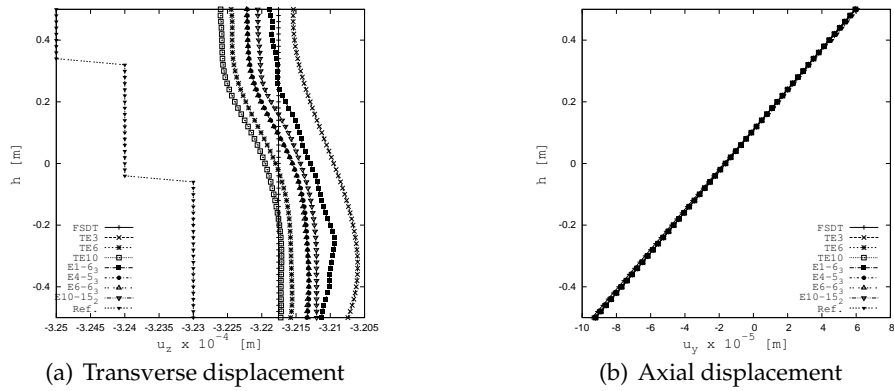


Figure 5.4 Displacements along the thickness of the three-layered FG beam at $y=L$.

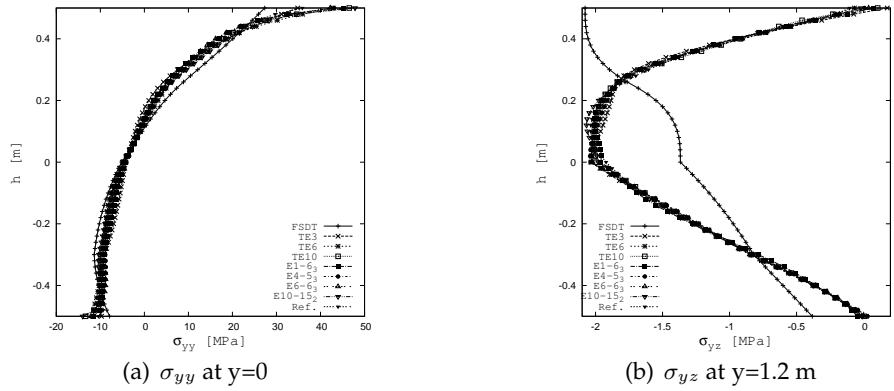


Figure 5.5 Stresses along the thickness of the three-layered FG beam.

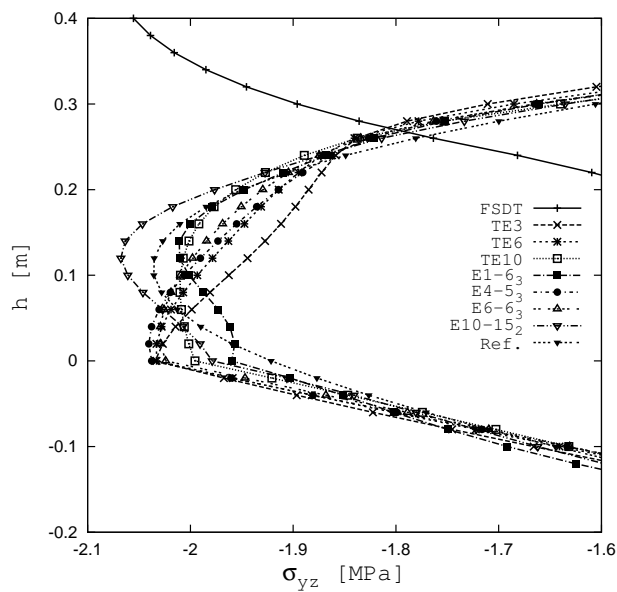


Figure 5.6 Zoom of the shear stress σ_{yz} distribution along the thickness of the three-layered FG beam.

5.2 Free-Vibration Analyses

5.2.1 Laminated compact beams

In the first two examples, symmetric ($0^0/90^0/0^0$) and antisymmetric ($0^0/90^0$) cross-ply laminated beams are studied. The effect of the beam dimensions and lamination on the natural frequencies and modes as well as on the accuracy of the proposed theories is investigated. The simply supported beams are constituted by orthotropic material, whose properties are:

$$E_L/E_T = 25 \quad G_{LT}/G_{TT} = 2.5 \quad \nu_{LT} = \nu_{TT} = 0.25$$

where L refers to the fiber direction and T refers to the normal direction. All laminae are assumed to be of the same thickness. For convenience, the natural angular frequencies² are presented in dimensionless form:

$$\bar{\omega} = \frac{L^2}{b} \sqrt{\frac{\rho}{E_T}} \omega$$

where L is the length of the beam and b the width of cross-section. The results are compared with those found in (Giunta et al., 2013) where the authors provided closed form solutions using CUF. The higher-order displacement theories were obtained adopting Taylor-type expansions and the relative results were assessed with three-dimensional FEM solutions. In Tabs.5.7 and 5.8, the dimensionless frequencies of the symmetric beams are shown, for length-to-thickness ratios equal to 10 and 5, respectively. The first two modal shapes are pure flexural modes, which occur in different planes. When the beam becomes thicker, these modes interchange their order of appearance and, only with higher order displacement models, the "modal swapping" becomes detectable. For both cases, the use of zig-zag function substantially improves the accuracy of results for the flexural modal shape in yz -plane, while, for the remaining mode of deformation, the most efficient models are the Taylor-type expansions and E8. By contrast, the third mode involves a torsional deformation, whose natural frequency is computed with acceptable accuracy adopting the theories with the xz term (in other words, Taylor-type expansions and E8). The last two modes involves shear deformations which are typically detected by using 3D elements. For the sake of clarity, Fig.5.7 shows these modal shapes computed with the expansion TE6. The axial/shear deformation appears as fourth and fifth mode, respectively. By comparing the results it is shown that the frequency values obtained with TE8 and E2 are close to the reference solutions for both values of length-to thickness ratios. Regarding the last shear modes, the zig-zag function once again enables a significant improvement of the solutions, indeed, if we consider TE3 expansion for L/h equal to 10, the relative error decreases from 6% to 0.2%. An antisymmetric laminated beam with length-to-thickness ratio equal to 5 is considered. The dimensionless angular frequencies are shown in Tab.5.9. For this case, the five modal shapes are: flexural on yz -plane, flexural/torsional on xy -plane, torsional, axial/shear and shear on xy -plane, respectively. For sake of clarity, the latter two deformation modes are shown in Fig.5.7-c and 5.7-d. Classical models are intrinsically unable to detect the torsional mode and the shear mode, hence, variable kinematic models are needed. As in the previous examples, the accuracy of the computation of frequencies is affected by the choice of the functions as well as by the kind of modal shapes. For instance, TE6 and E8 yield precise results for torsional and coupled modes (modes II and III), E2, E3 and E6 seem suitable for

² The angular frequency is $\omega = 2\pi f$ (rad/sec) whereas f is the frequency (Hz).

detecting the axial/shear mode (IV), whereas the zig-zag function is more effective for shear modes (modes IV and V).

Table 5.7 Dimensionless natural frequencies, $L/b=10$, $[0/90/0]$ beam.

	Mode I	Mode II	Mode III	Mode IV	Mode V	DOFs
TE ₂₃ (Giunta et al., 2013)	10.038	10.371	17.719	126.70	219.02	900
EBBT	11.697	13.929	-	129.52	-	198
FSDT	10.358	11.418	-	129.58	268.47	198
TE2	10.367	11.420	20.968	128.46	268.50	396
TE2 ^{zz}	10.367	10.450	20.968	128.75	221.10	462
TE3	10.113	10.637	20.968	128.78	233.05	660
TE3 ^{zz}	10.113	10.337	20.968	128.74	218.85	726
TE6	10.069	10.501	18.005	127.24	224.88	1848
TE6 ^{zz}	10.069	10.333	18.005	127.22	218.67	1914
E1-5	10.176	10.426	21.075	129.61	220.32	726
E1-5 ^{zz}	10.176	10.351	21.075	129.61	218.91	792
E2-4	10.174	10.416	21.088	127.86	220.24	1122
E2-4 ^{zz}	10.174	10.342	21.088	126.91	218.66	1188
E3-3	10.173	10.416	21.032	128.18	220.23	1254
E3-3 ^{zz}	10.173	10.340	21.031	127.20	218.66	1320
E5-2	10.188	10.491	21.475	128.07	258.00	594
E5-2 ^{zz}	10.188	10.350	21.471	128.61	218.95	660
E6-2	10.173	10.656	21.075	127.99	233.73	594
E6-2 ^{zz}	10.173	10.342	21.075	125.78	218.94	660
E7-2	10.173	10.428	21.075	126.18	258.00	858
E8-5	10.073	10.417	18.242	129.60	220.10	1386
E8-5 ^{zz}	10.073	10.342	18.241	129.22	218.68	1452

Table 5.8 Dimensionless natural frequencies, $L/b=5$, $[0/90/0]$ beam.

	Mode I	Mode II	Mode III	Mode IV	Mode V
TE_{23} (Giunta et al., 2013)	6.9252	7.5017	9.0683	55.914	58.135
EBBT	13.752	11.552	-	-	64.722
FSDT	8.0853	8.0409	-	-	64.752
TE2	8.0837	8.0451	10.502	67.238	62.857
$TE2^{zz}$	7.0131	8.0451	10.502	66.319	62.893
TE3	7.1597	7.6230	10.502	59.912	62.824
$TE3^{zz}$	6.8990	7.6230	10.502	56.467	62.540
TE8	6.9800	7.5279	9.1129	56.694	58.670
$TE8^{zz}$	6.8886	7.5279	9.1129	55.729	58.886
E1-5	6.9675	7.6956	10.536	58.245	64.591
$E1-5^{zz}$	6.8943	7.6956	10.535	57.322	64.552
E2-4	6.9653	7.6952	10.537	58.389	59.600
$E2-4^{zz}$	6.8913	7.6952	10.537	57.323	58.670
E5-2	7.0480	7.7013	10.586	58.608	62.850
$E5-2^{zz}$	6.8969	7.7013	10.585	57.361	62.621
E6-2	7.1752	7.6954	10.536	60.916	64.457
$E6-2^{zz}$	6.8973	7.6954	10.535	57.425	64.789
E8-5	6.9649	7.5601	9.2726	56.174	63.833
$E8-5^{zz}$	6.8918	7.5601	9.2726	56.036	63.955

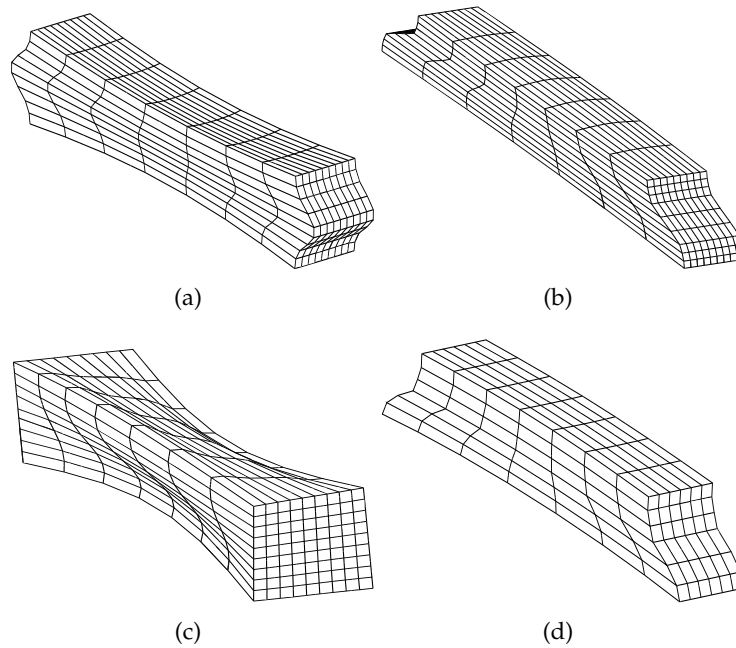


Figure 5.7 Modal shapes of laminated beams. (a) Mode IV of Tab.5.7. (b) Mode V of Tab.5.7. (c) Mode IV of Tab.5.8 and Mode V of Table 5. (d) Mode IV of Tab.5.9.

Table 5.9 Dimensionless natural frequencies, $L/b=5$, $[0/90]$ beam.

	Mode I	Mode II	Mode III	Mode IV	Mode V	DOFs
TE ₂₃ (Giunta et al., 2013)	4.9375	6.4603	9.0852	33.718	50.640	900
EBBT	6.0083	10.102	-	57.186	-	198
FSDT	5.0738	7.5051	-	40.961	-	198
TE2	5.0551	6.9637	10.133	37.566	63.570	396
TE2 ^{zz}	5.0440	6.9632	10.133	36.384	59.734	462
TE3	4.9947	6.6601	9.8334	36.165	56.963	660
TE3 ^{zz}	4.9942	6.6593	9.8330	33.851	53.001	726
TE6	4.9462	6.5042	9.1550	34.153	51.527	1848
TE6 ^{zz}	4.9384	6.5037	9.1550	33.583	50.799	1914
E1-6	5.0212	7.2227	10.235	37.565	60.877	858
E1-6 ^{zz}	4.9675	7.2227	10.235	34.202	55.170	924
E1-4 ₄	4.9406	6.5510	9.2579	34.519	52.504	1518
E1-4 ₄ ^{zz}	4.9360	6.5503	9.2582	33.564	51.480	1584
E2-4	4.9438	7.2222	10.237	33.957	54.648	1122
E2-4 ^{zz}	4.9381	7.2222	10.237	33.575	54.094	1188
E2-3 ₃	4.9407	6.6589	9.8328	33.927	53.147	1452
E2-3 ₃ ^{zz}	4.9362	6.6586	9.8328	33.590	52.615	1518
E3-4	4.9435	7.2154	10.237	33.920	54.637	1650
E3-4 ^{zz}	4.9381	7.2154	10.237	33.586	54.087	1716
E4-4	5.0065	7.2356	10.238	34.749	57.884	594
E4-4 ^{zz}	5.0059	7.2356	10.236	33.775	54.525	660
E5-3	4.9458	7.2220	10.235	34.525	55.559	858
E5-3 ^{zz}	4.9407	7.2220	10.235	33.613	54.139	924
E6-2 ^{zz}	4.9518	7.2222	10.235	33.758	54.156	660
E6-1 ₃ ^{zz}	4.9411	6.6586	9.8328	33.713	52.624	990
E8-5	6.9649	7.5601	9.2726	56.174	63.833	1386
E8-5 ^{zz}	6.8918	7.5601	9.2726	56.036	63.955	1452

Sandwich Beams

The sandwich beams considered in this section consist of structural face sheets (f) bonded to a core (c), whose material properties are:

$$E_f = 68.9GPa \quad E_c = 179.14MPa \quad G_f = 26.5GPa \quad G_c = 68.9MPa$$

$$\rho_f = 2687.3Kg/m^3, \quad \rho_c = 119.69Kg/m^3$$

The first structure has a rectangular cross-section, where the thicknesses of the face sheets and the core are $h_f = 0.40624$ and $h_c = 6.3475$ mm, respectively and the width is $b = 25.4$ mm. The length is $L = 1.2187$ m and both ends are clamped. The results of the present theories are compared with those found in (Howson and Zare, 2005) and (Banerjee et al., 2007) where the experimental values of Raville (Raville et al., 1961) were reported, and with those of a three-dimensional FEM solution (see Tab.5.10). The modal shapes considered are the first seven flexural modes on yz-plane and the first two torsional ones. For the latter, it is worth noting that expansions TE7 and E8 give best results whereas, for the flexural modes, the use of zig-zag term shows significant improvement of the related solutions, especially for TE1 and TE2.

The subsequent analysis involves a clamped-clamped sandwich beam with a lower length-to-thickness ratio ($L/h = 5$). The cross-section is square and the ratio h_c/h_f is assumed to be equal to 8. The first eight dimensionless frequencies are compared with a FEM solution, obtained using solid elements *HEX20* of *MSC NASTRAN*®. The values are presented in the following dimensionless form:

$$\bar{\omega} = \frac{L^2}{b} \sqrt{\frac{\rho_f}{G_f}} \omega$$

Given the results in Tab.5.11, it is clear that only refined kinematic models are able to describe the dynamic behaviour of this kind of structure. First of all, the improvements introduced by the zig-zag term are more evident than in the previous example. For instance, considering the natural dimensionless frequency computed with TE7, the relative error decreases from 12% to 0.05%. Further improvements concerns the VII frequency, whose related modal shape (Fig.5.8-b) involves an important deformation of the soft core of the structure. In this case, considering the expansion TE3, the error decreases approximately from 100% to 8%. For the remaining frequencies, the increase of the terms in the displacement field is more effective than the use of the zig-zag function. Mode VI (Fig.5.8-a) is an antisymmetric modal shape with respect to the yz-plane while mode VIII (Fig.5.8-c) involves again the deformation of the core. Furthermore, it must be noted that the last mode is detected only by the miscellaneous expansions (in which the order of Taylor-type polynomials is at least 4) and by E9 expansions. The latter provide appreciable results for all eight dimensionless frequencies with a low number of degrees of freedom.

5.2.2 The Functionally Graded cylinder

In this example a FGM sandwich cylinder is studied. Referring to Fig.5.9, the ratios length-to-mean radius (L/R) and mean radius-to-thickness (R/h) are assumed to be 5 and 10, respectively. The FG core is perfectly bonded to two isotropic faces, whose thicknesses are equal to $h_1 = h_3 = 0.1h$. The Young's modulus and the mass density of the core vary according to the following formula:

Table 5.10 Comparative results for the natural frequencies [Hz] of a fixed-fixed sandwich beam.

	Mode I	Mode II	Mode III	Mode IV	Mode V	Mode VI	Mode VII	Mode VIII ^a	Mode IX ^a
Exper.(Raville et al., 1961)	-	-	185.50	280.30	399.40	535.20	680.70	-	-
(Howson and Zare, 2005)	34.597	93.100	177.16	282.78	406.33	544.33	693.79	-	-
DSM (Banerjee et al., 2007)	34.342	91.385	171.69	270.36	383.27	506.88	638.39	-	-
FEM 3D	34.817	93.676	178.20	284.37	408.44	546.93	696.77	298.97	598.88
EBBT	35.435	97.668	191.44	316.41	472.62	660.22	879.53	-	-
FSDT	35.418	97.563	191.09	315.53	470.77	656.75	873.58	-	-
TE1	35.418	97.563	191.09	315.53	470.77	656.75	873.58	1137.9	2276.4
TE1 ^{zz}	34.696	93.340	177.58	283.34	407.15	545.29	695.54	1137.9	2276.2
TE2	35.628	98.146	192.24	317.45	473.70	660.93	879.34	868.71	1738.2
TE2 ^{zz}	34.895	93.853	178.50	284.72	408.97	547.56	698.15	867.86	1733.9
TE4	35.229	95.567	183.61	296.26	430.67	583.69	753.05	365.31	729.38
TE4 ^{zz}	34.958	94.016	178.79	285.15	409.54	548.28	698.98	365.10	728.80
TE7	35.043	94.518	180.35	288.72	416.26	559.41	715.75	338.73	674.84
TE7 ^{zz}	34.951	93.977	178.75	285.08	409.43	548.10	698.71	338.66	674.66
E2-5	36.580	98.428	187.31	298.96	429.71	575.72	734.49	1139.0	2276.7
E2-5 ^{zz}	36.480	97.893	185.70	295.37	423.06	564.85	718.28	1139.0	2276.7
E4-3 ₃	35.071	94.825	181.53	291.72	422.05	569.17	731.09	867.43	1733.4
E4-3 ₃ ^{zz}	34.982	93.836	178.28	284.84	409.31	547.13	701.35	867.23	1732.1
E5-2 ₂	34.984	94.369	180.10	288.38	415.81	558.89	715.30	867.36	1733.2
E5-2 ₂ ^{zz}	34.892	93.845	178.48	284.69	408.92	547.50	698.05	867.26	1732.6
E8-5	35.904	96.692	184.19	294.30	423.49	568.03	725.46	369.69	730.74
E8-5 ^{zz}	35.809	96.184	182.65	290.86	417.11	557.55	709.79	369.55	730.50

(-): expansions with zig-zag term.

^a: torsional mode.

Table 5.11 Comparative results for the dimensionless frequencies of a fixed-fixed sandwich beam with $L/b = 5$.

	Mode I ^a	Mode II ^a	Mode III ^c	Mode IV ^a	Mode V ^b	Mode VI*	Mode VII*	Mode VIII*	DOFs
FEM 3D	2.0308	4.3874	6.6198	7.3156	7.7618	10.461	10.603	10.673	68277
EBBT	14.373	35.786	-	61.872	9.4430	-	-	-	279
FSDT	10.367	22.116	-	35.737	7.9752	-	-	-	279
TE1	10.368	22.116	15.118	35.737	7.9752	30.233	88.065	-	279
TE1 ^{zz}	2.1069	4.6382	15.091	7.8576	8.8191	29.965	19.171	-	372
TE3	3.4838	7.1907	13.763	11.428	7.9197	31.614	21.320	-	930
TE3 ^{zz}	2.1030	4.6302	15.896	7.8498	7.9198	29.963	11.445	-	1023
TE6	2.2745	4.8532	7.0430	7.9833	7.8136	12.188	12.294	12.252	2604
TE6 ^{zz}	2.0325	4.3951	6.9046	7.3309	7.8136	11.402	11.032	12.252	2697
TE7	2.2687	4.8424	6.9949	7.9683	7.8120	11.847	11.971	12.234	3348
TE7 ^{zz}	2.0319	4.3923	6.8579	7.3222	7.8120	11.162	10.805	12.234	3441
E1-3 ₄	2.1753	4.6773	7.7521	7.4934	7.8533	13.142	12.132	19.943	1953
E1-3 ₄ ^{zz}	2.0386	4.4155	7.4239	7.3746	7.8533	12.710	11.330	19.943	2046
E5-3 ^{zz}	2.0434	4.4312	15.079	7.4039	8.1020	29.911	11.378	-	1302
E8-5 ^{zz}	2.1022	4.6233	7.3860	7.8253	7.8947	12.540	17.664	-	2046
E9-2 ^{zz}	2.0343	4.3993	8.6952	7.3368	8.0206	12.493	13.502	16.390	2418
E9-3 ^{zz}	2.0317	4.3914	6.9315	7.3220	7.8181	11.114	10.823	12.284	4650
E9-4 ^{zz}	2.0299	4.3850	6.7931	7.3065	7.8055	10.924	10.760	11.698	7626

(-): expansions with zig-zag term.
 - : results not provided by the model.
 *: mode in Fig.5.
^a: bending mode in z - direction.
^b: bending mode in x - direction.
^c: torsional mode.

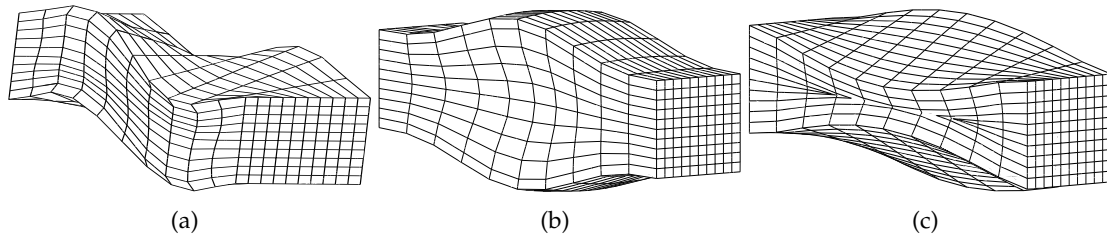


Figure 5.8 Modal shapes of sandwich beam. (a) Mode VI (b) Mode VII (c) Mode VIII.

$$f = (f_1 - f_2) \left(\frac{2|\zeta|}{h_2} \right)^\alpha + f_2 \quad (5.4)$$

where h_2 is the core thickness, ζ is the generic coordinate ($-\frac{h_2}{2} < \zeta < \frac{h_2}{2}$) and the exponent α assumes the values 3, 5 and ∞ . For this case, E_1 and E_2 are assumed to be 70 and 380 GPa, whereas the mass densities ρ_1, ρ_2 are 2702 and 3800 Kg/m³, respectively. The Poisson's ratio ν is constant and equal to 0.3. For the sake of clarity, Fig.5.9 shows how the properties E and ρ change along the thickness. The results in Tab.5.12 are reported in terms of non-dimensional frequency parameter $\bar{\omega} = \omega h \sqrt{\frac{\rho_2}{E_2}}$ and compared with those presented in (Wu and Kuo, 2013), in which a semi-analytical solution based on the finite layer method was developed for the simply-supported cylindrical structures. As expected, accuracy improves when the displacement field is enriched. The two graphs of Fig.5.10 illustrate how the percentage error $\left(\frac{\bar{\omega} - \bar{\omega}_{ref}}{\bar{\omega}_{ref}} \times 100 \right)$ varies with respect to the number of degrees of freedom (DoF). For both values of the exponent α (3 and ∞), it is possible to note that higher order models are needed to reach acceptable results for all modes of deformation and indeed, by using either the tenth-order Taylor expansion or the E9-4 series, errors remain lower than 5%.

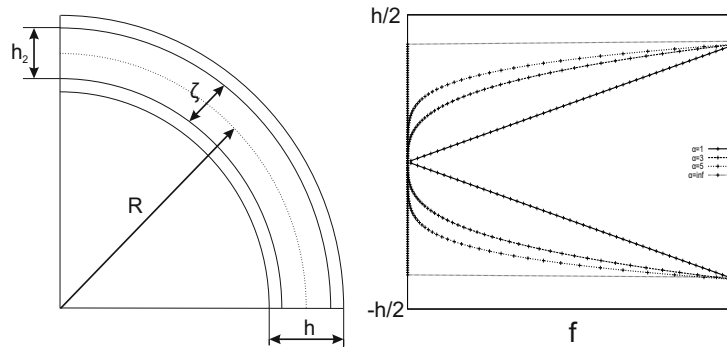


Figure 5.9 Cylinder cross-section and variations of the generic property f along the thickness.

5.2.3 Thick metallic and composite cylinders

This section presents the results obtained from free-vibration analyses carried out on moderately thick shells at standstill. Later on, the same structures will be considered in order to evaluate the effects of the rotational speed on their frequencies.

First of all, a thick isotropic cylinder has been considered. Its material properties are: Young's modulus $E = 207$ GPa, Poisson's ratio $\nu = 0.28$ and density $\rho = 7860$ kg/m³. Both ends are

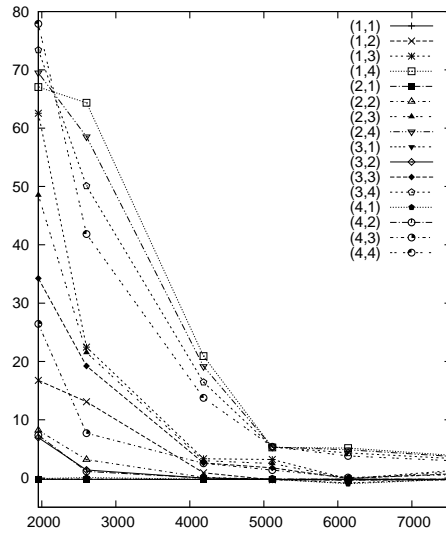
free (F-F) and the length, the mean radius and the thickness of the structure are 0.254 m, 0.09525 m and 0.0381 m, respectively. This cylinder was previously studied in (Wang et al., 1998) where its three-dimensional mode shapes were accurately classified. The accuracy of the 1D-CUF elements is evaluated, comparing the natural frequencies with those obtained using theoretical as well as experimental approaches. It is possible to observe in Tab.5.13 that both TE expansions (TE8 and TE9) yield results very close to the 3D solution for all considered modes.

Secondly, a thick cylinder made of orthotropic material is studied. The mechanical properties are: $E_{11} = 211$ GPa, $E_{22} = E_{33} = 24.1$ GPa, $G_{12} = G_{13} = G_{23} = 6.9$ GPa, $\nu_{12} = \nu_{13} = \nu_{23} = 0.36$ and $\rho = 1967$ kg/m³. The thickness-to-diameter and the length-to-diameter ratios are $\alpha = 0.1667$ and $k = 2.5$, respectively, with the mean diameter equal to 0.1 m. The considered structure is simply supported and clamped at its ends and the layers have the same thickness. The natural frequencies computed with various Taylor-like expansions, and for different lamination schemes, are listed in Tab.5.14. For the purpose of comparison, in the last column the results obtained with the DIQUMASPAB software are shown. It should be noted that the beam element TE8 provides accurate results, the maximum percentage error is approximately 7% for the radial mode $n = 3$ and lamination scheme $[0^\circ/0^\circ]$. Furthermore, it is well known that the lamination scheme strongly affects the order of appearance of the modes. For instance, when the ply angle is equal to 90° , the shell-like modes occur at higher frequencies than those relating to the bending and extensional deformations, contrary to what happens for 0° .

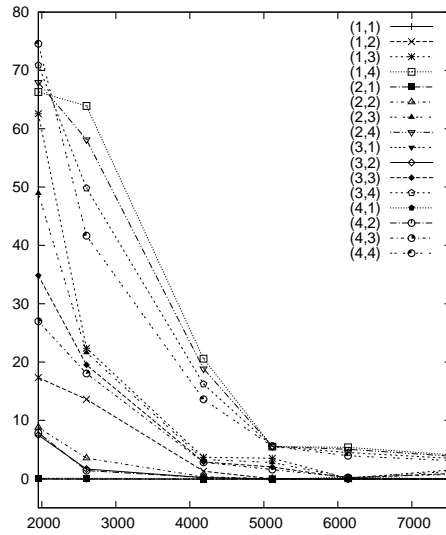
Table 5.12 Non-dimensional frequencies parameter $\bar{\omega}$ for a sandwich FGM cylinder.

α	(m,n)	TE5	TE6	TE8	TE9	TE10	E9-4	LD ₃₃ (Wu and Kuo, 2013)
3	(1,1)	0.015361	0.015361	0.015360	0.015360	0.015357	0.015360	0.015396
	(1,2)	0.012379	0.011991	0.010700	0.010572	0.010572	0.010570	0.010603
	(1,3)	0.037004	0.027878	0.023520	0.023487	0.022739	0.023055	0.022764
	(1,4)	0.069182	0.068064	0.050075	0.043592	0.043541	0.043031	0.041413
	(2,1)	0.037971	0.037967	0.037962	0.037962	0.037905	0.037962	0.038044
	(2,2)	0.024680	0.023535	0.022843	0.022764	0.022762	0.022762	0.022814
	(2,3)	0.041048	0.033589	0.028462	0.028326	0.027616	0.027917	0.027637
	(2,4)	0.075675	0.070775	0.053192	0.047022	0.046805	0.046301	0.044643
	(3,1)	0.055409	0.055400	0.055380	0.055379	0.055032	0.055380	0.055498
	(3,2)	0.040272	0.038185	0.037661	0.037585	0.037582	0.037582	0.037661
	(3,3)	0.049534	0.043988	0.037851	0.037544	0.036867	0.037163	0.036897
	(3,4)	0.088012	0.076183	0.059094	0.053461	0.052947	0.052460	0.050754
	(4,1)	0.066753	0.066750	0.066674	0.066672	0.066173	0.066672	0.066811
	(4,2)	0.055221	0.052033	0.051449	0.051352	0.051346	0.051348	0.051442
	(4,3)	0.061498	0.057241	0.049866	0.049301	0.048679	0.048912	0.048636
	(4,4)	0.106066	0.084568	0.067819	0.062819	0.061887	0.061404	0.059622
5	(1,1)	0.014674	0.014673	0.014673	0.014673	0.014672	0.014673	0.014728
	(1,2)	0.012008	0.011629	0.010369	0.010235	0.010236	0.010233	0.010286
	(1,3)	0.036057	0.027151	0.022950	0.022915	0.022153	0.022466	0.022212
	(1,4)	0.067267	0.066243	0.048739	0.042526	0.042470	0.041959	0.040374
	(2,1)	0.036278	0.036273	0.036269	0.036269	0.036271	0.036269	0.036397
	(2,2)	0.023750	0.022622	0.021939	0.021854	0.021853	0.021853	0.021938
	(2,3)	0.039935	0.032645	0.027691	0.027547	0.026820	0.027119	0.026885
	(2,4)	0.073364	0.068858	0.051761	0.045849	0.045614	0.045111	0.043497
	(3,1)	0.052961	0.052952	0.052930	0.052929	0.052798	0.052928	0.053116
	(3,2)	0.038704	0.036648	0.036124	0.036042	0.036013	0.036039	0.036172
	(3,3)	0.048072	0.042645	0.036698	0.036371	0.035691	0.035972	0.035768
	(3,4)	0.084994	0.074066	0.057468	0.052071	0.051528	0.051034	0.049390
	(4,1)	0.063862	0.063859	0.063776	0.063774	0.063708	0.063774	0.063998
	(4,2)	0.053099	0.049964	0.049370	0.049266	0.049261	0.049262	0.049433
	(4,3)	0.059573	0.055414	0.048263	0.047658	0.046905	0.047268	0.047061
	(4,4)	0.102079	0.082142	0.065901	0.061110	0.060092	0.059630	0.057938
∞	(1,1)	0.013160	0.013160	0.013159	0.013159	0.013156	0.013159	0.013170
	(1,2)	0.010916	0.010570	0.009423	0.009302	0.009301	0.009301	0.009304
	(1,3)	0.032905	0.024767	0.020979	0.020948	0.020254	0.020543	0.020239
	(1,4)	0.061290	0.060407	0.044434	0.038878	0.038829	0.038352	0.036854
	(2,1)	0.032540	0.032536	0.032532	0.032532	0.032554	0.032531	0.032555
	(2,2)	0.021441	0.020402	0.019777	0.019701	0.019701	0.019700	0.019710
	(2,3)	0.036398	0.029727	0.025240	0.025120	0.024475	0.024741	0.024440
	(2,4)	0.066673	0.062774	0.047179	0.041896	0.041694	0.041225	0.039696
	(3,1)	0.047522	0.047513	0.047494	0.047494	0.047568	0.047493	0.047526
	(3,2)	0.034903	0.033008	0.032532	0.032459	0.032459	0.032458	0.032473
	(3,3)	0.043723	0.038750	0.033355	0.033070	0.032458	0.032712	0.032423
	(3,4)	0.076978	0.067483	0.052349	0.047532	0.047063	0.046611	0.045042
	(4,1)	0.057351	0.057349	0.057277	0.057277	0.057450	0.057275	0.057310
	(4,2)	0.047908	0.045023	0.044493	0.044403	0.044401	0.044400	0.044410
	(4,3)	0.054100	0.050294	0.043797	0.043275	0.042698	0.042926	0.042609
	(4,4)	0.092171	0.074786	0.059985	0.055719	0.054865	0.054426	0.052797

 m : half-waves in y -direction. n : half-waves in circumferential direction.



(a) $\alpha = 3$



(b) $\alpha = \infty$

Figure 5.10 Percentage error versus the number of degrees of freedom.

Table 5.13 Frequencies [Hz] at standstill of the thick isotropic cylinder.

Modal description			Frequency [Hz]				
Mode Type	n	m	TE8	TE9	2D(Guo et al., 2001)	3D(Wang et al., 1998)	Exp.(Wang et al., 1998)
Pure Radial	2	0	2746	2606	2573	2594	2570
Radial Shearing	2	1	3101	2993	2950	2989	2962
Axial Bending	1	1	6233	6230	6239	6240	6286
Global Torsion	0	1	6313	6313	6320	6291	-
Radial Shearing	2	2	6484	6433	-	6503	6536
Global Bending	1	2	7038	7033	7134	7109	7104
Radial Shearing	3	1	7574	7502	-	7219	7100
Extensional	0	0	8111	8108	8096	8081	8149
Extensional	0	1	8558	8551	-	8567	8615
Extensional	0	2	8821	8815	-	8845	8886
Longitudinal	0	0	11272	11269	11266	11460	11536
Circumferential	1	1	12673	12673	12653	12647	12616

:- result not provided.

Table 5.14 Frequencies [Hz] at standstill of the C-S composite cylinder.

Mode Type	n	m	TE6	TE7	TE8	DQM*
$0^\circ/0^\circ$						
Extensional	0	0	10167.	10160.	10160. ^(0.04)	10155.
Bending	1	1	2885.8	2862.4	2862.3 ^(0.16)	2857.5
Radial	2	1	3945.9	3827.8	3781.6 ^(3.94)	3638.0
Radial	2	2	6498.8	6431.5	6272.5 ^(2.16)	6139.7
Radial	3	1	8343.4	8305.3	7978.6 ^(7.07)	7451.6
Radial	3	2	9933.8	9855.8	9589.1 ^(6.79)	8978.8
Torsion	1	0	3745.9	3745.9	3745.9 ^(0.00)	3745.9
$30^\circ/-30^\circ$						
Extensional	0	0	5863.8	5849.7	5849.4 ^(0.26)	5833.7
Bending	1	1	5227.5	5206.1	5204.3 ^(-0.42)	5226.5
Radial	2	1	4485.7	4308.1	4348.3 ^(2.84)	4227.9
Radial	2	2	8315.0	8261.9	8168.3 ^(0.51)	8126.1
Radial	3	1	8790.1	8757.7	8459.4 ^(5.93)	7985.5
Radial	3	2	10736.	10679.	10429. ^(5.10)	9922.5
Torsion	1	0	8331.1	8322.9	8316.3 ^(-0.82)	8385.8
$45^\circ/-45^\circ$						
Extensional	0	0	3637.7	3631.4	3630.3 ^(0.06)	3627.9
Bending	1	1	4458.7	4446.6	4444.3 ^(-0.05)	4446.9
Radial	2	1	4397.3	4307.9	4271.5 ^(2.71)	4158.6
Radial	2	2	7390.9	7311.1	7229.4 ^(0.70)	7178.9
Radial	3	1	9649.5	9522.0	9236.3 ^(5.03)	8793.7
Radial	3	2	11110.	10989.	10719. ^(4.98)	10210.
Torsion	1	0	9725.8	9710.4	9706.9 ^(-0.66)	9771.4
$90^\circ/90^\circ$						
Extensional	0	0	3522.9	3520.9	3520.8 ^(0.54)	3501.8
Bending	1	1	2309.3	2302.4	2302.3 ^(0.17)	2298.2
Radial	2	1	6344.7	5998.0	5986.4 ^(3.65)	5775.2
Radial	2	2	7198.1	6909.6	6851.2 ^(2.46)	6686.3
Radial	3	1	14641.	14620.	12836. ^(6.20)	12086.
Radial	3	2	15043.	14918.	13213. ^(6.17)	12444.
Torsion	1	0	3745.9	3745.9	3745.9 ^(0.00)	3745.9
$0^\circ/90^\circ/0^\circ$						
Extensional	0	0	8735.9	8733.6	8731.0 ^(0.00)	8731.7
Bending	1	1	2869.0	2845.3	2845.2 ^(0.20)	2839.4
Radial	2	1	4135.6	4044.6	3998.8 ^(4.02)	3843.9
Radial	2	2	6597.1	6543.0	6384.8 ^(2.31)	6240.5
Radial	3	1	8989.6	8951.6	8621.3 ^(6.83)	8069.7
Radial	3	2	10465.	10382.	10104. ^(6.75)	9465.0
Torsion	1	0	3745.9	3745.9	3745.9 ^(0.00)	3745.9

*: first-order shear deformation shell theory.

In brackets, the relative errors: $(100*(DQM-TE8))/DQM$.

5.3 The spinning structures

5.3.1 Classical beam theories

In order to assess the theory presented in Sec.3.2, shafts made of isotropic material are here considered. The boundary conditions and the ratio between the cross-section dimensions are assumed to be problem's parameters. Ten finite elements are used for the discretization along the $y - axis$. With the purpose of enabling a general application of results, they are presented in non-dimensional form by adopting the following non-dimensional natural frequency and spinning speed parameters:

$$\omega^* = \frac{\omega}{\omega_0}, \quad \Omega^* = \frac{\Omega}{\omega_0}, \quad \omega_0 = \sqrt{\frac{\sqrt{EJ_{xx}EJ_{yy}}}{\rho AL^4}},$$

where J_{xx}, J_{zz} are the moments of inertia in the two principal planes, E is the Young's Modulus, A the area of the cross-section and L the length of the beam. In the first example, the dynamic behavior of a beam with $J_{xx} = J_{zz}$ which is subjected to different boundaries conditions is investigated. Equation (5.5) is exploited for comparison purposes and the relative results are reported in Fig.5.11.

$$\omega_{ref} = \lambda^2 \sqrt{\frac{EI}{\rho AL^4}} \mp \Omega \quad (5.5)$$

λ is a coefficient depending on the boundary conditions.

As easily shown, the results derived by the Unified Formulation match those of the analytical solutions for every type of boundary condition. Since the effects of shear deformation and rotatory inertia are considered to be small for this type of rotor, the study has been conducted using Euler-Bernoulli theory. In Tab.5.15, some values of non-dimensional natural frequency at different spinning speed parameters are compared with those obtained by Banerjee *et al* in (Banerjee and Su, 2004) for the cantilever beam. It should be noted that the frequencies are very close to those of the reference, especially the value of the critical speeds.

Table 5.15 Frequency ratios of a cantilever spinning beam with $J_{xx} = J_{zz}$.

Ω^*	Theory	ω_1^*	ω_2^*	ω_3^*	ω_4^*	ω_5^*	ω_6^*
0	(Banerjee and Su, 2004)	3.516	3.516	22.034	22.034	61.697	61.967
	Present	3.510	3.510	21.992	21.992	61.551	61.551
2	(Banerjee and Su, 2004)	1.516	5.516	20.034	24.034	59.697	63.697
	Present	1.510	5.510	19.995	23.992	59.559	63.552
3.51	(Banerjee and Su, 2004)	0	7.016	18.534	25.534	58.197	65.197
	Present	0	7.020	18.486	25.500	58.052	65.059
4	(Banerjee and Su, 2004)	-	7.516	18.034	26.034	57.697	65.697
	Present		7.509	17.996	25.990	57.563	65.548

In the same work, Banerjee *et al.* presented the results related to beams with rectangular cross-sections. Figure 5.12 shows how the first two flexural natural frequencies are affected by the

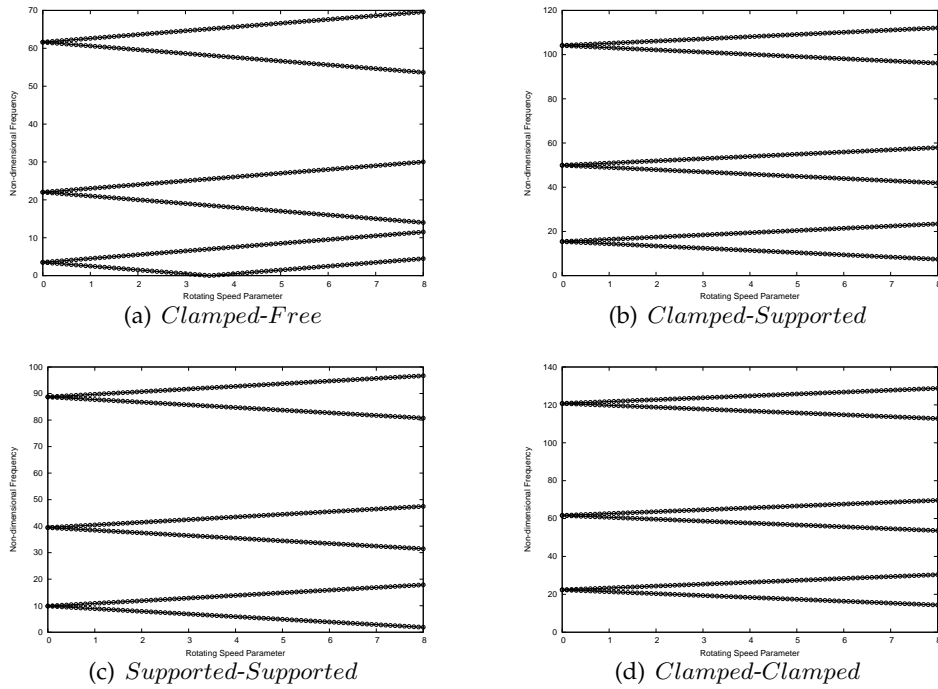


Figure 5.11 The variation of non-dimensional natural frequencies with spinning speed parameter for a beam (J_{xx} , J_{zz}) subjected to several boundary conditions ('lines': Eq.5.5; '⊙': CUF).

ratio between the main cross-section dimensions, b/h , when the rotating speed is changing. The reference solutions are obtained using Eq.5.6, where $\tilde{\omega}_x$ and $\tilde{\omega}_z$ are the natural frequencies at standstill.

$$\omega_{x,z} = \sqrt{\frac{1}{2} \{ -(\tilde{\omega}_x^2 + \tilde{\omega}_z^2 + 2\Omega^2) \pm \sqrt{(\tilde{\omega}_x^2 - \tilde{\omega}_z^2)^2 + 8\Omega^2(\tilde{\omega}_x^2 + \tilde{\omega}_z^2)} \}} \quad (5.6)$$

It is clear that the behaviors of the frequencies in the two principal planes are very different. In fact, the first frequency decreases until it becomes zero, whereas the second continues to increase. It is important to note that, for these values of *aspect - ratio*, the flexural normal modes in the two planes are alternated. On the contrary, when the width becomes much smaller than the height, the relationship for the frequency ratios undergoes an observable change. For instance, if $b = 0.1h$, the first two mode frequency ratios in the x direction are smaller than the first one in z direction. This difference is shown in Fig. 5.13, where the first seven frequency ratios are presented. For the last case, in Tab.5.16 the results obtained with CUF are compared with the numerical values of frequency ratios presented in ((Banerjee and Su, 2004)).

As the effects of shear deformation can be disregarded when the shaft is very thin, but if this approximation is no longer valid, other structural models are needed. In the following test case, a moderate thick cylindrical beam simply supported is analyzed. The length and the radius are assumed to be equal to 10 m and 0.25 m, respectively. The material has the Young's modulus equal to 210 GPa whereas the Poisson coefficient and the density are 0.3 and 7800kg/m³. The results in Tab.5.17 are compared with those provided by Curti *et al.* (Curti *et al.*, 1992), who proposed an analytical procedure based on DSM including the effects of the shear deformation of the shaft. It is evident that, also in this case, the proposed results strongly agree with the reference solutions.

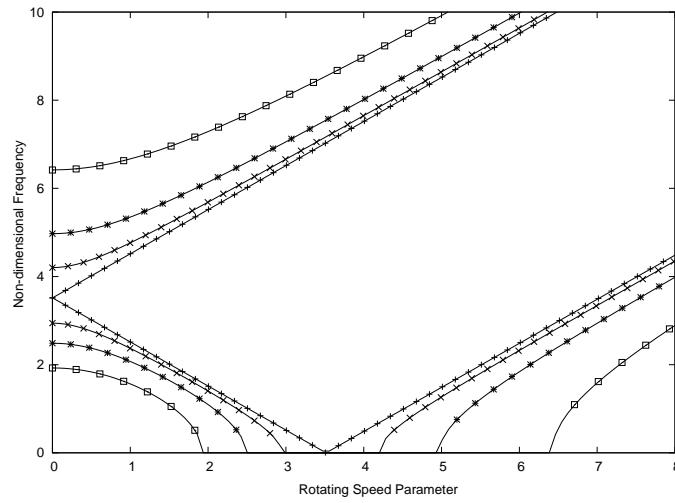


Figure 5.12 The first two frequency ratios w_1^* and w_2^* as functions of the spinning speed ratio for various values of aspect - ratio (‘-’: Eq.5.6; ‘+’: $b/h = 1$; ‘×’: $b/h = 0.7$; ‘*’: $b/h = 0.5$; ‘□’: $b/h = 0.3$).

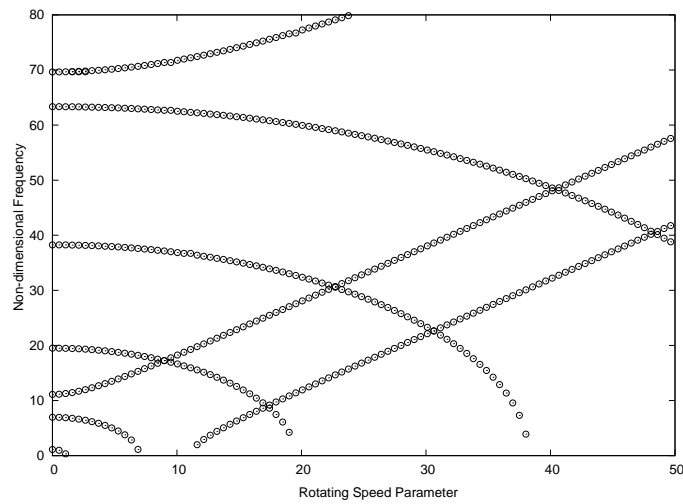


Figure 5.13 The first seven frequency ratios $w_1^* - w_7^*$ as functions of the spinning speed ratio for aspect-ratio equal to 0.1.

Table 5.16 Frequency ratios of a cantilever spinning beam with rectangular cross-section ($b = 0.1h$).

Ω^*	<i>Theory</i>	ω_1^*	ω_2^*	ω_3^*	ω_4^*
0	(Banerjee and Su, 2004)	1.1119	6.9680	11.119	19.511
	Present	1.1114	6.9658	11.119	19.508
1.11	(Banerjee and Su, 2004)	0	6.8623	11.307	19.473
	Present	0	6.8732	11.284	19.475
2	(Banerjee and Su, 2004)	0	6.6637	11.632	19.404
	Present	0	6.6611	11.633	19.401
4	(Banerjee and Su, 2004)	-	5.6679	12.900	19.080
	Present	-	5.6638	12.901	19.077
6	(Banerjee and Su, 2004)	-	3.4910	14.536	18.530
	Present	-	3.4818	14.538	18.526
7.1	(Banerjee and Su, 2004)	-	0	15.526	18.118
	Present	-	0	15.524	18.116
8	(Banerjee and Su, 2004)	-	-	16.3367	17.7348
	Present	-	-	16.3399	17.7310

Table 5.17 Forward critical speeds predicted by CUF for the test case of a simply supported shaft.

Mode Number	(Curti et al., 1992)	<i>EBBM</i>	<i>FSDT</i>
1	63.869	63.699	63.550
2	253.769	255.001	252.449
3	564.741	573.379	564.299
4	989.050	1019.405	988.400
5	1516.866	1599.400	1519.259

EBBM stands for Euler-Bernoulli Beam Model.

FSDT stands for First-order Shear Deformation Theory.

5.3.2 Higher order beam theories for spinning composite shafts

Cylindrical composite shaft

This section shows the results related to analyses carried out on composite thin-walled structures. The first case concerns the dynamic study of hollow rotating cylinders whose material and geometrical features are summarised in Tab.5.18. The shaft has been discretised with seven 4-nodes beam elements and it is supported by one bearing at each end, whose stiffnesses k_{xx} and k_{zz} are 1740 GN/m. The first critical speeds obtained with 1D-CUF theories are shown in Tab.5.19 and compared with those found in (Chang et al., 2004), adopting the $[90^\circ/45^\circ/-45^\circ/0^\circ_6/90^\circ]$ lamination scheme. The results for both materials are within the interval of reference speeds, and the differences between the three theories (TE2, TE3 and TE4) are essentially negligible. Furthermore, the effects of the aspect ratio for the graphite-epoxy shaft are also investigated. As expected, when the structure becomes thicker, the critical speeds occur at higher values, and the differences between the three expansions increase. In fact, when the aspect ratio is equal to 2, TE3 and TE4 lead to similar results, whereas TE2 overestimates the critical speed of 10%. In addition, considering the same material, the effects due to the lamination scheme have been evaluated and the results are shown in Tab.5.21. The increasing the lamination angle with respect to the longitudinal direction reduces the shaft stiffness and causes a consequent reduction in the critical speeds. Some evident discrepancies can be observed between the refined beam models and those found in literature. In fact, when θ is equal to 15° , 30° or 45° , the present results are closer to speeds obtained with the shell theory SST than those of classical beam models. In order to show the accuracy of the CUF elements, natural frequencies of the boron-epoxy shaft (Tab.5.18), computed with TE elements, are listed in Tab.5.22 and compared with the results found in (Boukhalifa, 2011), where a first-order shear beam theory with a torsion function was proposed, and with those obtained using Di.Qu.M.A.S.P.A.B., a free software based on the Differential Quadrature Method (GDQ) for shells and plates. At least the third-order theory (TE3) is necessary to obtain accurate results for bending as well as torsional modes. Moreover, it is worth noting that remarkable differences exist between the first natural frequencies of (Boukhalifa, 2011) and those obtained with the other approaches, especially for θ equal to 15° , 30° , 45° and 60° . The use of a constant shear correction factor could be the reason for these important discrepancies, since the shear effects are closely related to the lamination scheme.

Thin-walled composite shaft

In the following numerical illustrations, box beams with thin walls, whose dimensions are shown in Tab.5.18, are studied. The results are displayed for different cross-section height-to-width ratios ($R = b/c$, Fig.5.14) and lamination angles (θ), in terms of non-dimensional frequency ($\bar{f} = f/f_n$), as a function of the speed parameter ($\bar{\Omega} = \Omega/f_n$). The value f_n is the natural frequency of a cantilever graphite-epoxy box beam with $R = 1$ and $\theta = 90^\circ$ obtained with a 2D finite element solution ($f_n = 52.649$ [Hz]). Figure 5.15 shows how the first two frequency ratios vary with the rotational speed for θ equal to 0° and 90° , using various expansions. As expected, the theory order does not affect the trend of the branches, with the exception that curves start at lower values when the displacement field is enriched, and these differences are more evident for the case in which θ is equal to 0° . This fact demonstrates that classical models (and ad-hoc theories!) cannot guarantee the same accuracy for all lamination angles, thus confirming that a simple method to conceive increasingly accurate theories could be a very useful

Table 5.18 Material and geometrical features of composite shaft.

Dimensions	Cylinders	Box beam
Thickness (h) [m]	0.001321	0.01016
Width (c) [m]	0.1269*	0.1016
Length (L) [m]	2.470	1.016
Materials	Boron-epoxy (Chang et al., 2004)	Graphite-epoxy(Chang et al., 2004)
E_{11} [Gpa]	211.0	139.0
E_{22} [Gpa]	24.1	11.0
G_{23} [Gpa]	6.90	3.78
G_{31} [Gpa]	6.90	6.05
G_{12} [Gpa]	6.90	6.05
ρ [kg/m ³]	1967.0	1578.0
ν_{12}	0.360	0.313

*: mean diameter.

Table 5.19 Critical speeds (rpm) of composite shafts for [90°/45°/-45°/0°_o/90°].

Theory	Boron-epoxy	Graphite-epoxy
SST (Chang et al., 2004)	5872	5349
EBBT (Chang et al., 2004)	5919	5302
BTBT (Chang et al., 2004)	5788	5113
FSDT (Chang et al., 2004)	5762	5197
TE2	5808	5256
TE3	5766	5232
TE4	5724	5220

SST: Sanders shell theory.

EBBT: Euler-Bernoulli beam theory.

BTBT: Bresse-Timoshenko beam theory.

FSDT: First-order shear deformation theory.

tool. Moreover, in order to evaluate the effect due to the ply angle, the first two frequency ratios are shown in Fig.5.16, adopting the TE2 and TE6 expansions. Critical speeds occur at different values, depending on the lamination angle, and maximum and minimum velocities occur for $\theta = 0^\circ$ and $\theta = 90^\circ$, respectively. Similar results were obtained by Librescu *et al.* in (Song and Librescu, 1997a). In addition, it must be noted that different lamination schemes determine the occurrence of couplings between different deformation modes. For instance, in Fig.5.14, two different configurations [$\theta_T/\theta_L/\theta_B/\theta_R$] are studied: *Case I* [45°/-45°/-45°/45°] and *Case II* [45°/-45°/45°/-45°]. The frequencies (f) and damping (D) ratios are computed as functions of the rotating speed using a number of displacement models (Fig.5.17 and Fig.5.18). Classical theories (EBBT and FSDT, Fig.5.17-a) provide qualitatively similar results for the first configuration, but do not predict any instability range. Nevertheless, with the first-order shear deformation theory, a veering of the fourth, fifth and sixth branches can be detected. TE3 and TE6 expansions, instead, correspond to dramatic changes with three instability fields appear-

Table 5.20 Critical speeds (rpm) of graphite-epoxy shaft for several length-to-diameter ratios.

Theory	L/D		
	2	5	15
SST (Chang et al., 2004)	112400	41680	8585
EBBT (Chang et al., 2004)	329600	76820	9072
BTBT (Chang et al., 2004)	176300	54830	8543
FSDT (Chang et al., 2004)	176300	55706	8527
TE2	240900	65580	8760
TE3	206400	61200	8580
TE4	206400	61200	8580

Table 5.21 Critical speeds (rpm) of composite shaft for various lamination angles.

Theory	Lamination						
	0°	15°	30°	45°	60°	75°	90°
SST (Chang et al., 2004)	5527	4365	3308	2386	2120	2020	1997
EBBT (Chang et al., 2004)	6425	5393	4269	3171	2292	1885	1813
FSDT (Chang et al., 2004)	6072	5331	4206	3124	2284	1890	1816
TE1	6270	4770	3120	2280	1950	1860	1860
TE2	6270	4710	3120	2280	1950	1860	1860
TE3	6060	4170	2760	2160	1935	1860	1830
TE4	6060	4140	2730	2145	1920	1830	1800

ing within the considered speed interval. This configuration involves a dominant twist-motion therefore models that are able to describe bending-torsional coupling are needed. In addition, when the expansion order is increased, instability thresholds are predicted at lower speed values. On the contrary, for the second case, the most important effect is due to shear and, for this reason, the shearable beam model leads to comparable results with those obtained with higher-order theories. For both schemes, the gyroscopic coupling markedly affects the system, causing several veerings of frequency branches.

In the last illustrative example, a rectangular box beam ($R = 0.5$) is analysed with the purpose of considering another kind of anisotropy. Hereafter, the reference frequency f_n is equal to 25.976[Hz]. Figure 5.19-a shows the first two frequency ratios varying with the speed parameter when θ is 0° or 15° . We compare four different theories and, for both cases, the curves move towards lower and lower values when the displacement model is enriched. For $\theta = 0^\circ$ (thin lines), TE3 branches almost overlap TE6 theory branches, while, discrepancies between these models clearly increase when θ is equal to 15° (bold lines). Therefore, in order to ensure a good accuracy for other lamination schemes, the TE6 expansion is selected and the results are shown in Fig.5.19-b. It is worth noting that the curves follow similar paths regardless of the lamination. In fact, after a veering of the backward frequency branch, two eigenvalues interact and instability occurs. Furthermore, when θ increases, the instability threshold appears at lower and lower speeds, while the range of the instability field becomes smaller, ultimately reaching

Table 5.22 Frequencies at standstill of boron-epoxy shaft.

Lam.	Mode	(Boukhalifa, 2011)	GDQ	TE4	TE3	TE2	TE1*	FSDT*	EBBT*
0°	1° Flex.	108.23	109.23	109.24	109.24	113.95	113.95	113.95	119.44
	2° Flex.	-	357.13	357.15	357.19	403.38	403.37	403.37	475.41
	1° Tors.	-	379.13	379.14	379.14	379.14	379.14	-	-
15°	1° Flex.	94.86	69.57	69.83	70.05	81.73	81.76	81.76	108.39
	2° Flex.	-	261.23	262.15	262.81	309.33	309.47	309.47	431.46
	1° Tors.	-	412.23	412.79	412.79	413.60	412.60	-	-
30°	1° Flex.	76.71	45.82	46.05	46.60	52.41	52.33	52.33	74.39
	2° Flex.	-	180.30	181.11	183.10	205.85	205.16	205.16	296.12
	1° Tors.	-	519.80	519.98	519.98	520.63	519.80	-	-
45°	1° Flex.	59.21	37.85	37.98	38.48	39.57	39.54	39.54	43.62
	2° Flex.	-	150.13	150.55	152.51	156.95	156.30	156.30	173.62
	1° Tors.	-	638.00	639.43	639.44	691.04	663.24	-	-
60°	1° Flex.	45.84	36.49	36.59	36.74	36.75	36.75	36.75	36.89
	2° Flex.	-	144.11	144.30	145.10	145.35	145.14	145.14	146.84
	1° Tors.	-	534.03	540.09	540.10	675.61	586.18	-	-
75°	1° Flex.	40.74	38.33	38.46	38.58	38.99	39.00	39.00	39.58
	2° Flex.	-	149.60	149.75	150.42	153.16	153.21	153.21	157.54
	1° Tors.	-	415.73	419.76	419.71	460.93	429.83	-	-
90°	1° Flex.	40.10	39.80	39.95	40.47	40.70	40.79	40.79	41.03
	2° Flex.	-	154.05	154.18	156.07	159.34	159.71	159.71	163.33
	1° Tors.	-	379.14	379.14	379.14	379.14	379.14	-	-

*: Poisson locking correction activated.

a minimum for $\theta = 90^\circ$. The effects of ply angles on damping are shown in Fig.5.19-c.

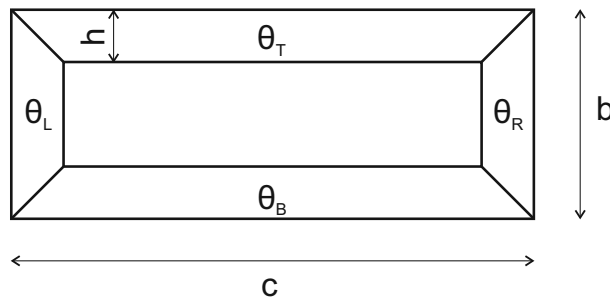


Figure 5.14 Sketch of the box beam.

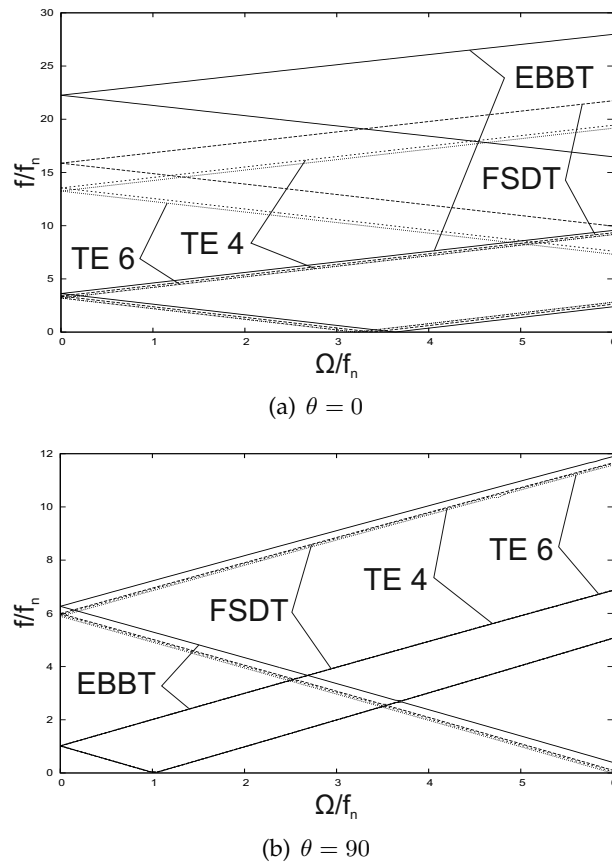


Figure 5.15 Dependency of frequency ratios upon the speed parameter for the cantilever box beam ($R = 1$).

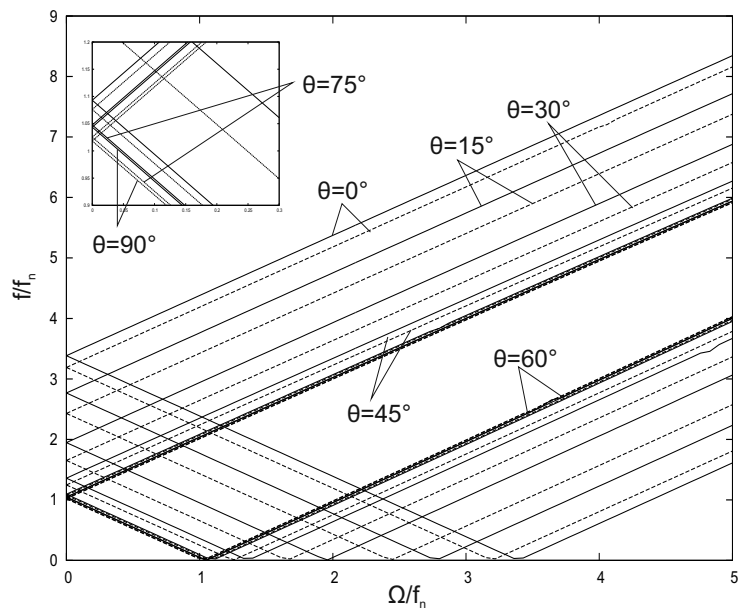
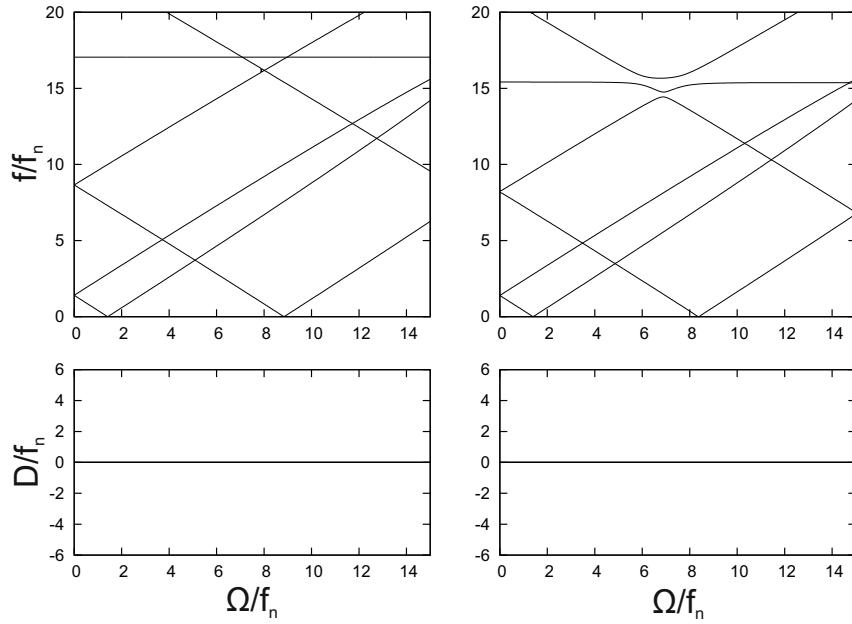
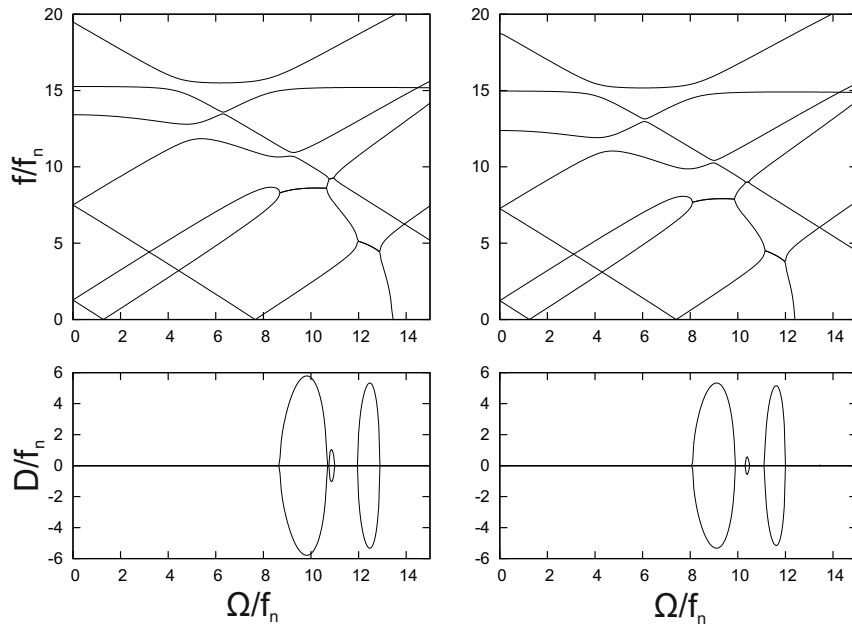


Figure 5.16 Dependency of frequency ratio upon the speed parameter for various values of ply angles ($R = 1$), '—': TE2, '- - -': TE6.

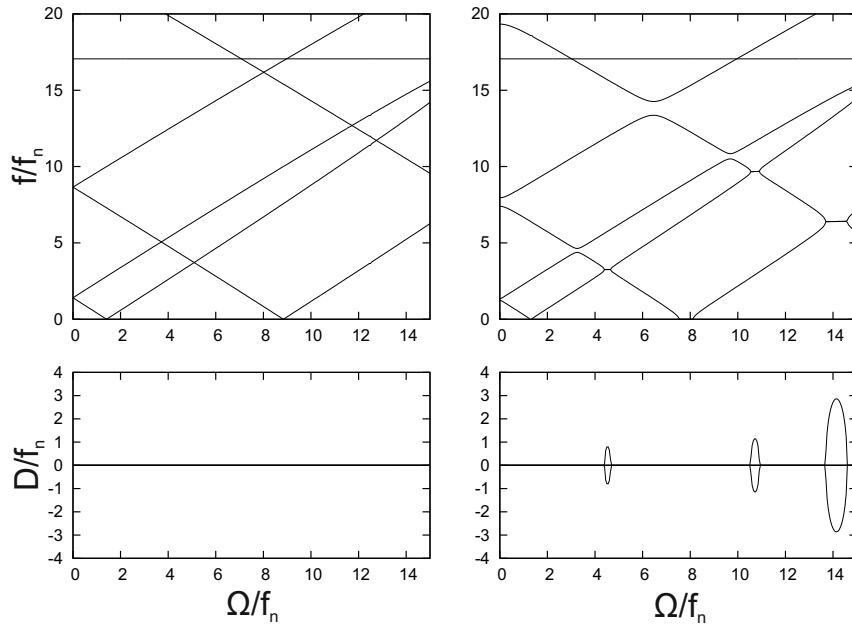


(a) EBBT, FSDT

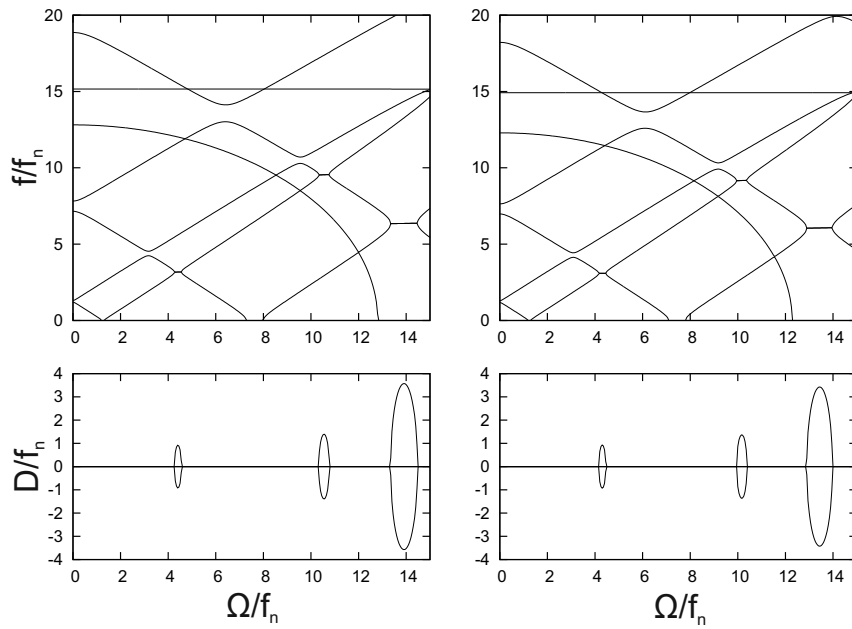


(b) TE3, TE6

Figure 5.17 Dependency of frequency ratio and damping upon the speed parameter for a cantilever box beam ($R = 1$ and Case I).

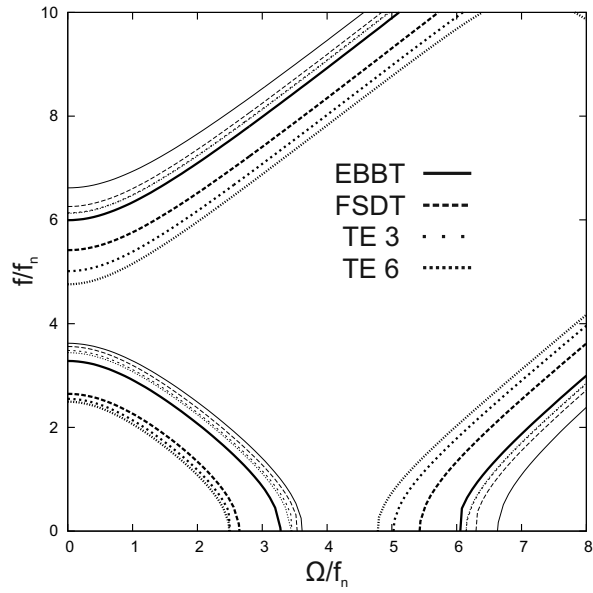


(a) EBBT, FSDT

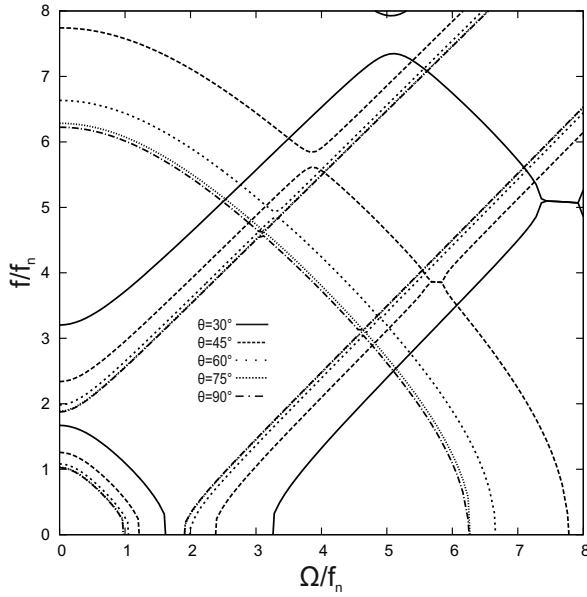


(b) TE3, TE6

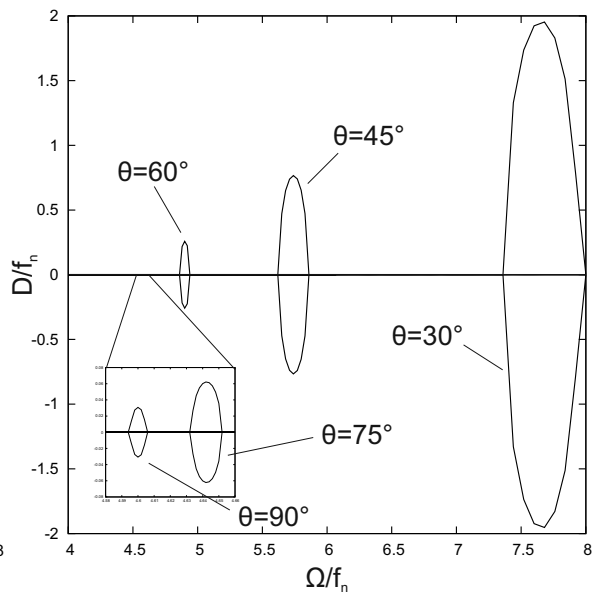
Figure 5.18 Dependency of frequency and damping ratios upon the speed parameter for a cantilever box beam ($R = 1$ and Case II).



(a) 'lines': $\theta=0^\circ$, 'bold lines': $\theta=15^\circ$



(b) Frequency ratios: TE6



(c) Damping ratios: TE6

Figure 5.19 Dependency of frequency and damping ratios upon the speed parameter for a cantilever box beam ($R = 0.5$).

5.3.3 Highly deformable spinning structures

Thin walled cylinders

The following analyses are devoted to the study of the influence of centrifugal stiffness on the dynamic behaviour of thin rotating shells (see Sec.3.2.2). To this end, isotropic and composite cylinders with different dimension ratios, boundary conditions and lamination schemes have been studied.

In the first numerical computation, a cylinder with thickness-to-diameter ratio $\alpha = 0.02$ and length-to-diameter ratio $k = 5$. The material is isotropic with Young's modulus (E), Poisson's ratio (ν) and density equal to 207.0 GPa, 0.3 and 7860 Kg/m³, respectively. Table 5.23 shows the frequencies at standstill for different dimension ratios (α = thickness/diameter and k =length/diameter with diameter equal to 1) obtained with Taylor-like expansions of fourth (TE4), fifth (TE5), sixth (TE6) and seventh (TE7) order. For comparison purposes, the last column shows the frequencies obtained using the DiQuMASPAB code. As expected, increasing the order of the theory, results converge to reference values for all considered circumferential wave numbers (n) and boundary conditions.

Table 5.23 Frequencies [Hz] at standstill of the isotropic cylinder for various α and k .

n	TE4	TE5	TE6	TE7	DQM
Supported-Supported, $\alpha = 0.02$ and $k = 5$					
1	101.2	101.2	101.2	101.2	101.2
2	96.29	76.25	75.57	64.61	64.61
3	289.4	252.1	189.0	188.1	152.2
Clamped-Clamped, $\alpha = 0.02$ and $k = 5$					
1	171.4	171.4	171.4	171.4	170.8
2	115.5	99.35	98.63	90.48	90.17
3	300.7	254.5	192.3	191.2	155.9
Clamped-Clamped, $\alpha = 0.005$ and $k = 5$					
2	75.37	73.90	73.84	73.18	72.73
3	178.3	72.94	59.86	59.63	52.50
4	-	215.8	122.6	92.91	75.54
Clamped-Clamped, $\alpha = 0.005$ and $k = 3$					
2	168.4	167.5	167.4	167.1	166.6
3	319.1	112.0	104.0	103.6	99.26
4	-	340.9	134.1	107.7	92.38

For the supported-supported condition and n equal to 2 ($\alpha = 0.02$ and $k = 5$), Fig.5.20 shows how the frequency ratio (f/f_n) changes with respect to the speed parameter (Ω/f_n) using the TE4, TE6 and TE7 expansions. In spite of the natural frequencies in the non-rotating state are different, it is interesting to note that the three displacement theories predict same variations of backward and forward non-dimensional frequencies.

To evaluate the effects of boundary conditions, cylinders with supported-supported and clamped-clamped ends are considered. The dimensionless frequencies obtained with the TE7 theory are

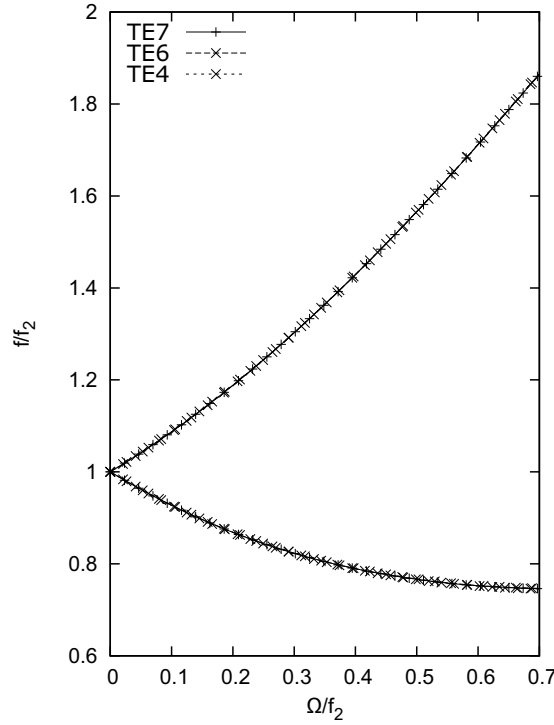


Figure 5.20 Dependency of frequency ratio upon the speed parameter for various TE expansions; '· · ·': TE4, '- -': TE6, '—': TE7 ($n = 2$, $\alpha = 0.02$ and $k = 5$).

shown in Fig.5.21-a and Fig.5.21-b, respectively.

Also in this case the non-dimensional results are nearly identical despite the different frequencies in the non-rotating state (see Tab.5.23). The graphs also show the frequency parameters derived from the following analytical solutions

$$\frac{f}{f_n} = \frac{2n}{n^2 + 1}(\Omega/f_n) \pm \sqrt{1 + \frac{n^6 - 2n^4 - 1}{(n^2 + 1)^2}(\Omega/f_n)^2} \quad (5.7)$$

$$\frac{f}{f_n} = \frac{2n}{n^2 + 1}(\Omega/f_n) \pm \sqrt{1 + \frac{n^2(n^2 - 1)^2}{(n^2 + 1)^2}(\Omega/f_n)^2} \quad (5.8)$$

$$\frac{f}{f_n} = \frac{2n}{n^2 + 1}(\Omega/f_n) \pm \sqrt{1 + \frac{n^6 + 3n^2}{(n^2 + 1)^2}(\Omega/f_n)^2} \quad (5.9)$$

In particular, Eqs.5.7 and 5.8 were proposed by Endo *et al.* in (Endo et al., 1984) for the study of rotating rings. Although the solutions were based on a non-linear shell theory, the expressions present slight differences due to the use of different hypothesis in defining acceleration and strain terms. On the other hand, using the linear approximation, Chen et al. (1993) presented Eq.5.9 for the study of high speed rotating shells. Other reference values (●) are taken from (Endo et al., 1984), where the results presented in (Srinivasan and Lauterbach, 1971) were reported in the dimensionless form. It should be observed that the TE7 results strongly agree with those obtained using Eq.5.8.

Assuming α equal to 0.005, the minimum frequency for the non-rotating cylinder occurs for $n = 3$ (see Tab.5.23). Figure 5.22-a is the result for this mode.

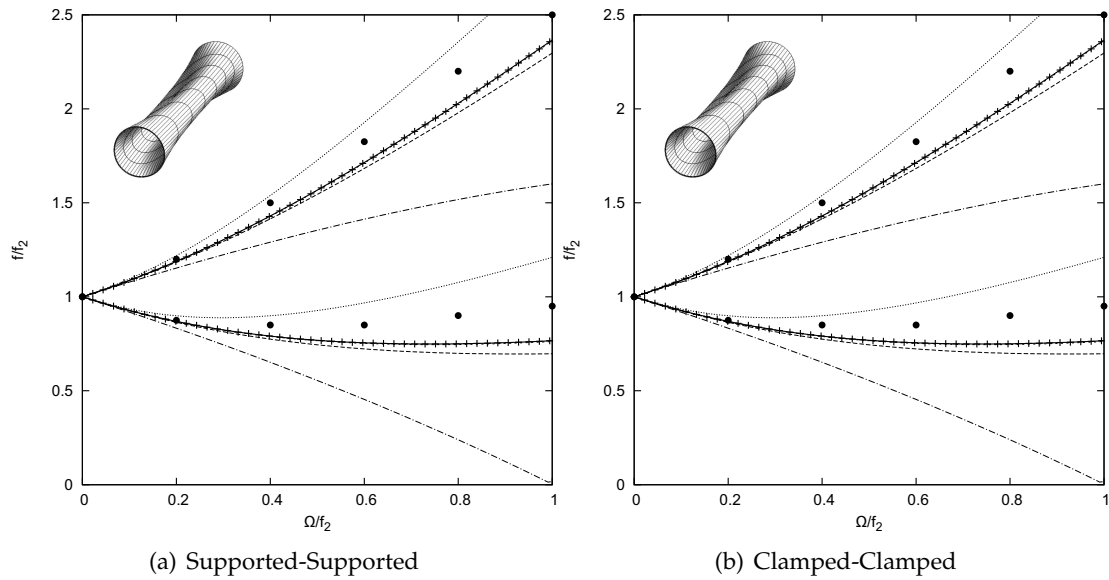


Figure 5.21 Dependency of frequency ratio upon the speed parameter; '—': 5.7, '---': 5.8, '- · -': 5.9, '●': Ref.[7] of (Endo et al., 1984), '· · ·': TE7 w/o σ_0 , '+ + +': TE7 ($n = 2$, $\alpha = 0.02$ and $k = 5$).

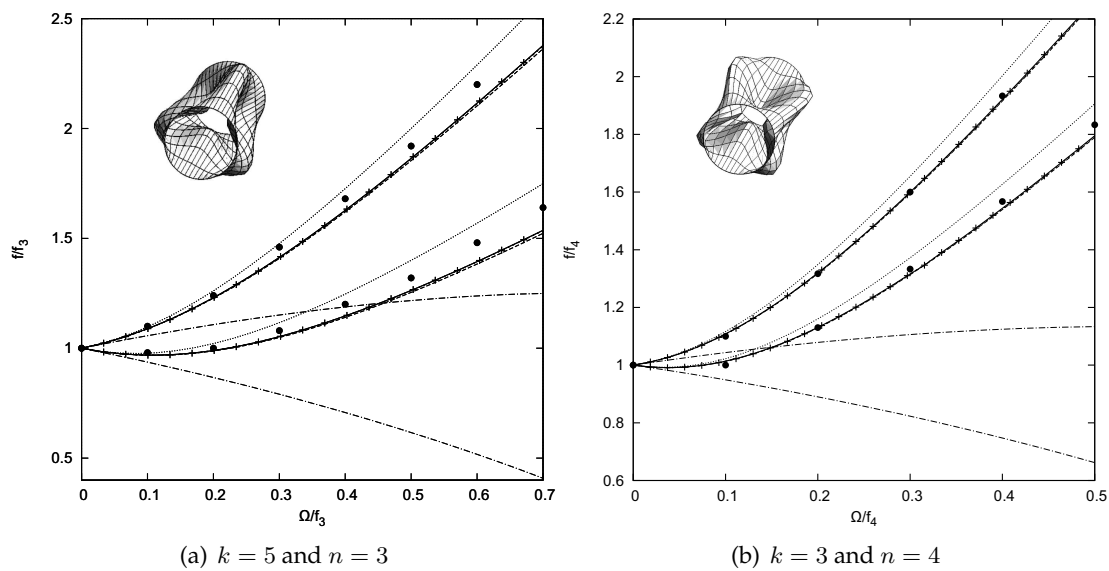


Figure 5.22 Dependency of frequency ratio upon the speed parameter; '—': 5.7, '---': 5.8, '- · -': 5.9, '●': Ref.[7] of (Endo et al., 1984), '· · ·': TE7 w/o σ_0 , '+ + +': TE7 ($\alpha = 0.005$).

Beam results agree with shell solutions, especially with those of Eqs.5.7 and 5.8. The same consideration can be made for the mode with $n = 4$ ($\alpha = 0.005$ and $k = 3$), whose frequency variations with respect to the rotational speed are shown in Fig.5.22-b. Table 5.24 lists dimensionless frequencies for five rotational speeds with or without the geometrical stiffening. It should be observed that the contribution due to the hoop tension becomes more evident as the circumferential wave number increases.

		Ω/f_n					
		0.0	0.1	0.2	0.3	0.4	0.5
Forward							
f/f_2	with σ_0	1.0	0.93	0.87	0.82	0.79	0.77
	w/o σ_0	1.0 ^(0.0)	0.92 ^(1.1)	0.83 ^(4.6)	0.74 ^(9.8)	0.65 ^(17.7)	0.55 ^(28.6)
f/f_3	with σ_0	1.0	0.97	0.99	1.05	1.15	1.26
	w/o σ_0	1.0 ^(0.0)	0.94 ^(3.1)	0.87 ^(12.1)	0.79 ^(24.8)	0.71 ^(38.3)	0.62 ^(50.8)
f/f_4	with σ_0	1.0	1.01	1.13	1.32	1.54	1.79
	w/o σ_0	1.0 ^(0.0)	0.95 ^(5.9)	0.89 ^(21.2)	0.82 ^(37.9)	0.75 ^(51.3)	0.66 ^(63.1)
Backward							
f/f_2	with σ_0	1.0	1.09	1.19	1.30	1.43	1.57
	w/o σ_0	1.0 ^(0.0)	1.08 ^(0.9)	1.15 ^(3.4)	1.22 ^(6.2)	1.29 ^(9.8)	1.35 ^(14.0)
f/f_3	with σ_0	1.0	1.09	1.23	1.41	1.63	1.86
	w/o σ_0	1.0 ^(0.0)	1.06 ^(2.8)	1.11 ^(9.8)	1.15 ^(18.4)	1.19 ^(27.0)	1.22 ^(34.4)
f/f_4	with σ_0	1.0	1.11	1.32	1.60	1.92	2.26
	w/o σ_0	1.0 ^(0.0)	1.04 ^(6.3)	1.08 ^(18.2)	1.11 ^(30.6)	1.12 ^(41.7)	1.13 ^(50.0)

In brackets, relative errors between the two cases.

Table 5.24 Dimensionless frequencies f/f_n vs. dimensionless speed Ω/f_n with and without the hoop tension for thin cylinders.

Other results are presented in Fig.5.23, where the frequencies of a rotating cantilevered cylinder ($\alpha = 0.02$ and $k = 0.5$) are shown. In the graph, the branches are related to the modes with $n = 3$ and $n = 2$. The reference solution was taken from (Guo et al., 2002), where a finite element based on a non-linear plant-shell theory was developed. Although there are some slight discrepancies, trends of curves obtained with TE7 expansion are similar to the reference. It is worth noting that the present beam element provides very accurate results for $\Omega=0$.

Moderately thick cylinder

Regarding the isotropic cylinder studied in Sec.5.2.3, the evolutions of a number of frequencies listed in Tab.5.13 as functions of the rotating speed are investigated. Figure 5.24 illustrates how frequency parameters change with the rotational speed for global bending ($n = 1, m = 2$) and

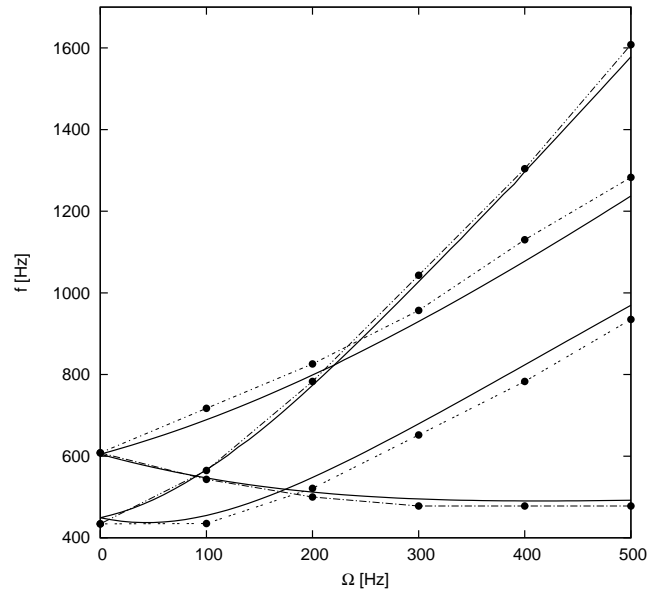


Figure 5.23 Dependency of frequency ratio upon the speed parameter; '-+-': $n = 2$ (Guo et al., 2002), '-x-': $n = 3$ (Guo et al., 2002), '—': TE8 ($\alpha = 0.02$ and $k = 0.5$).

axial bending modes ($n = 1, m = 1$). It should be noted that the non-linear variation of the global bending frequencies predicted by the 1D-CUF elements is quite similar to that presented in (Guo et al., 2001).

Figure 5.25 shows the results for pure radial ($m = 0$) and radial shearing ($m = 1, 2$) modes for n equal to 2 and 3. It is possible to note that a different longitudinal wave number involves changes in the frequency variations, especially for low values of the circumferential wave number n . As also stated in (Guo et al., 2001), these differences are not detectable from the above analytical solutions (Eqs.5.7,5.9). Furthermore, Fig.5.26 illustrates the variations of the extensional and torsional frequencies. Although nearly constant, the two extensional frequencies exhibit different behaviour upon the speed variation. Indeed, the branch related to $m = 0$ grows after $\Omega/f_{00} = 0.25$, while in contrast, for $m = 2$, the frequency decreases after an initial increase. Regarding the torsional frequency, the curve monotonically decreases with the speed, as also shown in (Guo et al., 2001).

Similarly to the case of thin cylinders, Tab.5.25 lists forward and backward dimensionless frequencies for various speed parameters, with and without the initial stress. The structure is clamped at both ends, and the frequencies at standstill are $f_2 = 4993.53$ Hz and $f_3 = 8435.53$ Hz. Despite the thick wall, natural frequencies are considerably lower when the contribution of the initial stress is overlooked, especially for higher speed values. In addition, relative errors are very close to those computed for the thin cylinder in Tab.5.24.

Laminated moderately thick cylinders

The effects of the rotational speed on the natural frequencies have been evaluated also for the laminated cylinders of Sec.5.2.3. Figures 5.27-5.29 show the frequency parameters as functions of the speed for various lamination schemes. In particular, in the first two graphs, bending fre-

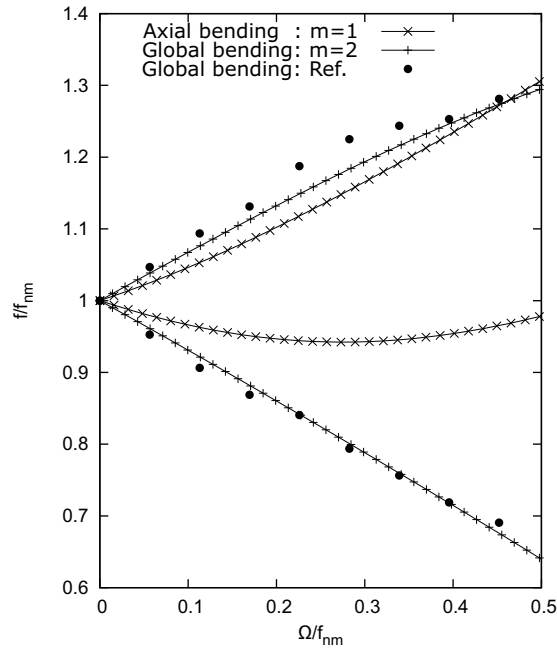


Figure 5.24 Dependency of frequency ratio upon the speed parameter of axial bending and global bending modes. TE9, $n=1$, Ref: (Guo et al., 2001).

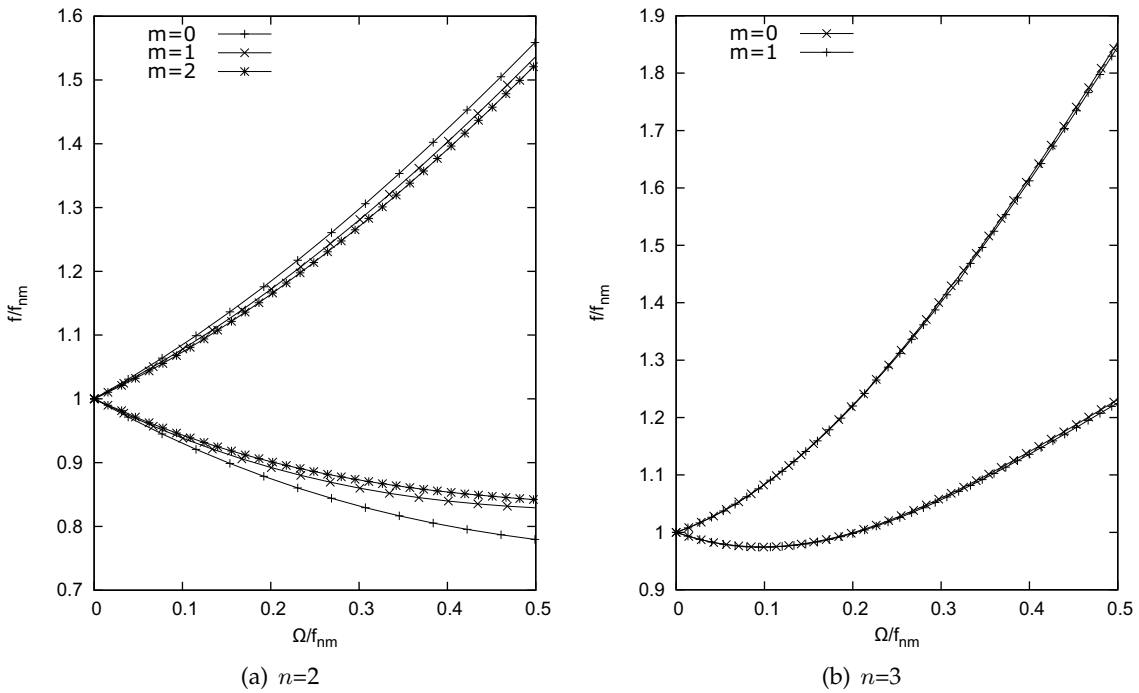


Figure 5.25 Dependency of frequency ratio upon the speed parameter of pure radial ($m=0$) and radial shearing modes ($m=1,2$). TE9.

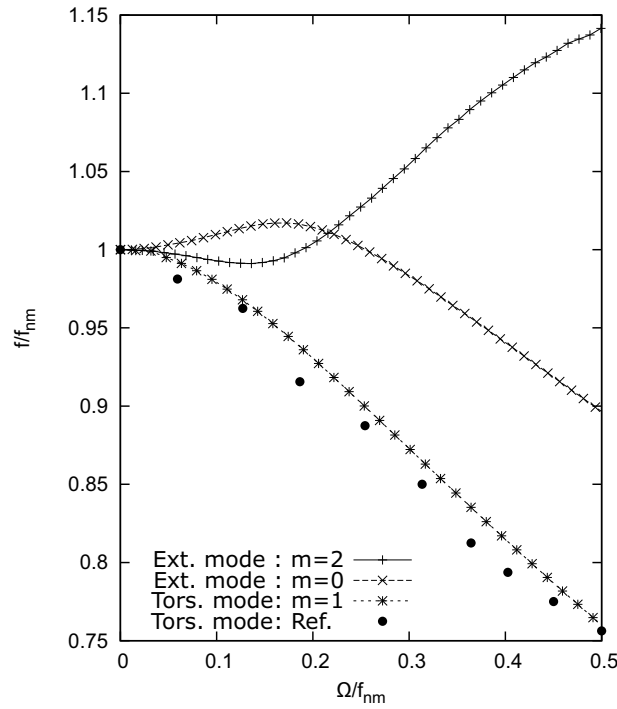


Figure 5.26 Dependency of frequency ratio upon the speed parameter of extensional ($n=0,2, m=0$) and global torsion modes ($n=0, m=0$). TE9, Ref: (Guo et al., 2001).

		Ω/f_n					
		0.0	0.1	0.2	0.3	0.4	0.5
Forward							
f/f_2	with σ_0	1.0	0.93	0.88	0.83	0.80	0.77
	w/o σ_0	1.0 ^(0.0)	0.92 ^(1.1)	0.84 ^(4.5)	0.75 ^(9.6)	0.66 ^(17.5)	0.56 ^(27.3)
f/f_3	with σ_0	1.0	0.97	0.99	1.05	1.12	1.2
	w/o σ_0	1.0 ^(0.0)	0.94 ^(3.1)	0.87 ^(12.1)	0.79 ^(24.8)	0.71 ^(36.6)	0.62 ^(48.3)
Backward							
f/f_2	with σ_0	1.0	1.09	1.18	1.29	1.45	1.56
	w/o σ_0	1.0 ^(0.0)	1.07 ^(1.8)	1.14 ^(3.4)	1.20 ^(7.5)	1.25 ^(13.8)	1.30 ^(16.7)
f/f_3	with σ_0	1.0	1.08	1.22	1.40	1.62	1.86
	w/o σ_0	1.0 ^(0.0)	1.05 ^(2.8)	1.09 ^(10.6)	1.12 ^(20.0)	1.13 ^(30.2)	1.14 ^(38.7)

In brackets, relative errors between the two cases.

Table 5.25 Dimensionless frequencies f/f_n vs. dimensionless speed Ω/f_n with and without the hoop tension for the thick cylinder.

frequencies vary almost linearly only when the lamination schemes are $[0^\circ/0^\circ]$ and $[0^\circ/90^\circ/0^\circ]$. The non-linear trend of the other curves is much more evident for the angle ply configurations and when the longitudinal wave number, m , is equal to 2 (Fig.5.27-b). Figures 5.28-a and 5.28-b show the forward and backward branches for n equal to 2 and 3, respectively. Although the influence of the stacking sequence decreases when ' n ' increases, there remain differences in the frequency variations at higher speed values. Finally, Fig.5.29 reveals that the torsional branch variations also depend on the lamination scheme.

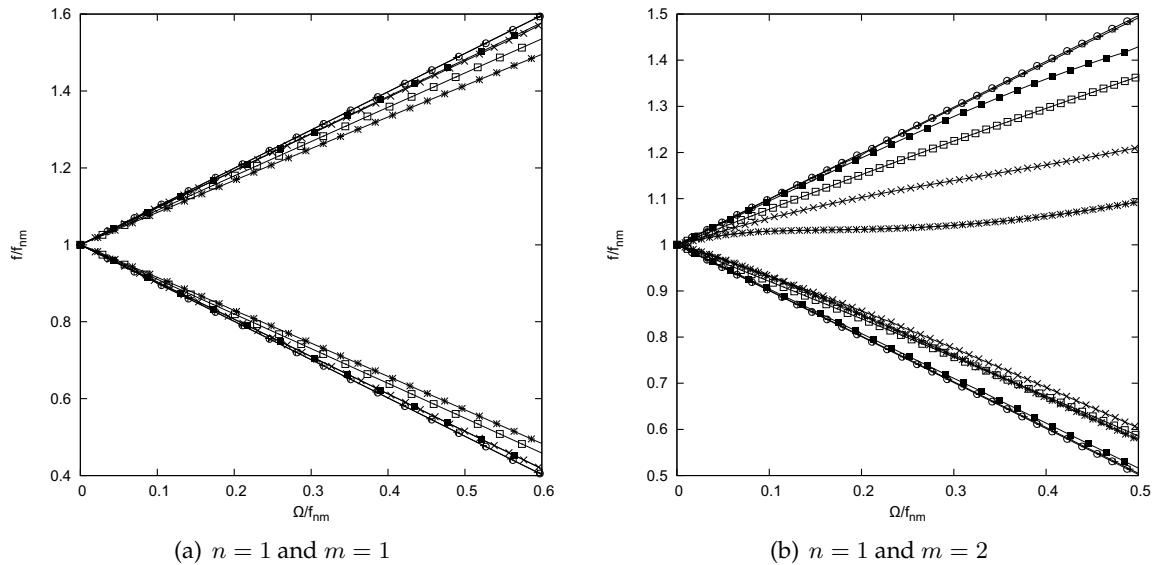


Figure 5.27 Dependency of the frequency ratios upon the speed parameter for two different longitudinal wave number. TE8. '-+-': $[0^\circ/0^\circ]$, '-x-': $[30^\circ/30^\circ]$, '-*-': $[45^\circ/45^\circ]$, '-□-': $[65^\circ/65^\circ]$, '-■-': $[90^\circ/90^\circ]$, '-o-': $[0^\circ/90^\circ/0^\circ]$.

Rotating ring

We now consider a thin ring, rotating about its centre. The mean radius is 0.5 m, and the rectangular cross-section has the width and the height equal to 0.05 and 0.02 m, respectively. The structure made of aluminium (Young's Modulus, $E=73.1$ GPa; density, $\rho=2770$ kg/m³; Poisson's ratio, $\nu=0.33$) has been modelled using 40 9-node Lagrange elements above the cross-section, and 4 2-node beam elements along the longitudinal direction (the total number of degrees of freedom is 3600). Figure 5.30 shows the first natural frequencies as a function of the spin speed and the results are compared with those presented in (Genta, 2005), which were obtained with 40 brick 20-node elements. It should be noted that the 1D results strongly agree with the reference solution for all frequencies, which correspond to out-of-plane and in-plane mode shapes.

Rotating disc

Since the Lagrange-type beam elements allows one to impose non-classical boundary conditions, a thin hollow disc, clamped at the bore, is now considered. The outer radius, the inner radius, and the uniform thickness are 203.2, 101.6 and 1.016 mm, respectively. The material properties are $E=2.1$ GPa, $\rho=7800$ kg/m³, and $\nu=0.3$. The cross-section has been mod-

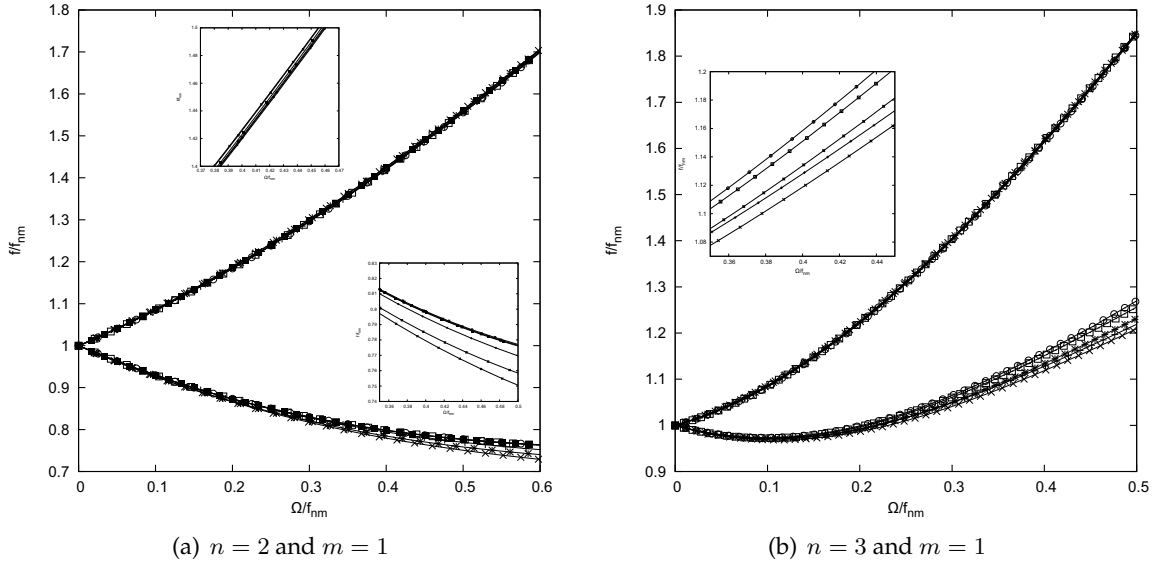


Figure 5.28 Dependency of the frequency ratios upon the speed parameter for two different circumferential wave number. TE8. '-+-': $[0^\circ/0^\circ]$, '-x-': $[30^\circ/30^\circ]$, '-*-': $[45^\circ/45^\circ]$, '-□-': $[65^\circ/65^\circ]$, '-■-': $[90^\circ/90^\circ]$, '-o-': $[0^\circ/90^\circ/0^\circ]$.

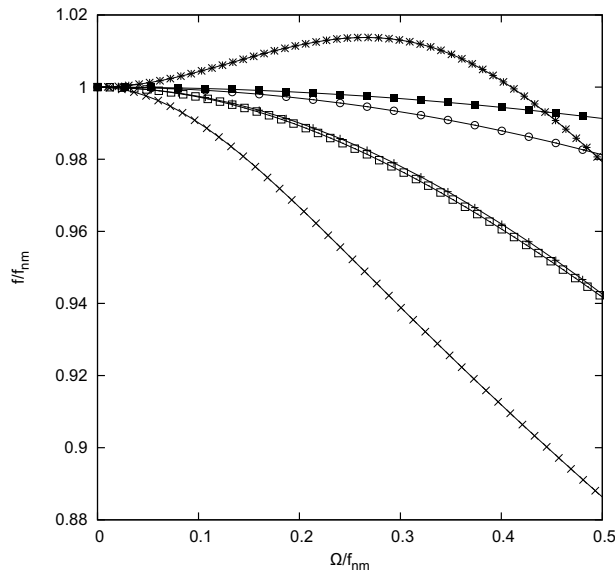


Figure 5.29 Dependency of the frequency ratios upon the speed parameter for the torsional mode. TE8, $n = 1$, $m = 0$. '-+-': $[0^\circ/0^\circ]$, '-x-': $[30^\circ/30^\circ]$, '-*-': $[45^\circ/45^\circ]$, '-□-': $[65^\circ/65^\circ]$, '-■-': $[90^\circ/90^\circ]$, '-o-': $[0^\circ/90^\circ/0^\circ]$.

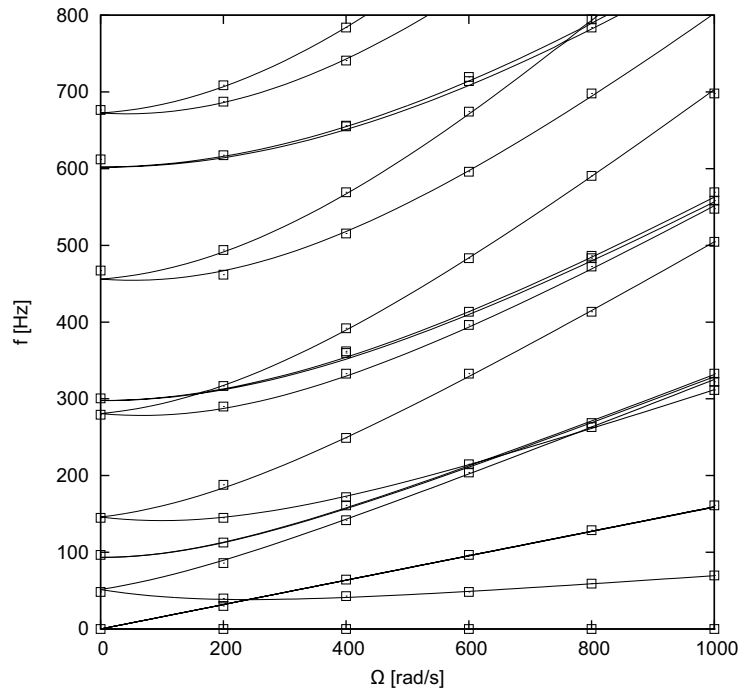


Figure 5.30 Frequencies [Hz] vs. spin speed [rad/s] for a rotating ring; '—': LE9, '□': solid FE model (Genta, 2005)

elled with 40 9-node Lagrange elements (4 in the radial direction, and 10 along the circumference) but, contrary to the previous case, a single 4-node beam element has been used along the longitudinal direction. The total number of degrees of freedom of this mathematical model is 2160. Figures 5.31 graphically show the evolutions of frequencies with the spin speed for modes characterised by a different number of nodal diameters, ' m '. The frequencies have been reported in the inertial frame in order to compare the present solution with the experimental data reported in (Mote and Nieh, 1971). Despite slight differences in the computation of frequencies at $\Omega=0$, graphs reveal that the unified 1D formulation accurately describes the dynamics of highly deformable structures with a low number of degrees of freedom.

Rotating disc on a flexible shaft

The rotor is constituted by a thin disc, whose radius and thickness are $r_d=0.15$, $h_d=0.005$ m, fixed at one-third of a shaft with length, $L_s=0.4$ m, and radius, $r_s=0.01$ m. The rotor is simply supported at each extremity and it is made of steel ($E=207$ GPa, $\rho=7860$ kg/m³, and $\nu=0.28$). The used mathematical model (2010 degrees of freedom) consisted of 12 L3 for the shaft cross-section, 24 L9 for the disc, and 7 4-node beam elements along the longitudinal axis. Figure 5.32 shows the first 7 mode shapes at $\Omega=0$, computed with the proposed beam model.

It should be noted that, except the first 2 modes, the deformability of the disc strongly affects the dynamics of the whole structure. Moreover, in Fig.5.33, the corresponding forward and backward frequencies are compared with results presented in (Combesure and Lazarus, 2008), where Combesure *et al.* provided a solid finite element solution. The comparison reveals that the 1D-CUF formulation leads to accurate results with a limited computational effort demonstrating that complex-shaped rotors can be easily studied with the present approach.

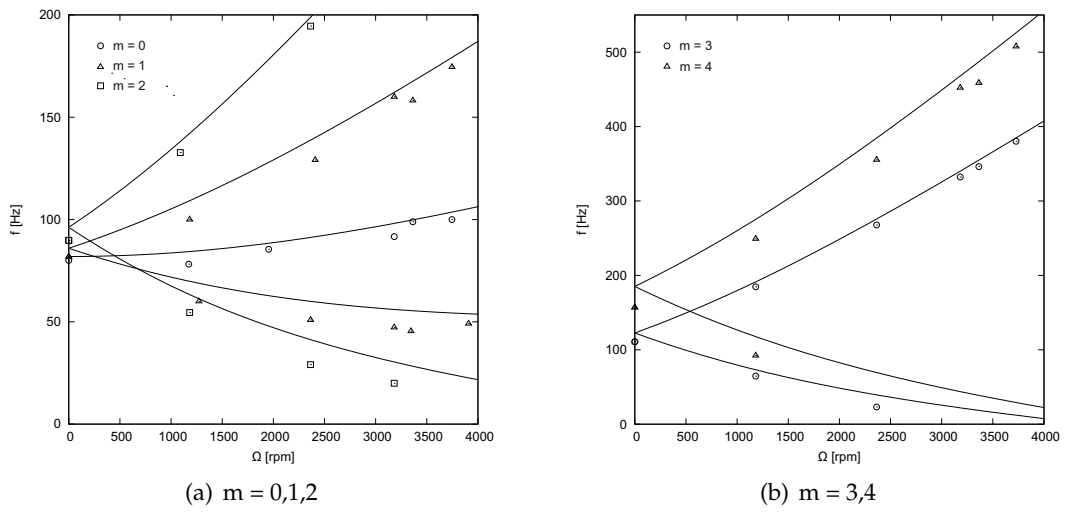


Figure 5.31 Frequencies [Hz] vs. spin speed [rpm] for a rotating disc; '—': LE9, '○', '△', '□': experimental data (Mote and Nieh, 1971).

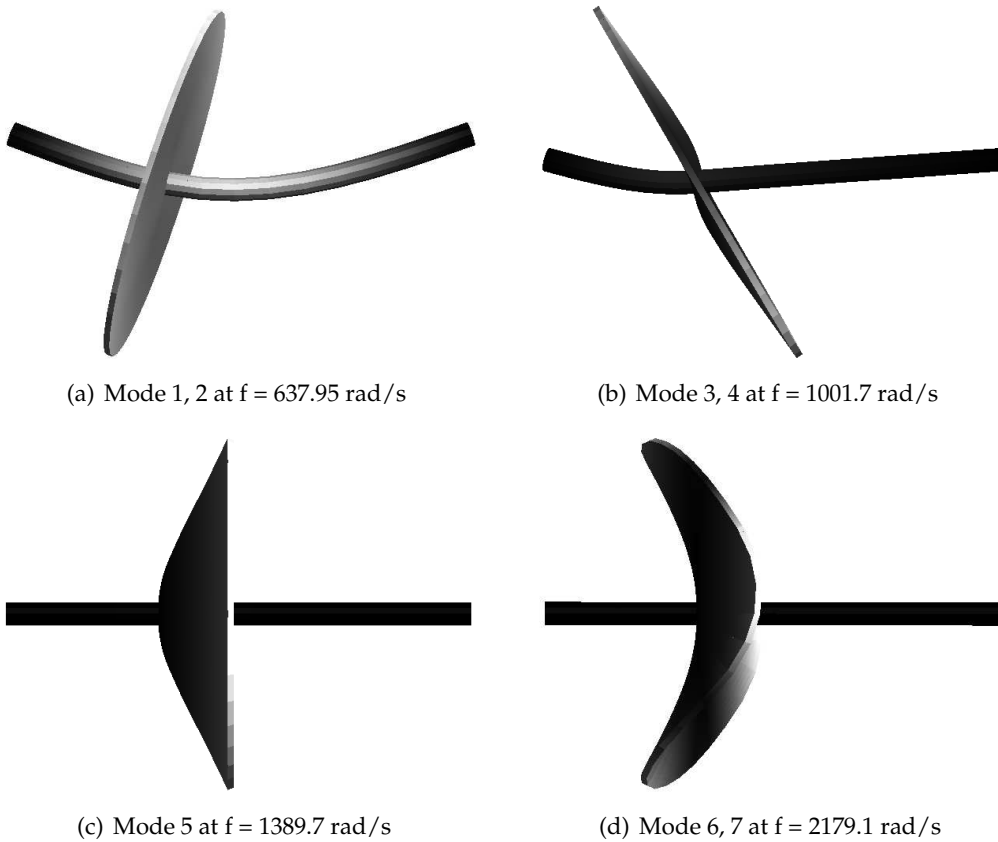


Figure 5.32 First seven mode shapes of the disc on the flexible shaft in the non-rotating state.

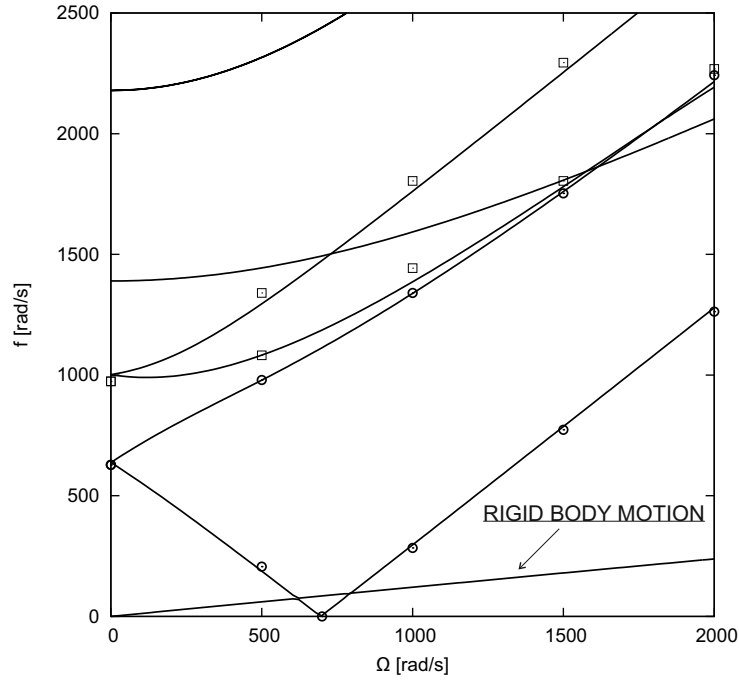


Figure 5.33 Frequencies vs. spin speed for a rotating disc on a flexible shaft; '—': LE model, '○', '□': solid FE model (Combesure and Lazarus, 2008)

5.4 The centrifugally stiffened structures

To assess the theory of Sec.3.3, several illustrative examples are presented. The boundary conditions and the beam dimensions are the problem parameters. To enable a general application of results, if not otherwise declared, they are presented in non-dimensional form adopting the following expressions:

$$\omega^* = \frac{\omega}{\omega_0}, \quad \Omega^* = \frac{\Omega}{\omega_0}, \quad \omega_0 = \sqrt{\frac{\rho AL^4}{EJ_{xx}}} \quad \delta_t = \frac{r_h}{L} \quad S = \sqrt{\frac{AL^2}{J_{xx}}}$$

where J_{xx} is the moment of inertia about x-axis, E is the Young Modulus and A the area of the cross-section. In the first test case, a thin rotating beam is considered and the non-dimensional results obtained in CUF form are compared with those presented in (Banerjee, 2000) where the Dynamic Stiffness Method were applied. As presented in Tab.5.26, the results strongly agree with the reference for all kinds of boundary conditions (B.C.) and for the considered hub offset ratios. The boundary conditions are clamped-free ($C - F$), clamped-supported ($C - P$) and supported-supported ($P - P$). To clarify, the comparison becomes possible if both Coriolis and the Softening matrices are ignored. In the second analysis, the structure is thicker ($S = 30$) to introduce the approximations of Euler-Bernoulli model. To do so, the first order shear deformation theory is needed. The variation of the fundamental non-dimensional frequency of a cantilever Timoshenko beam with the rotating speed is shown in Tab.5.27 and it is compared with (Lee and Kuo, 1993), without the use of any shear correction factor. The agreement between the two sets of results is evident, in fact, the relative error remains below 1%.

Since the unified formulation allows variations of the kinematic theories, higher-order mod-

<i>B.C.</i>	ω^*	<i>Theory</i>	$\Omega^* = 1$		$\Omega^* = 5$	
			$\delta_t = 0$	$\delta_t = 1$	$\delta_t = 2$	$\delta_t = 3$
<i>C - F</i>	1	(Banerjee, 2000)	3.6816	3.8888	10.862	12.483
		Present	3.6816	3.8895	10.866	12.488
	2	(Banerjee, 2000)	22.181	22.375	32.764	35.827
		Present	22.178	22.375	32.773	35.840
	3	(Banerjee, 2000)	61.842	62.043	73.984	77.935
		Present	61.836	62.032	73.986	77.939
<i>C - P</i>	1	(Banerjee, 2000)	15.513	15.650	22.663	24.729
		Present	15.512	15.649	22.670	24.738
	2	(Banerjee, 2000)	50.093	50.277	60.906	64.382
		Present	50.092	50.275	60.919	64.399
	3	(Banerjee, 2000)	104.39	104.59	116.99	121.30
		Present	104.42	104.62	117.04	121.36
<i>P - P</i>	1	(Banerjee, 2000)	10.022	10.264	19.684	22.078
		Present	10.021	10.264	19.690	22.086
	2	(Banerjee, 2000)	39.642	39.889	53.132	57.235
		Present	39.638	39.886	53.141	57.248
	3	(Banerjee, 2000)	88.991	89.241	103.92	108.93
		Present	89.003	89.253	103.94	108.96

Table 5.26 Dependency of the first three dimensionless natural frequency parameters on the variations of the dimensionless angular speed and hub dimension of a Euler-Bernoulli beam.

Ω^*	(Lee and Kuo, 1993)	Present	<i>Diff.</i> (%)
0	3.4798	3.4831	0.09
1	3.6452	3.6494	0.11
2	4.0994	4.1064	0.17
3	4.7558	4.7667	0.22
4	5.5375	5.5530	0.27
5	6.3934	6.4144	0.32
6	7.2929	7.3205	0.37
7	8.2184	8.2538	0.43
8	9.1596	9.2039	0.48
9	10.109	10.164	0.54

Table 5.27 Non-dimensional fundamental frequency ω^* of a cantilever Timoshenko beam as a function of the rotating speed.

els are tested. The considered structures are two graphite-epoxy rectangular beams. For both beams, the width, the length and the hub off-set are 25.4, 800.01 and 63.5 mm, respectively. The thickness and the fiber orientations are different for the two cases and they are listed in Tab.5.28 with the material properties. The reference solutions related to the flapwise normal modes are taken from (Hodges et al., 1996), where some experimental data were reported in graphical form (Epps and Chandra, 1996). As shown in Fig.5.34, the frequencies obtained with CUF are in good agreement with the theoretical approaches and experimental data. It is interesting to note that, the second-degree polynomial is sufficient to detect the bending modes and their related frequency values whereas, for vibration modes dominated by torsion, further refinements are needed to improve the solutions. In fact, using the fourth-degree polynomial, the torsional mode frequencies decrease, getting close to reference values. The remaining frequencies labeled with B_C are related to chordwise modes.

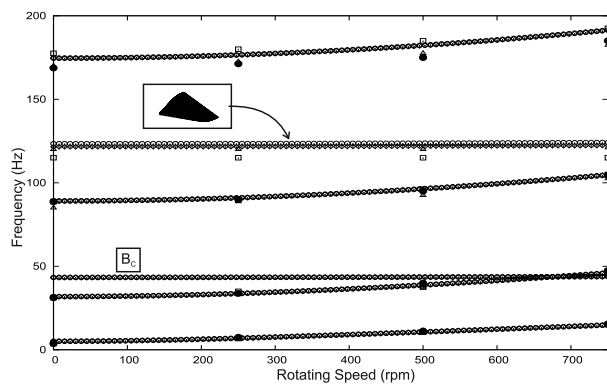
<i>Case</i>	<i>Thickness [mm]</i>	<i>Orientation</i>
1	2.97	0°
2	3.22	15°
<i>Property</i>	<i>Dimension [GPa]</i>	
E_{11}	141.9	
$E_{22} = E_{33}$	9.780	
$G_{21} = G_{31}$	6.140	
G_{32}	5.520	
$\nu_{12} = \nu_{13}$	0.42	
ν_{23}	0.54	

Table 5.28 Material and dimensions of graphite-epoxy beams.

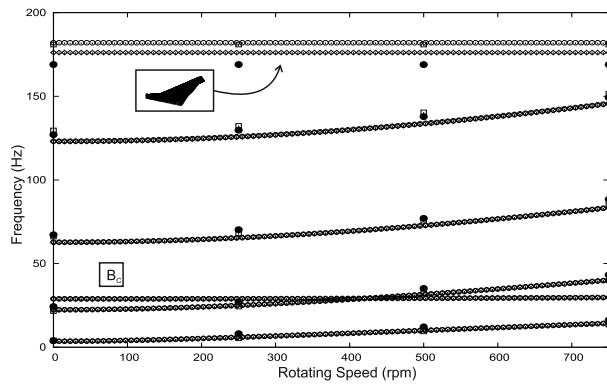
In order to investigate the effects of the ply angle and the rotational speed on the frequencies of more complex and realistic structures, we analyse a thin-walled box with the following geometry features and material properties

$$\begin{aligned}
 E_L &= 206.8GPa & E_T &= 5.17GPa & G_{LT} &= 2.55GPa & G_{TT} &= 3.10GPa \\
 \nu_{LT} &= \nu_{TT} &= 0.25, & \rho &= 1528.15Kg/m^3 \\
 b &= 0.0508m & c &= 0.2540m & t &= 0.01016m
 \end{aligned}$$

where L and T denote parallel and transverse directions to the fibers, b is the width and t the thickness of the beam wall. The beam and hub lengths are assumed to be 2.032 m. In (Song and Librescu, 1997b), the dependency of the first angular frequency on both rotational speed and ply angle orientations was evaluated using a refined theory, where some non-classical effects such as torsion were taken into account. However, in that case, Coriolis terms were discarded in order to split the equations describing the flap-lag bending deformation from those related to the extension-twist motion. In our test case, Coriolis matrix and the term $u_{y,y}$ are included. Figure 5.35 shows the first two angular frequencies changing with the rotational speed for different fiber orientations. The solid lines are obtained with the second-order expansion TE2, whereas the dotted curves with the TE4 expansion. With these two displacement models, it



(a) 0°



(b) 15°

Figure 5.34 Frequencies versus angular speed - "o": Present (TE2), "◇": Present (TE4), "□": Theory (Hodges et al., 1996), "△": Theory (Epps and Chandra, 1996) and "●": Experimental data (Epps and Chandra, 1996).

is possible to detect the flexural-twist coupling when the ply angles are different from 0° and 90° . Focusing on Fig.5.35-a, under a certain value of rotational speed depending on the fiber orientation, the dominant modal shape that exhibits the lowest frequency is the flapwise mode. Due to the centrifugal effect, the frequency rapidly increases until the lag mode frequency becomes the lower of the two. The same phenomenon is observed in Fig.5.35-b for the second angular frequency but, in this case, the threshold speeds determine the interchange between the lag/torsional modal shapes and those that involve flap/extensional deformations. Moreover, for both cases, the curves computed with TE4 undergo a translation toward lower values, whereas the trends remain almost similar.

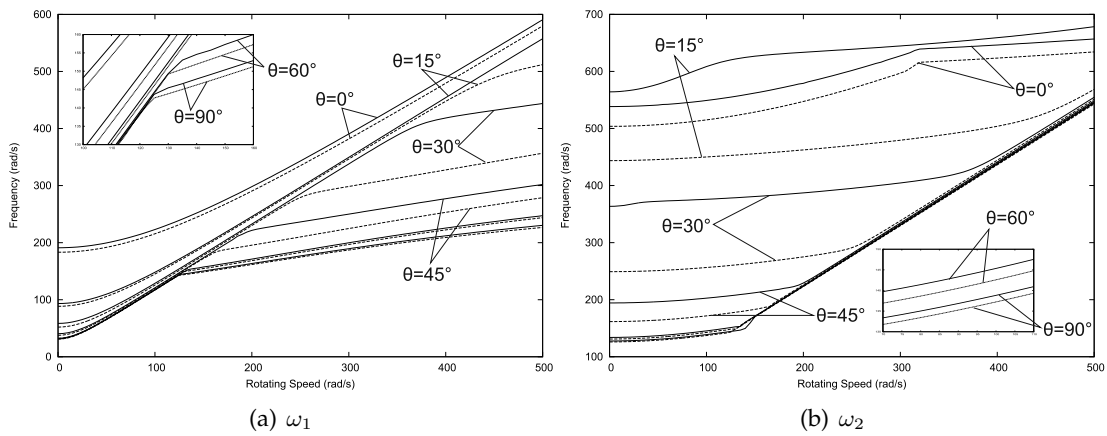


Figure 5.35 First angular frequency versus rotational speed for different ply angles - "solid lines": TE2; "dotted lines":TE4

5.5 Flutter Analyses

5.5.1 Wing structures

A cantilevered straight plate is considered in the first numerical example. The length (L), the thickness (t) and the width (c) of the investigated model are 0.305, 0.0762 and 0.001 m, respectively. The material, whose properties are $E = 73.8$ GPa, $\nu = 0.3$ and $\rho = 2768$ Kg/m³, is isotropic. Both flutter velocity [m/s] and frequency [Hz] are computed using both steady (ST) and unsteady (TM) models with different displacement expansions. These results are reported in Tab.5.29 and compared with those found in (Petrolo, 2011), where the Doublet Lattice Method (DLM) was combined with Carrera's Unified Formulation. In this case, the use of the second-order Taylor-like expansion provides acceptable results with a very low number of degrees of freedom. It should be noted that, with the corrected lift coefficient, the flutter velocities (V_F) computed with the TM are very close to the reference values while, with the ST, they are generally lower. However, the steady theory provided higher values of the flutter frequencies, especially with respect to those computed using Theodorsen's model.

Table 5.29 Flutter conditions for an isotropic plate.

	ST		TM		DLM (Petrolo, 2011)	
	V_F	f_F	V_F	f_F	V_F	f_F
TE2	(50.2)	(45.000)	(60.6)	(36.823)	-	-
	56.1	45.435	67.6	35.945	69.4	40.002
TE3	(49.5)	(42.904)	(59.5)	(35.257)	-	-
	55.6	43.622	66.2	34.363	68.5	39.029
TE4	(49.8)	(43.395)	(59.5)	(35.244)	-	-
	55.6	43.607	66.2	34.350	68.4	38.995

(): the lift coefficient is not corrected.

The effects of the sweep angle (Λ) are then investigated for the same structure. The ST and TM results are compared in Tab.5.30 with those presented in (Pagani et al., 2014), where the Dynamic Stiffness Method (DSM) was combined with DLM in CUF framework. The analyses of swept configurations require the use of more refined displacement theories in order to describe the bending-torsional coupling. For this reason, the third-order theory (TE3) is necessary to ensure convergence of the results. A positive angle of sweep implies a decrease in the flutter conditions. The steady theory again predicts lower flutter velocities and higher frequencies than the TM and DLM, which yield similar velocity values.

Other analyses are carried out on straight and swept composite plates. A six-layer cantilevered beam is first considered, using the same length as in previous structures, and total thickness and width 0.804 and 76.2 mm, respectively. The properties of the orthotropic material are $E_L = 98$ GPa, $E_T = 7.90$ GPa, $G_{LT} = 5.60$ GPa, $\nu = 0.28$ and $\rho = 1520$ kg/m³. The flutter conditions for the stacking sequence $[30_2/0]_S$ are compared in Tab.5.31 with those predicted by the DLM (Petrolo, 2013), using three different displacement theories. Despite the discrepancies between the flutter frequencies, the three aerodynamic approaches again predict similar flutter velocities for this case. This is also confirmed in Tab.5.32 where, for different lamination schemes, the flutter velocities computed using the TE3 displacement model are compared with 2D (CLT) and experimental (EXP) solutions.

Table 5.30 Flutter conditions for an isotropic plate.

Λ	Theory	V_F [m/s]			f_F [Hz]		
		TE2	TE3	TE4	TE2	TE3	TE4
0°	ST	56.086	55.595	55.589	45.435	43.607	43.622
	TM	67.564	66.247	66.231	35.945	34.363	34.350
	DLM(Pagani et al., 2014)	69.388	68.503	68.523	40.002	39.029	38.995
10°	ST	55.949	54.630	54.609	41.602	40.774	40.708
	TM	64.270	63.019	62.986	32.912	32.193	32.155
	DLM(Pagani et al., 2014)	65.441	64.305	64.506	38.362	37.361	37.352
20°	ST	58.665	53.853	53.721	38.914	37.791	37.635
	TM	64.845	60.352	60.210	31.223	29.859	29.770
	DLM(Pagani et al., 2014)	66.408	61.046	59.130	36.736	35.095	34.793
30°	ST	63.627	53.147	52.714	35.803	33.977	33.750
	TM	68.397	57.938	57.514	29.885	27.108	26.864
	DLM(Pagani et al., 2014)	70.145	57.747	57.216	34.156	31.887	31.616

Table 5.31 Flutter condition for a six-layer plate. $[30_2/0]_S$

	ST		TM		DLM (Petrolo, 2013)	
	V_F	f_F	V_F	f_F	V_F	f_F
TE2	25.969	27.185	28.726	23.132	28.820	27.813
TE3	24.007	26.318	26.696	22.142	25.938	26.651
TE4	23.915	26.216	26.590	22.038	25.937	26.650

The influence of the lamination scheme on the flutter conditions is also evaluated considering the $[\theta_2/90_2^\circ/-\theta_2]$ configuration. Figure 5.36 shows the instability velocities computed with the TE3 displacement model as a function of the angle-ply θ . Even though the steady approach yielded more conservative results, it should be noted that the strip theories predict similar variations of the flutter speeds, which reach maximum values between of 40° and 50° . Instead, when the DLM is adopted, the flutter speed initially increases with the angle, and then rapidly decreases when θ is equal to 35° . After this drop, the DLM results fall between those of the two strip theories. Figure 5.37 also shows both the frequencies and velocities of flutter computed with the steady and unsteady strip theories for the symmetric lamination schemes $[\theta/\theta/0^\circ/0^\circ]_S$ as a function of the lamination angle. Again the theories qualitatively yield the same variations for these configurations, which involve bending-torsional coupling, and predict maximum values of the velocities and frequencies for $150^\circ < \theta < 160^\circ$.

A symmetric eight-layer lamination is adopted for the beam configuration. The total thickness of the laminate is equal to 0.804 mm; the stacking sequence is $[-22.5/67.5/22.5/-67.5]_S$, and the thicknesses of plies are 0.03678, 0.04824, 0.06432 and 0.25326 mm, respectively. The natural

Table 5.32 Flutter velocities for a six-layer plate, TE3.

Lamination	ST	TM	CLT(2007)	EXP.(1984)	DLM(Petrolo, 2013)
$[0_2/90]_S$	19.2	23.5	23.0	25	23.2
$[45/-45/0]_S$	40.1	44.2	40.1	>32	40.3
$[45_2/0]_S$	25.0	27.8	27.5	28	26.2
$[30_2/0]_S$	24.0	26.7	27.1	27	25.9

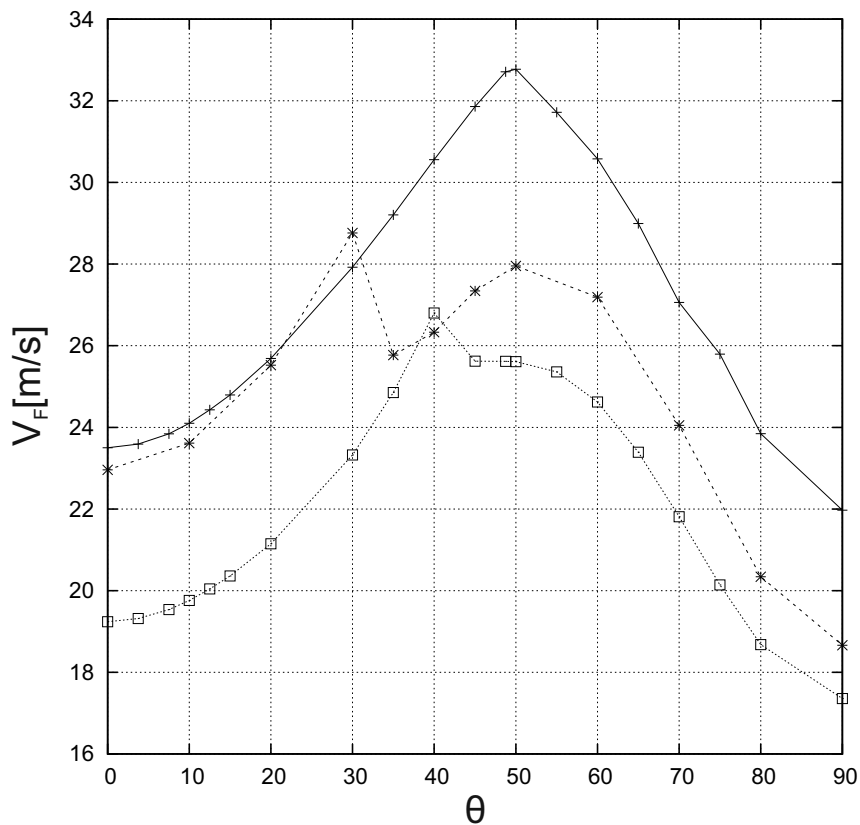


Figure 5.36 Flutter velocities on the angle ply for the lamination case $[\theta_2/90_2^o/-\theta_2]$: - * -: DLM, - + -: TM, - □ -: ST.

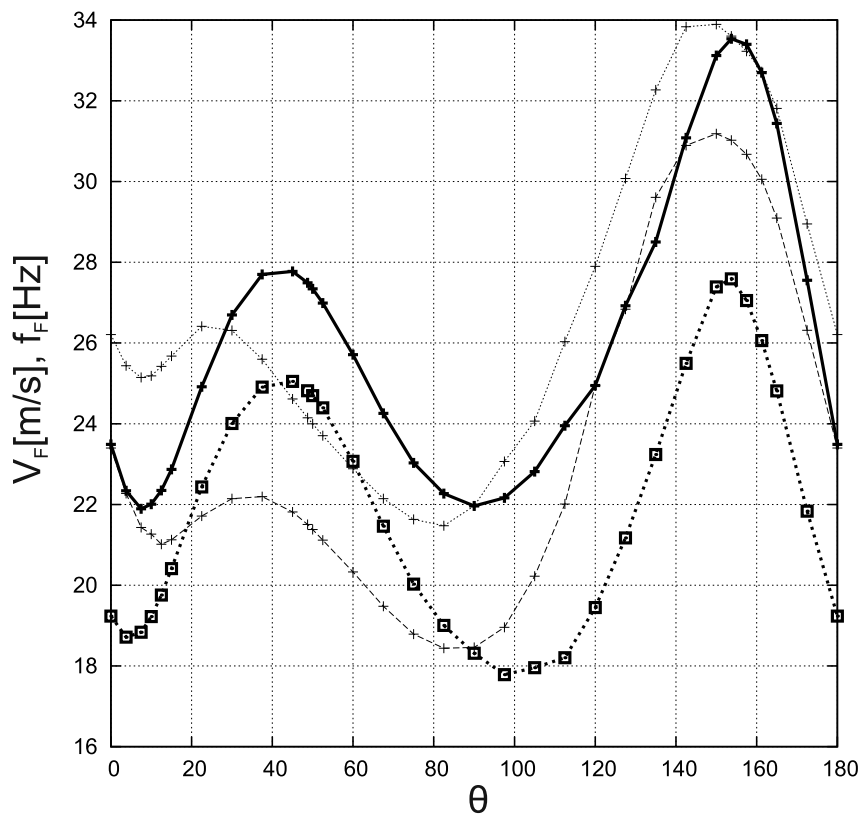


Figure 5.37 Flutter velocities (bold lines) and frequencies (lines) on the angle ply for the lamination case $[\theta/\theta/0^\circ]_s$:
 - + -: TM, -□-: ST.

frequencies (bending and torsion), flutter conditions and the results from the CLT model are presented in Tab.5.33. The above considerations are also valid for this case.

Table 5.33 Flutter velocities [m/s] for an eight-layer plate, TE3.

	f_1	f_2	f_3	f_4	f_5	V_F
$\Lambda = 0^\circ$						
ST	7.2	45.1	59.1	126.5	182.5	30.7
TM	7.2	45.1	59.1	126.5	182.5	36.5
DLM (Petrolo, 2013)	7.2	45.1	58.9	126.5	181.9	38.2
CLT (2007)	7.3	45.4	59.1	127.7	182.3	38.8
$\Lambda = 30^\circ$						
ST	5.6	34.5	59.9	96.2	187.5	29.5
TM	5.6	34.5	59.9	96.2	187.5	32.9
DLM (Petrolo, 2013)	5.6	34.4	59.6	95.9	182.7	32.0
CLT (2007)	5.6	34.4	60.0	95.4	182.0	32.4

Following several studies, where the wing was modelled as a box structure, a prismatic thin-walled beam is considered. The structure, whose dimensions and material properties are listed in Tab.5.34, is discretized with seven 4-node beam-elements .

According to the $[\theta_b/\theta_r/\theta_t/\theta_l]$ configuration of Fig.5.38 and, in order to consider an arbitrary lamination sequence where bending-torsion couplings are likely to occur, the $[\theta/0.1\theta/2\theta/10\theta]$ case is studied. Adopting the fourth-order Taylor-like expansion (TE4), the flutter velocities are computed with the ST, TM and DLM approaches and their trends, as a function of the angle ply, are shown in Fig.5.39. The accuracy of the unsteady strip theory (TM) with respect to the panel method is acceptable, since the maximum relative difference is about 10%, while the steady aerodynamic theory always yielded lower speed values. Moreover, Tab.5.35 shows the flutter velocities for a number of angle values.

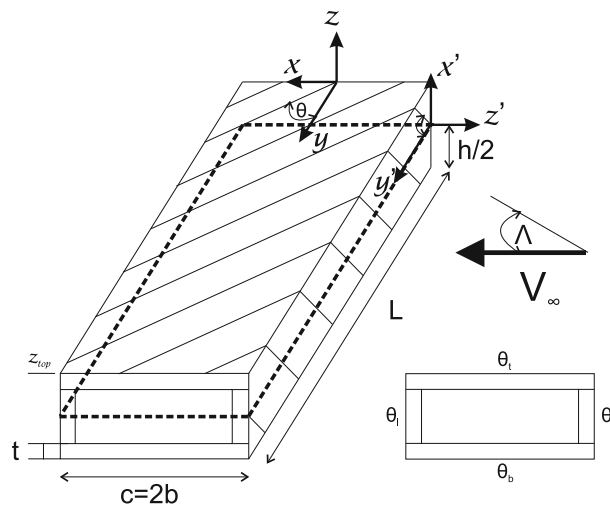


Figure 5.38 Sketch of the box beam and coordinate reference system.

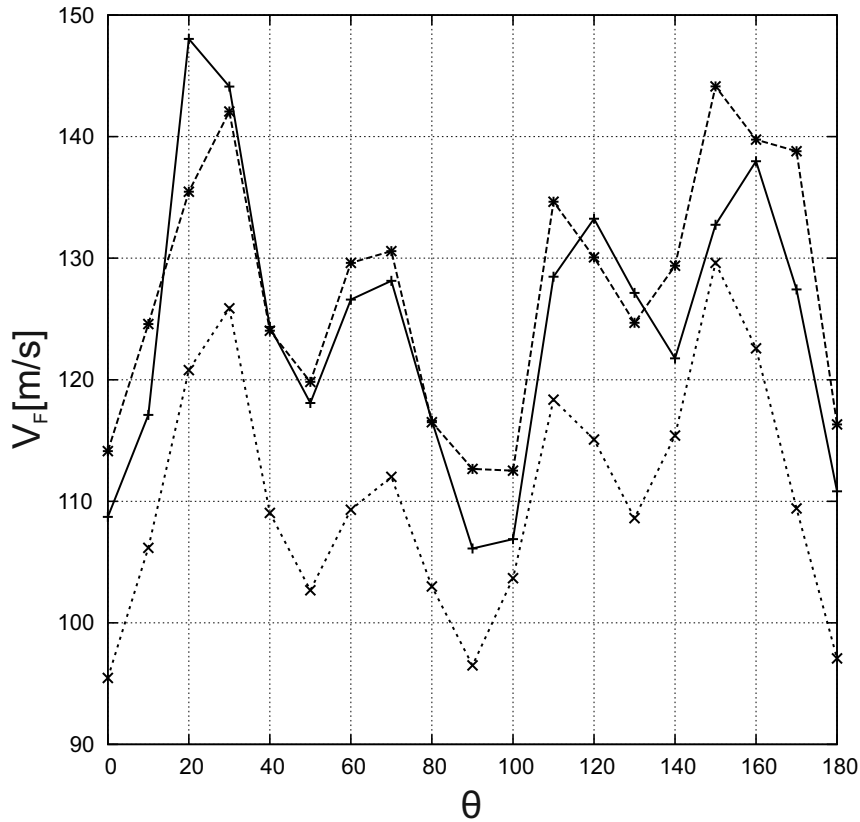
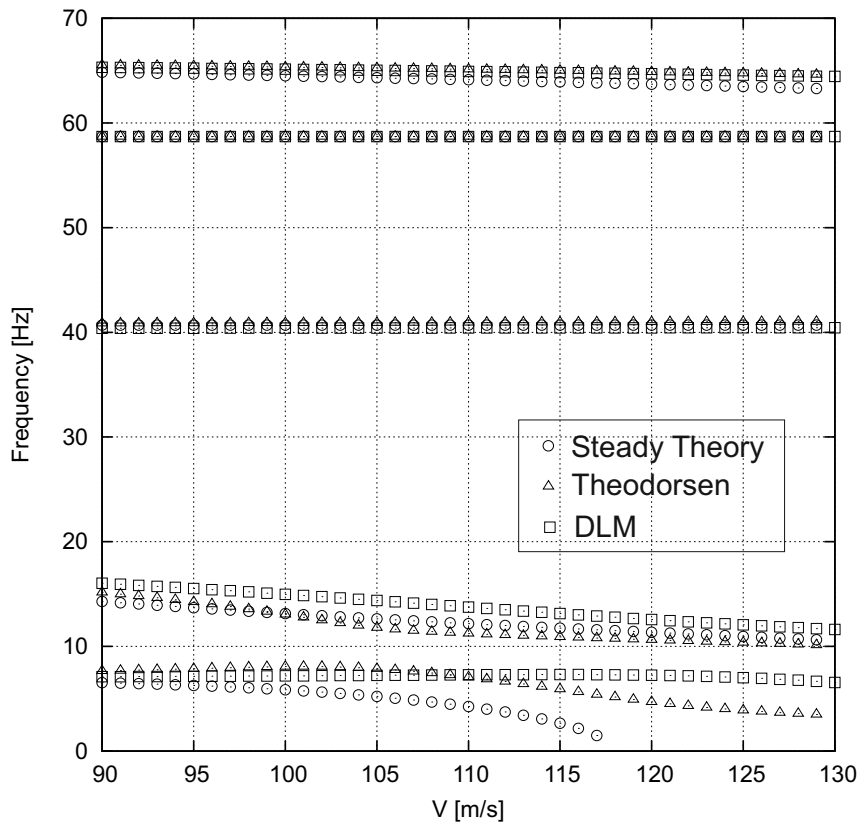


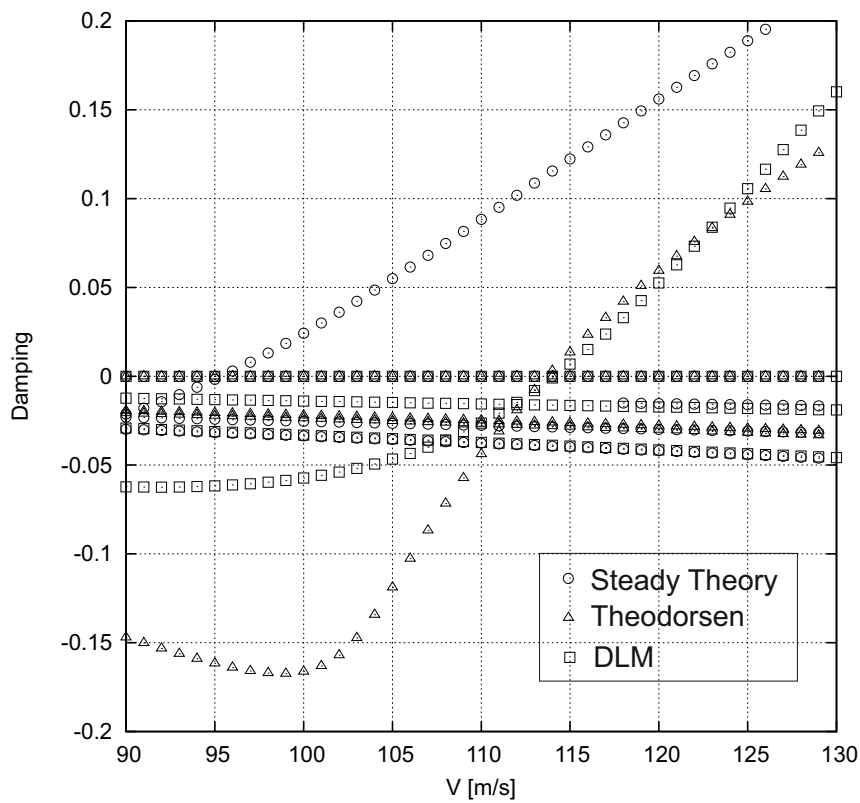
Figure 5.39 Flutter velocities on the angle ply of the box beam: $-\star-$: DLM, $-+-$: TM, $- \times -$: ST.

Figure 5.40 shows the frequency and damping evolutions as functions of speed for $\theta=0$ using the three aerodynamic approaches.

Although it was proved that the unsteady strip theory in the CUF framework provides good results, other analyses are carried out on the previous box structure, using the DLM, in order to compare different lamination solutions. The results shown in Fig.5.41 are normalized with respect to the flutter speed, when θ is equal to 0° . As expected, the solution related to the first scheme $[\theta/\theta/\theta/\theta]$ is symmetric with respect to the minimum flutter speed, which occurs for θ equal to 90° . The two maximum speed values are reached for θ equal to 50° and 130° . Although the worst condition is the same as that of the previous configuration, the second scheme $[-\theta/-\theta/\theta/\theta]$ provides the highest flutter speed for the considered cases, when θ is equal to 20° . Finally, regarding the last case $[\theta/0.1\theta/2\theta/10\theta]$, maximum value (at $\theta = 150^\circ$) is lower than those of previous examples but, interestingly, the minimum speed is the highest (at $\theta = 90^\circ$) with this configuration.



(a) Frequency



(b) Damping

Figure 5.40 Frequency and damping values as functions of speed: TE4

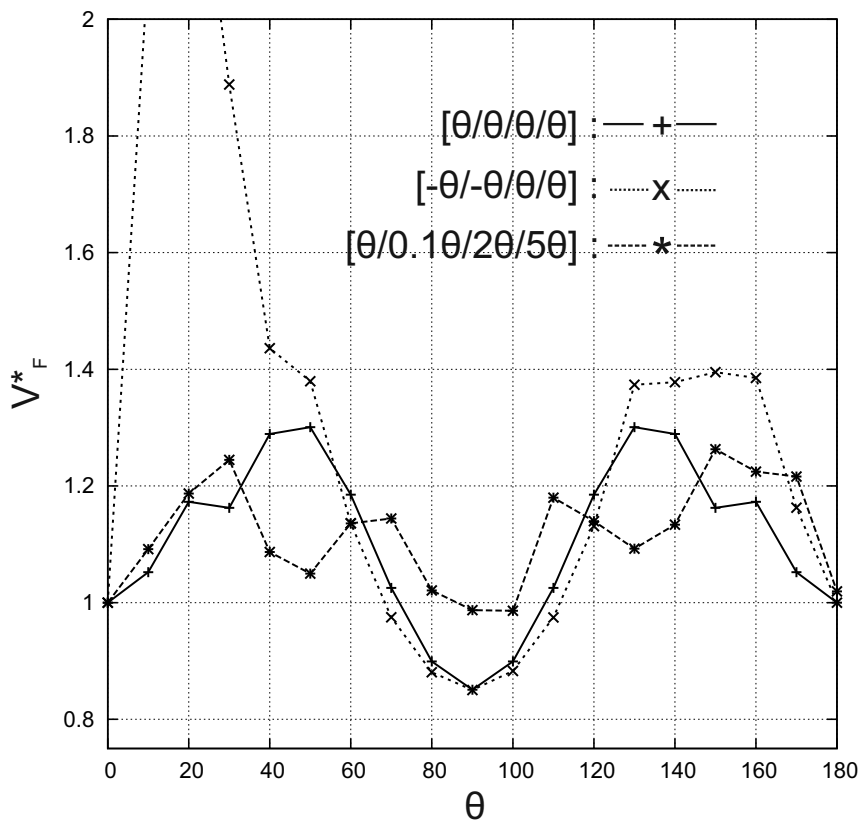


Figure 5.41 Normalized flutter velocities V^*_F on the angle ply of the box beam for three different lamination schemes (DLM).

Table 5.34 Material properties and dimensions of the composite box beam

<i>Property</i>	<i>Dimension</i>
E_{11}	206.8 [Gpa]
E_{22}	5.17 [Gpa]
G_{23}	2.55 [Gpa]
G_{31}	2.55 [Gpa]
G_{12}	3.10 [Gpa]
ν_{12}	0.25
ρ	1528.5 [kg/m ³]
c	0.5[m]
h	$c/15$ [m]
t	$c/150$ [m]
L	3.5[m]

Table 5.35 Flutter velocities [m/s] for the angle ply box beam, TE4.

	0°	30°	60°	90°	120°	150°	180°
ST	95.462	125.88	109.30	96.492	115.08	129.61	97.07
TM	108.71	144.12	126.59	106.11	133.24	132.75	110.82
DLM	114.12	142.06	129.62	112.66	130.07	144.14	116.32

5.5.2 Centrifugally stiffened beams

Isotropic rotating plate

The flutter conditions of an isotropic rotating plate are evaluated using different aerodynamic approaches. The material properties are $E = 74 \text{ GPa}$, $\nu=0.33$ and $\rho=2780 \text{ kg/m}^3$ and, the geometrical features are shown in Fig.5.42.

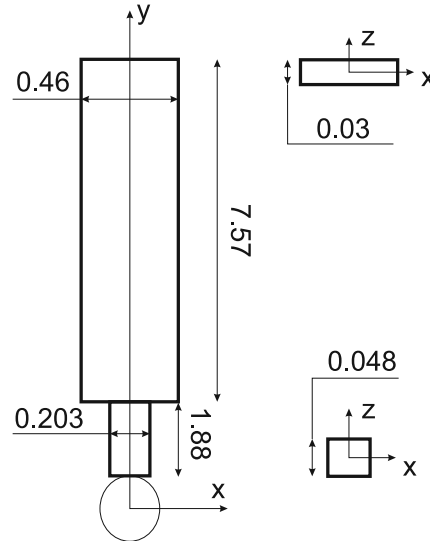


Figure 5.42 Geometrical features of the isotropic rotating plate.

Table 5.36 Flutter velocities [rad/s] for the isotropic rotating plate, TE3.

	\hat{h}	f_F [Hz]	Ω_F [rad/s]
Steady	-	8.14	14.52
Theodorsen	-	5.28	18.71
	4.5	5.32	18.03
Loewy	5.5	5.32	18.06
	6.5	5.22	18.08

Table 5.36 shows the flutter conditions predicted using both steady and unsteady aerodynamic theories. As far as Loewy’s model is concerned, three different spacing factors are considered in order to highlight its effects on the aeroelastic response of the blade. First of all, it is observed that the steady theory predicts a lower value of the flutter speed and a higher frequency with respect to the unsteady approaches. Secondly, despite different spacing factors, the unsteady models leads to very similar results both in terms of frequency and speed.

Rotating multi-section blade: NACA 0012

To demonstrate the capabilities of the refined CUF beam elements, a realistic helicopter blade is here considered. The airfoil is a NACA 0012 and chord and length of the structure are 0.3454 and 5.186 m, respectively. Figure 5.43 shows the blade profile that is constituted by different sections whit the materials listed in Tab.5.37. The structure is cantilevered and it is modelled

with 7 4-node beams. Several problem parameters are evaluated including the lamination angle of the skin ply, the aerodynamic theories and the order of TE models. Firstly, for the ply angle θ equal to zero, Fig.5.44 shows the natural frequencies as a function of the rotational speed by adopting different displacement theories.

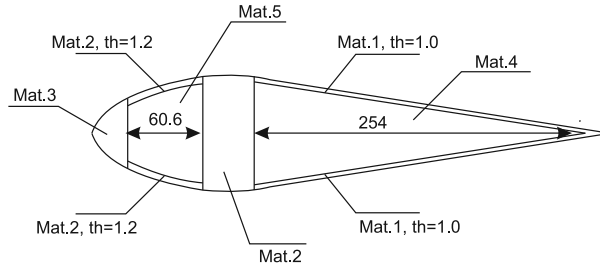


Figure 5.43 Airfoil NACA 0012. The dimensions are in [mm].

Table 5.37 Material properties of airfoil NACA 0012. Elastic moduli in [GPa] and densities in [kg/m³].

Material	E_{11}	E_{11}	E_{11}	G_{12}	G_{31}	G_{23}	ν_{12}	ν_{31}	ν_{23}	ρ
1	139.0	11.0	11.0	6.05	6.05	3.78	0.313	0.313	0.313	1578
2	35.756	15.427	15.427	3.902	3.902	3.902	0.27	0.27	0.27	1826.9
3	1.446	-	-	-	-	-	0.49	-	-	13683.
4	0.0827	-	-	-	-	-	0.2	-	-	190.99
5	0.03105	-	-	-	-	-	0.45	-	-	95.48

–: the material is isotropic.

Despite slight differences in the computation of the torsional frequencies (4th and 6th), the TE3 model ensures acceptable accuracy with a very low number of degrees of freedom. On the other hand, since the choice of the stacking sequence can determine dramatic changes in the dynamic response of rotating structures, Fig.5.45 shows the frequency variations with the rotating speed for a number of lamination angles.

In Figs.5.44 and 5.45, it is possible to note at different speed values, points at which the frequency branches suddenly veer. The "veering" phenomenon determines a temporary coupling of the involved modal shapes that can, in unlucky cases, affect the stability of the rotating structure. In order to observe the evolutions of modes, the Modal Assurance Criterion (MAC) is here exploited. The MAC number is defined as a scalar representing the degree of consistency between two different modal vectors. The MAC takes on values from zero (representing no consistent correspondence) to one (representing a consistent correspondence) and it is defined as

$$\text{MAC}_{ij} = \frac{|\{\phi_{A_i}\}^T \{\phi_{A_j}\}|^2}{\{\phi_{A_i}\}^T \{\phi_{A_i}\} \{\phi_{A_j}\} \{\phi_{A_j}\}^T} \quad (5.10)$$

where $\{\phi_{A_i}\}$ and $\{\phi_{A_j}\}$ are the modal vector $\{\phi_A\}$ at i^{th} and j^{th} speed. Figure 5.46 shows the MAC for speed values close to the "veering" point at approximately 35 [rad/s]. It is noteworthy that, after a phase where modal shapes differ from the original ones, they reappear simply interchanged as after a crossing. This changing can slowly happen increasing, therefore, the speed range where the deformation modes are coupled.

The flutter analyses are carried out by using the aerodynamic models proposed in Sec.4.2. Assuming that the four-blade rotor is operating at a thrust coefficient $C_T = 0.014$, the correspond-

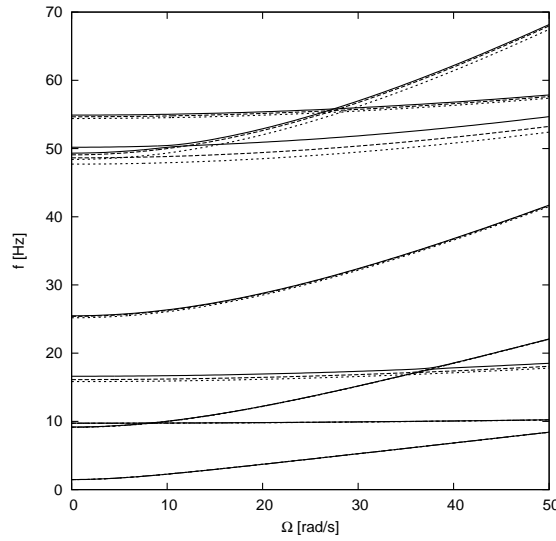


Figure 5.44 Frequency vs rotational speed: '—' TE3, '---' TE4, '...' TE5. $\theta = 0$

ing values of inflow ratio ' λ_0 ' and spacing factors ' \hat{h} ' are 0.084 and 3. Table 5.38 shows the flutter conditions as a function of the lamination angle. The used displacement theories are TE3 and TE4 expansions. It is noteworthy that, in this case, the two unsteady theories lead to extremely different results when the angle is -15 and -30. According to Loewy's model, the lift deficiency function behaves as in Fig.5.47, where for the first reduced frequency shown in the box, the real part is almost equal to 1 while the imaginary is almost null. This fact means that the oscillatory lift excites the first deformation mode at each rotation causing, at a certain velocity, the instability. Clearly, this result is strongly affect by the choice of the spacing factor that represents, therefore, a crucial parameter.

Table 5.38 Flutter velocities [rad/s] and frequencies [Hz] for the NACA-0012.

			θ						
			[-45]	[-30]	[-15]	[0]	[15]	[30]	[45]
Steady	TE3	V_F	44.44	52.55	44.89	22.24	24.39	32.24	32.04
		f_F	16.03	16.15	13.10	13.50	17.76	21.05	19.14
	TE4	V_F	39.64	49.24	42.92	22.25	23.48	30.64	30.32
		f_F	13.69	15.28	12.64	13.00	17.09	19.96	18.30
Theodorsen	TE3	V_F	46.72	54.31	47.72	30.28	27.47	36.40	36.80
		f_F	15.26	16.07	13.48	12.07	16.17	19.38	18.00
	TE4	V_F	40.34	51.41	45.78	29.18	26.43	34.62	34.82
		f_F	13.05	15.27	13.00	11.59	15.59	18.39	17.21
Loewy	TE3	V_F	45.14	26.40	11.00	29.48	25.88	34.70	36.31
		f_F	14.95	0.283	0.151	11.57	14.36	17.64	17.16
	TE4	V_F	39.69	25.03	10.80	26.57	25.03	33.08	34.33
		f_F	13.00	0.270	0.150	9.871	13.94	16.80	16.38

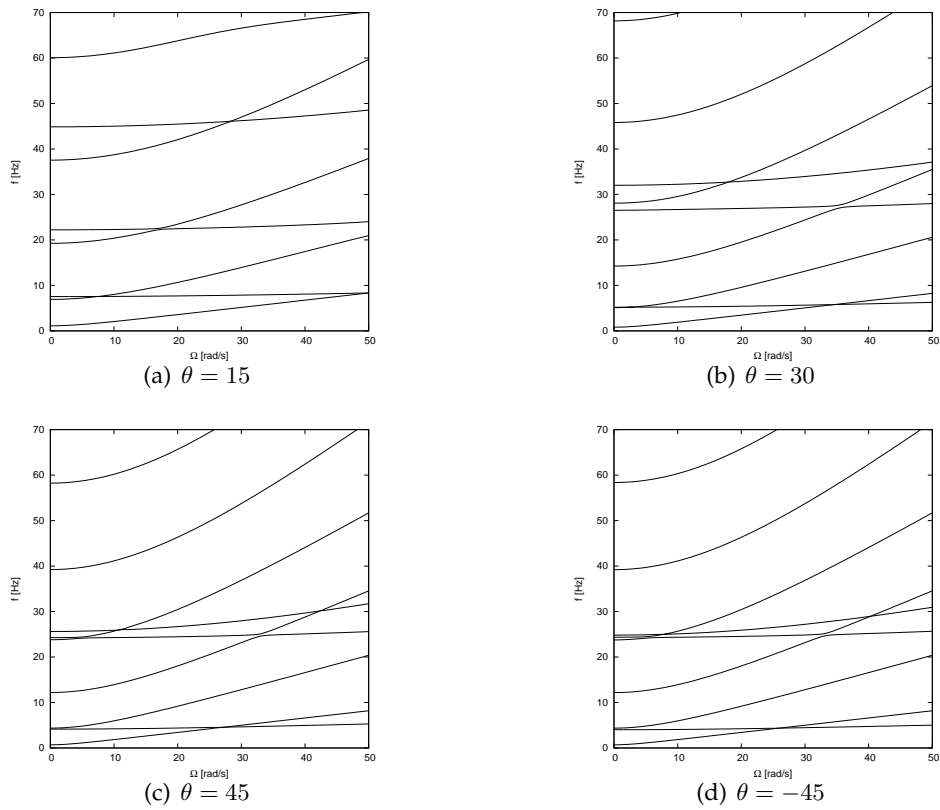


Figure 5.45 Frequency vs rotational speed for various lamination schemes. TE3.

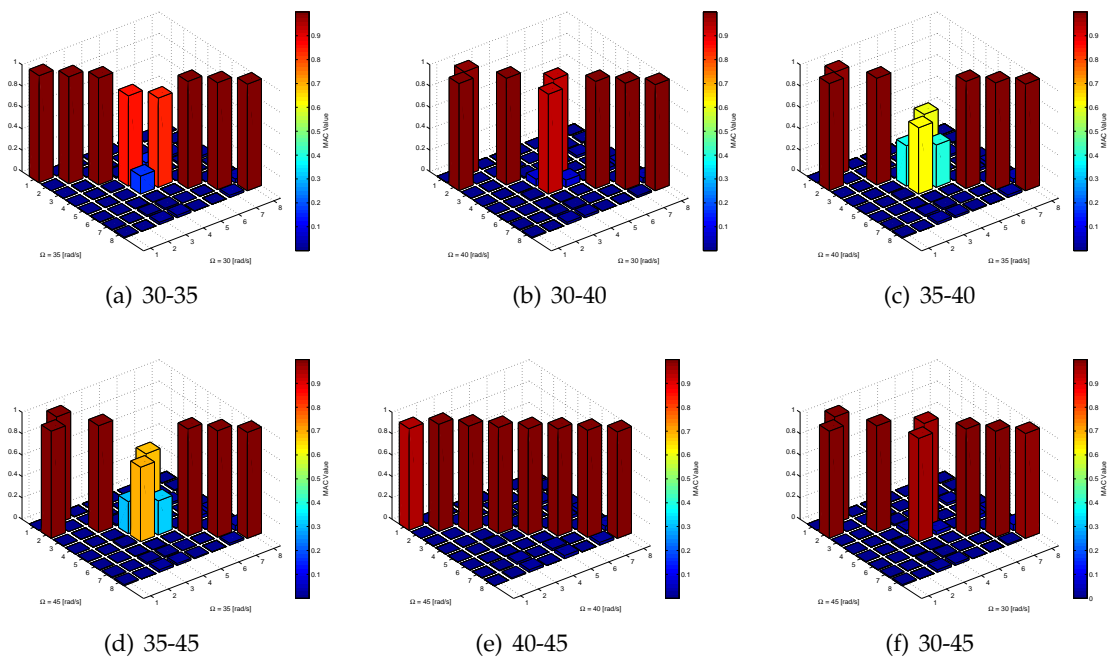


Figure 5.46 MAC values at different rotational speeds for the graph 5.45-b.

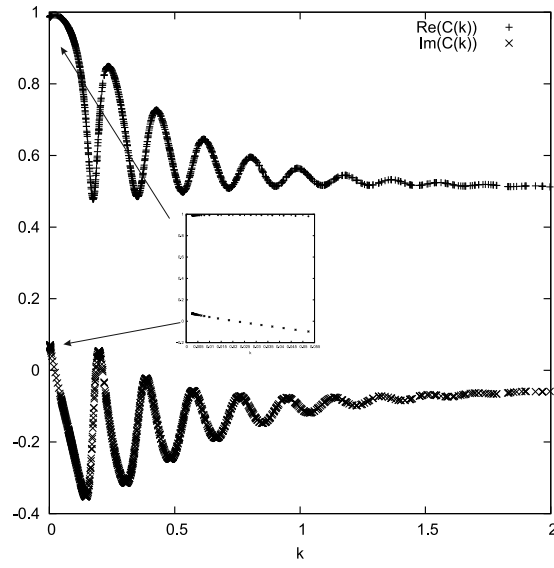


Figure 5.47 Real and imaginary parts of Loewy's deficiency function vs reduced frequency for $\theta = -15$. In the box, the values for the first reduced frequency.

5.6 Rotating plates in a supersonic flow

In this section, the dynamics of a rotating cantilevered plate in a supersonic flow is studied. A number of analysis is carried out considering beams with different values of length-to-thickness (L/h) and length-to-chord (L/c) ratios. The results are obtained for isotropic structures with Young's modulus $E=70$ GPa, Poisson's ratio $\nu=0.3$ and density $\rho=2700$ kg/m³. The air density ρ_a and the speed of sound V_s are assumed to be 24.08 kg/m³ and 344 m/s and, in order to fulfill the condition of supersonic flow on the whole blade surface, the rotational minimum speed (Ω_{min}) must be $1.8 \frac{V_{sound}}{r_h}$. To compare the results presented against results in (Farhadi and Hosseini-Hashemi, 2011), where the piston theory is combined with a non-linear Mindlin first-order shear deformation plate theory. For a thickness-to-length ratio equal to 0.015 and 0.01, Tables 5.39 and 5.40 shows the frequency parameters ($\bar{\omega} = \omega L^2 \sqrt{\frac{12\rho(1-\nu^2)}{Ech}}$) for length-to-width ratio equal to 3 and 2.5, respectively.

Table 5.39 Non-dimensional out-of-plane frequencies for rotating isotropic plate ($h/L = 0.015$, $r_h/L = 1$) at Ω_{min} .

L/c	Theory	$\bar{\omega}_1$	$\bar{\omega}_2$	$\bar{\omega}_3$	$\bar{\omega}_4$	$\bar{\omega}_5$	$\bar{\omega}_6$	$\bar{\omega}_7$	$\bar{\omega}_8$
Free rotation									
3	TE3	42.9	48.1	103.4	125.5	175.5	211.0	243.7	266.0
	TE4	42.9	48.0	103.4	125.2	175.3	210.1	210.3	261.7
	TE5	42.9	48.0	103.4	125.0	175.3	209.3	209.7	258.9
	2D (2011)	41.7	52.8	100.0	125.0	172.2	208.3	211.1	255.6
2.5	TE3	42.9	46.7	103.4	119.9	170.0	180.8	201.9	229.0
	TE4	42.9	46.6	103.4	119.6	150.5	176.6	201.0	214.3
	TE5	42.9	46.6	103.4	119.4	149.4	176.6	200.6	208.1
	2D (2011)	41.7	55.6	100.0	119.4	150.0	172.2	200.0	211.1
Rotation in air medium flow									
3	TE3	43.8	46.9	103.2	125.4	175.4	211.1	243.7	265.9
	TE4	43.8	46.8	103.2	125.2	175.1	209.8	210.8	261.6
	TE5	43.8	46.8	103.2	125.0	175.1	209.0	210.2	258.8
	2D (2011)	41.7	52.8	100.0	125.0	172.2	208.3	216.7	256.1
2.5	TE3	44.5	44.8	103.2	119.9	169.9	180.7	202.0	229.0
	TE4	44.5	44.8	103.2	119.6	150.6	176.4	201.3	214.3
	TE5	44.5	44.8	103.2	119.5	149.7	176.3	200.8	208.1
	2D (2011)	41.7	52.8	100.0	119.4	152.8	172.2	200.0	208.3

Discrepancies are recorded in the computation of the second frequency ' $\bar{\omega}_2$ ' that is, for all studied configurations, related to the torsional mode. Moreover, for h/L equal to 0.01, the 1D theories predict frequency lockings between the first and second values for both L/c ratios and between the third and fourth for the lowest L/c value. These discrepancies are due to the fact that the reference solution was obtained by a plate theory, which takes into account non-linear strain terms that can play an important role especially for highly deformable plates. However, the comparisons confirms that the 1D-CUF elements provide quite accurate descriptions of the aeroelastic behavior of thin structures rotating in a flow.

Similarly to the subsonic case, the flutter instability occurs when a mode is self-excited that is,

Table 5.40 Non-dimensional out-of-plane frequencies for rotating isotropic plate ($h/L = 0.01, r_h/L = 1$) at Ω_{min} .

L/c	Theory	$\bar{\omega}_1$	$\bar{\omega}_2$	$\bar{\omega}_3$	$\bar{\omega}_4$	$\bar{\omega}_5$	$\bar{\omega}_6$	$\bar{\omega}_7$	$\bar{\omega}_8$
Free rotation									
3	TE3	63.9	67.7	152.4	169.8	244.8	257.6	280.7	319.2
	TE4	63.9	67.6	152.4	169.5	216.2	251.8	279.8	297.9
	TE5	63.9	67.6	152.4	169.4	214.7	251.8	279.4	289.5
	2D (2011)	63.3	75.9	151.9	170.9	221.5	246.8	275.3	288.0
2.5	TE3	63.9	66.6	152.2	165.2	181.8	250.3	260.5	272.8
	TE4	63.9	66.6	151.8	160.3	164.9	246.0	253.6	271.8
	TE5	63.9	66.6	151.6	158.7	164.8	238.9	252.3	271.5
	2D (2011)	63.3	76.6	151.3	164.6	170.9	240.5	250.6	269.0
Rotation in air medium flow									
3	TE3	65.3	65.5	151.7	169.7	244.3	256.9	281.6	319.0
	TE4	65.3	65.6	151.7	169.7	217.0	250.6	281.2	297.7
	TE5	65.4	65.7	151.8	169.8	216.2	250.6	280.9	289.5
	2D (2011)	63.3	69.6	145.6	170.9	224.7	237.3	278.5	291.1
2.5	TE3	64.8	65.0	152.1	163.6	182.7	248.6	261.2	273.3
	TE4	65.0	65.2	154.7	154.8	168.9	244.7	253.5	273.3
	TE5	65.1	65.3	154.5	154.6	169.2	238.7	251.4	273.3
	2D (2011)	63.3	75.9	145.6	167.7	183.5	237.3	246.8	272.2

the real part of the related eigenvalue becomes positive. The instability condition depends on several parameters such as structure dimensions and material properties. In Figs.5.48 and 5.49, frequency and damping values of isotropic plates, with length and chord equal to 0.3 and 0.1 m, are shown as functions of the Mach number at the structure tip ($2 \times L$) for 'h/L' equal to 0.01 and 0.005, respectively. For both cases, TE4, TE5 and TE6 displacement theories are used. Looking at the frequency plots, veering, crossing as well as locking phenomena are clearly recognizable for both structures. When the blocking phenomenon occurs, the real parts of the involved eigenvalues diverge and, if one of them becomes positive, the system is unstable. Results reveal that the thinner plate becomes unstable when the maximum velocity reaches a Mach number equal to 5.3, while in contrast, the thicker plate remains stable for all considered speeds. It should be noted that the TE4 expansion does not predict any instability region for the thinner plate.

In the conclusive analyses, we consider the same thinner plate of the previous example ('h/L'=0.005) constituted by two layers of orthotropic materials. The material properties are $E_{11}=98$ GPa, $E_{22}=E_{33}=7.90$ GPa, $\nu_{12}=\nu_{31}=\nu_{23}= 0.28$, $G_{12}=G_{31}=G_{23}= 5.60$ GPa, and $\rho= 1520$ kg/m³. The lamination sequence is anti-symmetric with respect to the mean plane of the plate [$\theta/-\theta$]. Figure 5.50 shows the evolutions of frequency and damping values with the rotational speed. The analyses are carried out using the Taylor-like expansion of sixth-order.

It should be noted that damping values relating to the first 15 mode shapes are negative in the whole speed range considered only for $\theta=75^\circ$ and 90° . This fact demonstrates that a correct choice of the lamination sequence can be an effective way to avoid flutter instabilities, especially when high deformable structures must be used.

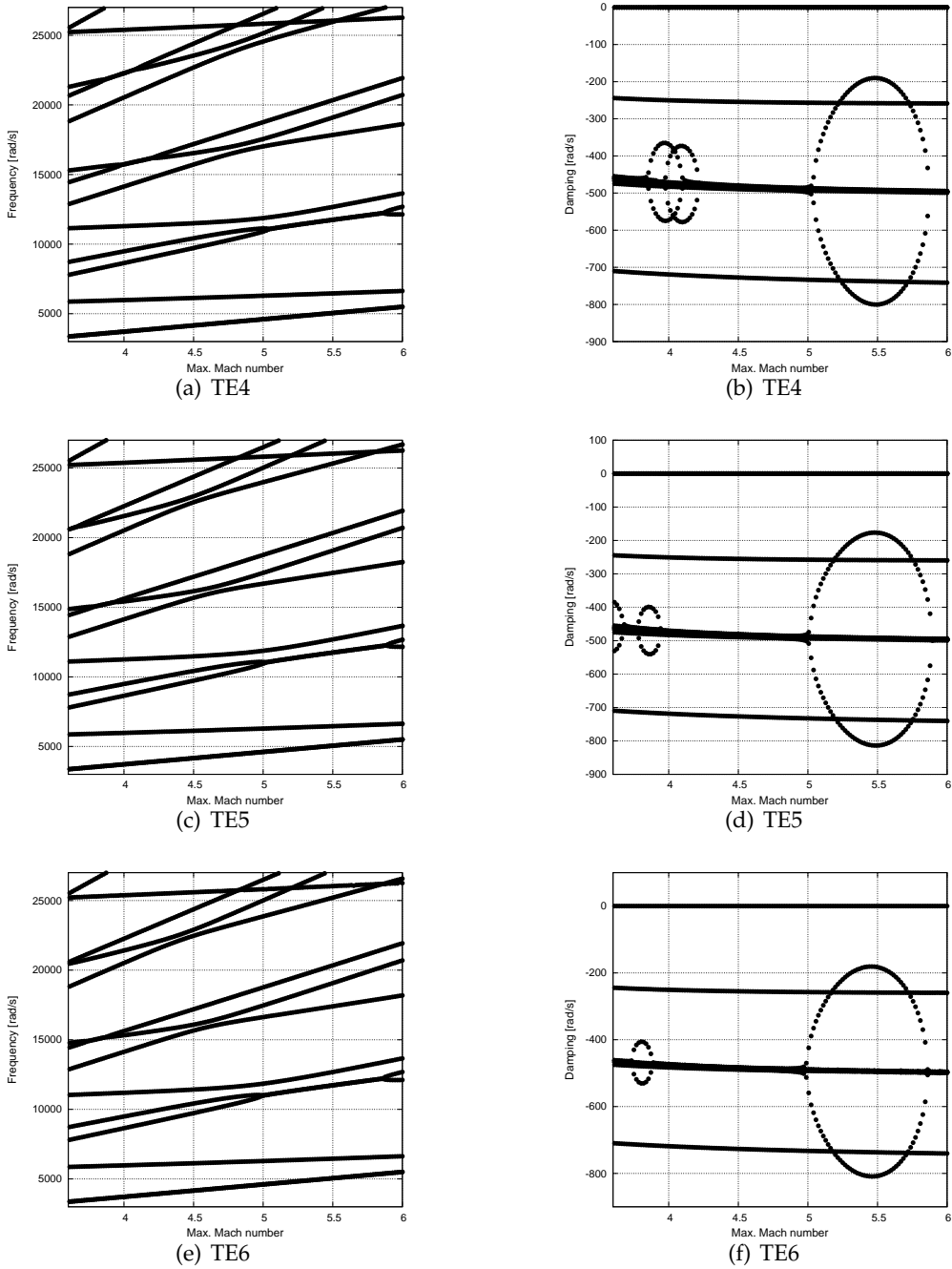


Figure 5.48 Frequency and damping values of an isotropic plate rotating in compressed air with h/L equal to 0.01.

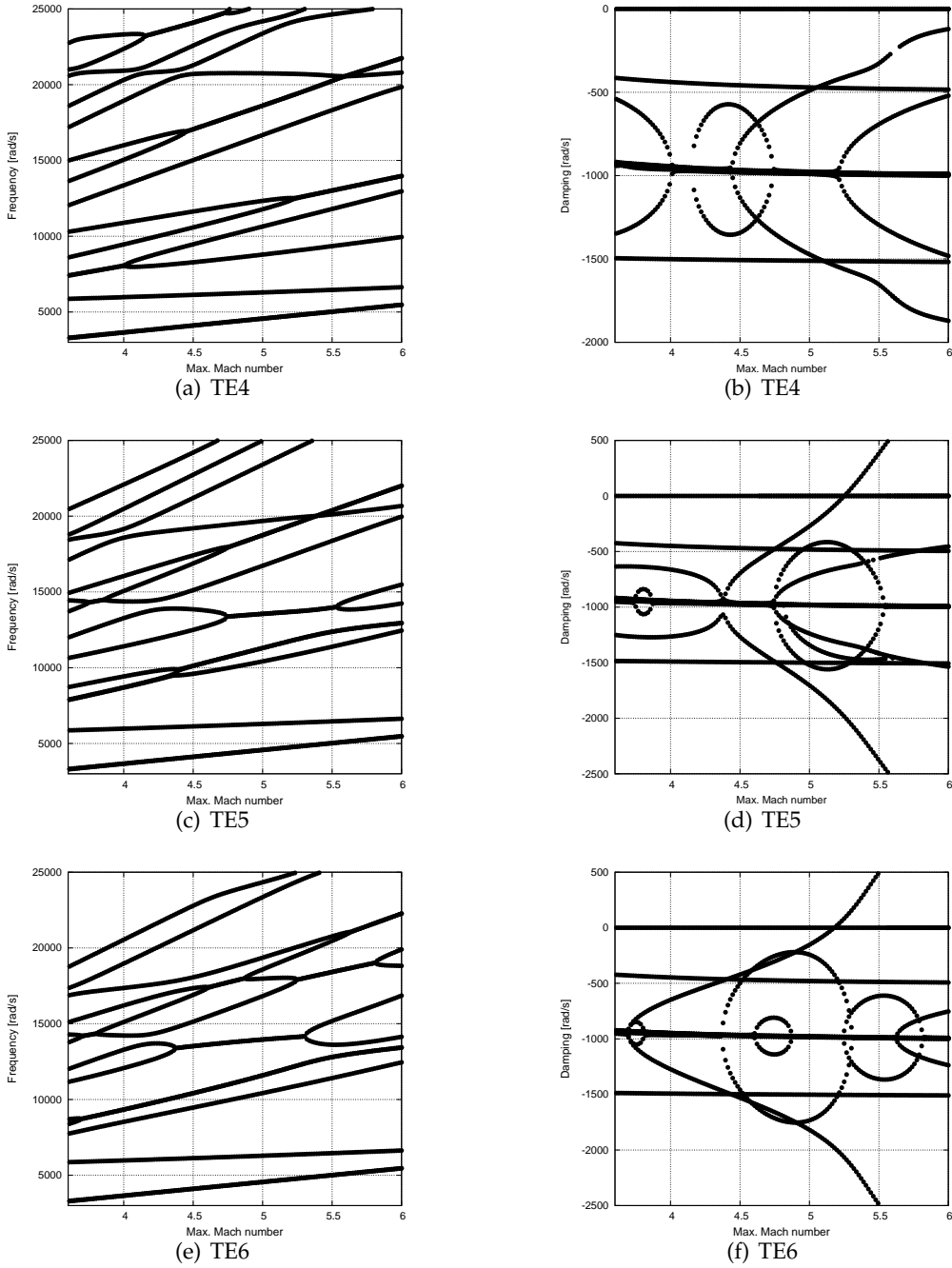
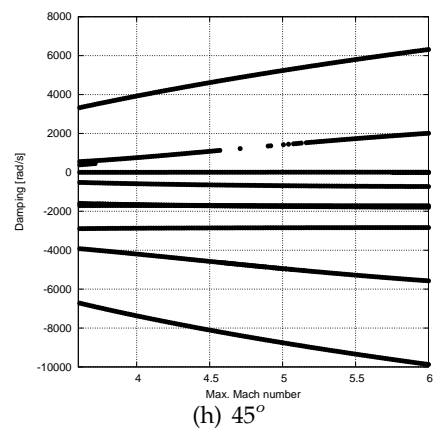
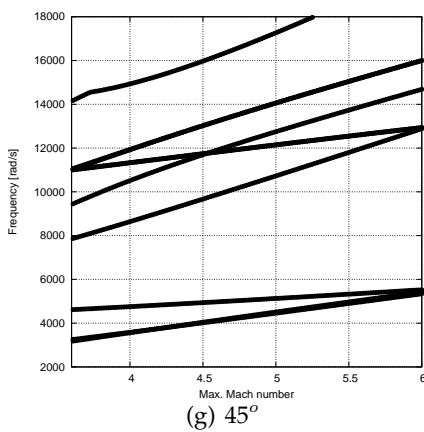
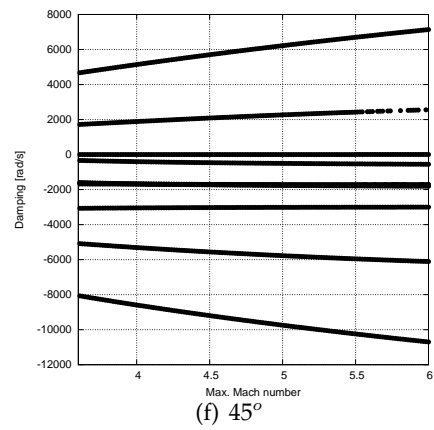
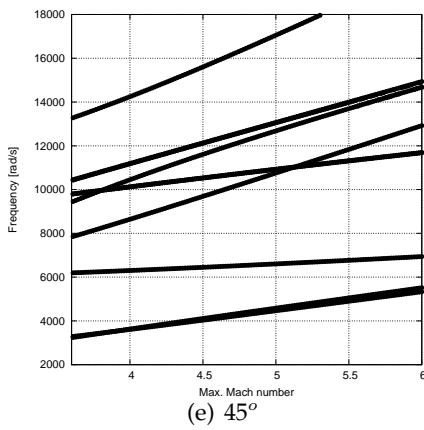
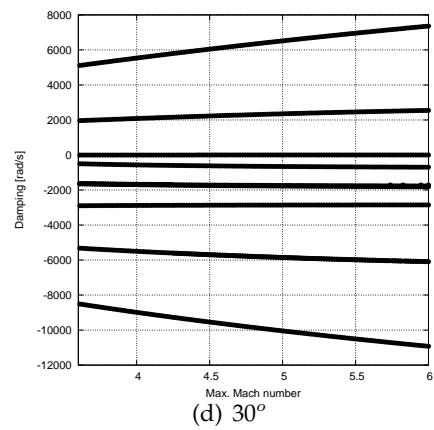
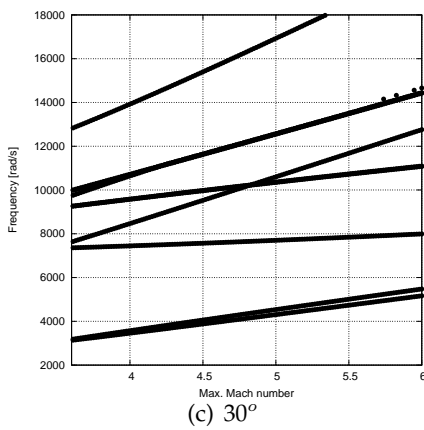
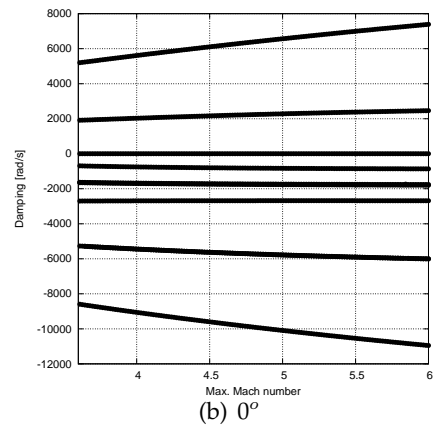
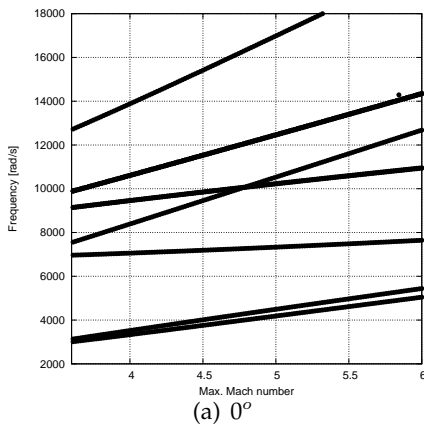


Figure 5.49 Frequency and damping values of an isotropic plate rotating in compressed air with h/L equal to 0.005.



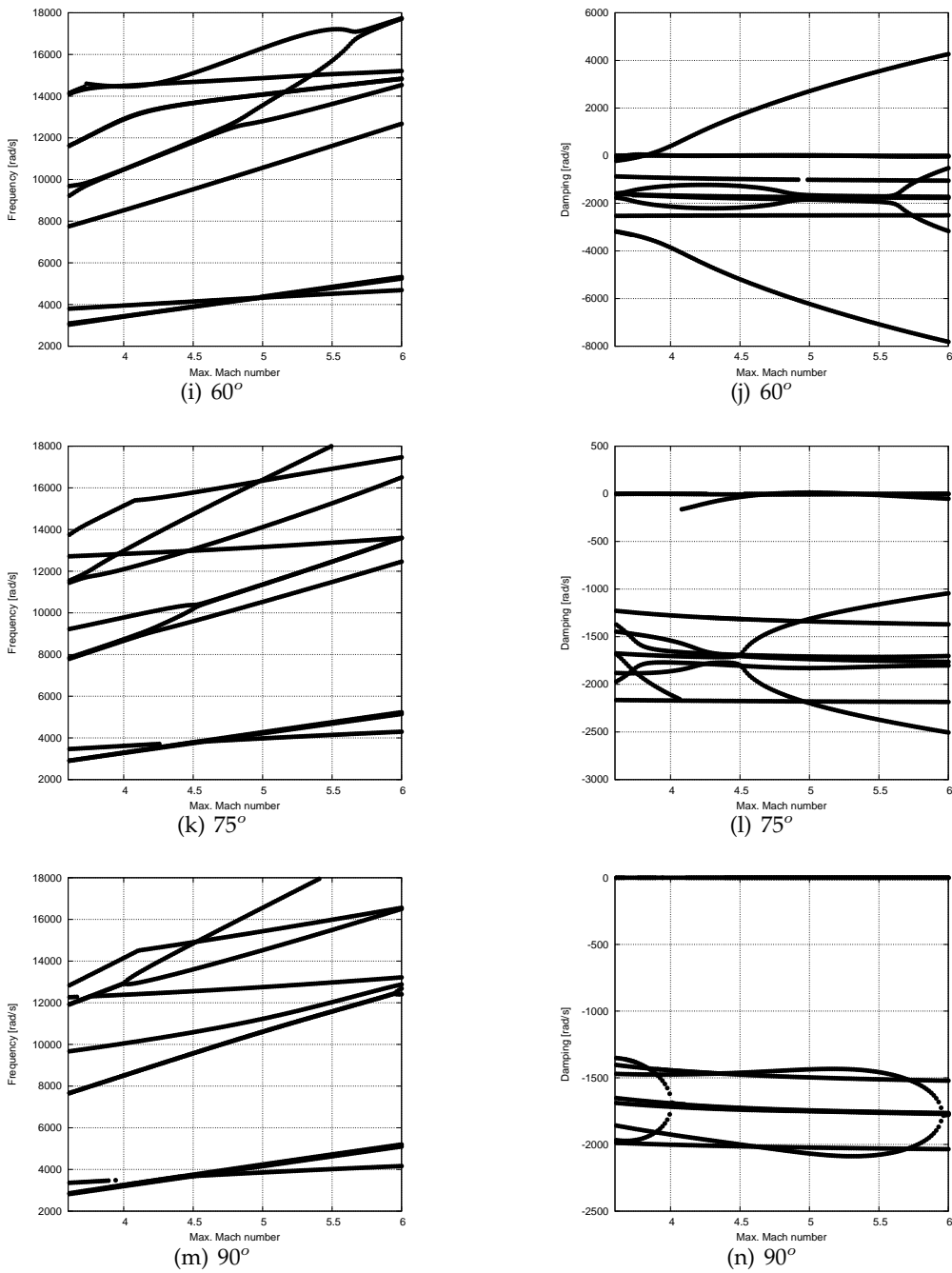


Figure 5.50 Frequency and damping values of a laminated plate rotating in compressed air with h/L equal to 0.005. (TE6)

Chapter 6

Conclusions

This thesis aims to present a simple tool for the aeroelastic analysis of rotating structures. Both steady and unsteady aerodynamic theories are coupled with refined beam theories obtained through Carrera Unified Formulation. The enhanced capabilities of 1D CUF theories allowed to deal with problems that usually require sophisticated solutions with a low number of degrees of freedom.

6.1 Outline and contribution to the literature

The FE and CUF approximations allow the development of several refined beam finite elements. Besides Taylor- and Lagrange-like expansions (TE and LE), the displacement fields are obtained by using several functions including trigonometric, exponential, hyperbolic and zig-zag terms. In order to verify the effectiveness of the finite elements, linear static and free-vibration analyses have been carried out on structures made of composite as well as functionally graded material. In the light of the obtained results, it is clear that

- although the classical beam theories provide acceptable results in terms of displacements and longitudinal stress, they do not describe the correct shear stress distribution, especially when shear effects become relevant;
- the use of refined 1D models is recommended in order to achieve acceptable results when thick structures are considered;
- the zig-zag function significantly improves the solution when thick laminated and sandwich beams are studied;
- 1D CUF beam elements provide results very close to shell and solid finite element solutions;
- the accuracy of the solution strictly depends on the problem characteristics, therefore the possibility to develop an (at least) infinite number of theories appears to be a remarkable feature of the present formulation.

In the second part of this work we have focused on the study of rotors using CUF. The equations of motion, derived through Hamilton's Principle, include both Coriolis term and centrifugal

contributions. The TE elements have been used to perform a number of free-vibration analyses on spinning shafts and blades made of either isotropic or composite materials. Moreover, the higher-order models have allowed evaluation of the dynamic behavior of highly deformable spinning structures such as thin-walled cylinders. To sum up:

- regarding spinning shafts, classical beam theories provide accurate results when slender and metallic structures are considered;
- since the bending-torsional coupling must be described in order to correctly predict the occurrence of instabilities, the higher-order theories are recommended for the study of shafts made of composite materials;
- the initial stress is essential when the wall thickness becomes thin, confirming that classical beam theories are suitable only to study compact cross-sections;
- refined beam models provide reliable results for thick laminated cylindrical shells;
- as for the centrifugally stiffened beams, the present formulation is able to describe both chordwise and flapwise motions;
- 1D CUF elements leads to more accurate results than classical theories when laminated and thin-walled blades are studied;
- since stretching and chordwise motions are coupled by Coriolis matrix, the non-linear term ' $u_{y,y}$ ' introduces a stiffness contribution that can be important for the prediction of divergences.

In the third section, aerodynamic theories have been developed and combined with the refined beam theories. Theodorsen's approach (from which the steady and quasi-steady theories can be easily obtained) has been used to evaluate flutter conditions of various wing configurations including straight and swept structures constituted by isotropic and composite materials. Due to their wide use in the modelling of wings and blades, special attention has been given to thin-walled laminated beams. Flutter speeds and frequencies have been compared with those obtained with the DLM and, with solutions available in the literature, yielding the following findings:

- since the flutter phenomenon involves a bending-torsion coupling, refined beam models are needed to predict an accurate dynamic response of the structure;
- while the steady approach predicts too low flutter velocity values, the unsteady strip theory generally yields results very close to the reference values;
- as expected, the lamination scheme and the sweep angle affect the dynamics of the structures to a great extent. As a consequence, a correct setting of these two parameters is crucial for a the aeroelastic design.

The natural extension of Theodorsen's model for the rotary-wing aeroelasticity, namely Loewy's theory, has been then embedded in CUF framework writing both structural and aerodynamic matrices in terms of *fundamental nuclei*. The differences between classical aerodynamic theories for fixed wings and Loewy's approach have been investigated by analysing metallic and nonhomogeneous blades:

- as expected, the steady approach leads to more conservative results than unsteady models in terms of flutter velocities;
- although different values of the spacing factor ' \hat{h} ' have been considered, Loewy's theory provides results very close to those obtained with Theodorsen's approach for the metallic blade;
- as expected, the stacking sequence strongly affects the aeroelastic response of blades;
- since the inclusion of the returning wave implies the possibility of single-degree-of-freedom flutter in blade torsion, considerable discrepancies between Loewy's and Theodorsen's theory are observed when the nonhomogeneous blade is considered;
- the spacing factor ' \hat{h} ' can affect the solution, therefore it is a crucial parameter for instability predictions.

Finally, the Piston Theory combined with the higher-order structural theories has been adopted in aeroelastic analyses of plates rotating in compressed and supersonic flows. The effects of aspect-ratios and lamination scheme have been evaluated and the results were reported in terms of natural frequencies. In the light of these results, the following conclusions are drawn:

- refined CUF models strongly agree with the reference solutions (obtained with a non-linear plate theory) for the moderately thick rotating plate;
- for the thinnest plate, slight discrepancies are observed in the computation of torsional frequencies and, therefore, frequency blocking phenomena predicted at different rotational speed;
- higher order theories are needed to correctly predict the instability conditions especially when thin structures are considered;
- an adequate choice of the stacking sequence can avoid the occurrence of instabilities.

6.2 Future works

Within this work, Carrera Unified Formulation has shown excellent performance in the study of the dynamics and the aeroelasticity of rotors, therefore paving the way for future research that will include:

1. extension to nonlinear structural analysis (geometrical as well as material nonlinearities);
2. extension to multi-field problems in order to evaluate, for instance, the temperature effects on turbine blades;
3. development of cascade theory for turbine and compressor blades in subsonic and supersonic flows;
4. analysis of complex-shaped rotating structures (swept-tip blades, twisted blades etc.);
5. extension to more sophisticated aerodynamic theories (panel methods, CFD)

Appendix A

In the following section, we present the coefficients of the transformed material matrix \tilde{C} as a function of stiffness material coefficients C and the two angles θ, β .

Isotropic and orthotropic materials

$$\begin{aligned}
\tilde{C}_{33} &= C_{33}\cos^4\theta + 2(C_{23} + 2C_{66})\cos^2\theta\sin^2\theta + C_{22}\sin^4\theta \\
\tilde{C}_{32} &= \cos^2\beta(C_{23}(\cos^4\theta + \sin^4\theta) + (C_{33} + C_{22} - 4C_{66})\cos^2\theta\sin^2\theta) + \sin^2\beta(C_{13}\cos^2\theta + C_{21}\sin^2\theta) \\
\tilde{C}_{31} &= \sin^2\beta(C_{23}(\cos^4\theta + \sin^4\theta) + (C_{33} + C_{22} - 4C_{66})\cos^2\theta\sin^2\theta) + \cos^2\beta(C_{13}\cos^2\theta + C_{21}\sin^2\theta) \\
\tilde{C}_{36} &= \cos\beta((2C_{66} + C_{23} - C_{33})\cos^3\theta\sin\theta + (-2C_{66} + C_{22} - C_{23})\sin^3\theta\cos\theta) \\
\tilde{C}_{22} &= \cos^4\beta(C_{22}\cos^4\theta + (4C_{66} + 2C_{23})\cos^2\theta\sin^2\theta + C_{33}\sin^4\theta) + \\
&\quad + \cos^2\beta\sin^2\beta((4C_{44} + 2C_{21})\cos^2\theta + (4C_{55} + 2C_{13})\sin^2\theta) + C_{11}\sin^4\beta \\
\tilde{C}_{12} &= \cos^2\beta\sin^2\beta((4C_{66} + 2C_{23})\cos^2\theta\sin^2\theta + C_{33}\sin^4\theta - 4C_{55}\sin^2\theta + C_{22}\cos^4\theta - 4C_{44}\cos^2\theta + C_{11}) + \\
&\quad + (\cos^4\beta + \sin^4\beta)(C_{13}\sin^2\theta + C_{21}\cos^2\theta) \\
\tilde{C}_{26} &= \cos^3\beta((2C_{66} + C_{23} - C_{33})\sin^3\theta\cos\theta + (-2C_{66} + C_{22} - C_{33})\cos^3\theta\sin\theta) + \\
&\quad + \cos\beta\sin^2\beta((2C_{44} - 2C_{55} + C_{21} - C_{13})\cos\theta\sin\theta) \\
\tilde{C}_{11} &= C_{11}\cos^4\beta + \cos^2\beta\sin^2\beta((4C_{44} + 2C_{21})\cos^2\theta + (4C_{55} + 2C_{13})\sin^2\theta) + \\
&\quad + \sin^4\beta(C_{22}\cos^4\theta + C_{33}\sin^4\theta + (4C_{66} + 2C_{23})\cos^2\theta\sin^2\theta) \\
\tilde{C}_{16} &= \cos^3\beta(C_{21} - C_{13})\cos\theta\sin\theta + \cos\beta\sin^2\beta((2C_{66} + C_{23} - C_{33})\cos\theta\sin^3\theta + \\
&\quad + (-2C_{66} + C_{22} - C_{23})\cos^3\theta\sin\theta) \\
\tilde{C}_{44} &= (\cos^4\beta + \sin^4\beta)(C_{44}\cos^2\theta + C_{55}\sin^2\theta) + \cos^2\beta\sin^2\beta(C_{11} + C_{22}\cos^4\theta + \\
&\quad + (-2C_{44} - 2C_{12})\cos^2\theta + (-2C_{55} - 2C_{13})\sin^2\theta + (4C_{66} + 2C_{23})\cos^2\theta\sin^2\theta) \\
\tilde{C}_{45} &= \cos^3\beta(C_{44} - C_{55})\cos\theta\sin\theta + \cos\beta\sin^2\beta((-2C_{66} + C_{22} - C_{23})\cos^3\theta\sin\theta + \\
&\quad + (2C_{66} + C_{23} - C_{33})\cos\theta\sin^3\theta + (C_{55} - C_{44} - C_{12} + C_{13})) \\
\tilde{C}_{55} &= \cos^2\beta(C_{55}\cos^2\theta + C_{44}\sin^2\theta) + \sin^2\beta(C_{66}(\cos^4\theta + \sin^4\theta) + \\
&\quad + (C_{33} + C_{22} - 2C_{66} - 2C_{23})\cos^2\theta\sin^2\theta) \\
\tilde{C}_{66} &= \sin^2\beta(C_{55}\cos^2\theta + C_{44}\sin^2\theta) + \cos^2\beta(C_{66}(\cos^4\theta + \sin^4\theta) + \\
&\quad + (C_{33} + C_{22} - 2C_{66} - 2C_{23})\cos^2\theta\sin^2\theta) \\
\tilde{C}_{34} &= \cos\beta\sin\beta((C_{33} + C_{22} - 4C_{66})\cos^2\theta\sin^2\theta + C_{23}(\cos^4\beta + \sin^4\beta) - C_{13}\cos^2\theta - C_{12}\sin^2\theta) \\
\tilde{C}_{35} &= \sin\beta((C_{22} - C_{23} - 2C_{66})\cos\theta\sin^3\theta + (-C_{33} + C_{23} + 2C_{66})\cos^3\theta\sin\theta) \\
\tilde{C}_{24} &= \cos^3\beta\sin\beta(C_{22}\cos^4\theta - (C_{21} + 2C_{44})\cos^2\theta - (4C_{66} + 2C_{23})\cos^2\theta\sin^2\theta + \\
&\quad + (C_{13} + 2C_{55})\sin^2\theta + C_{33}\sin^4\theta) + \cos\beta\sin^3\beta((C_{13} + 2C_{55})\sin^2\theta + (C_{12} + 2C_{44})\cos^2\theta - C_{11}) \\
\tilde{C}_{25} &= \sin^3\beta(C_{21} - C_{13})\cos\theta\sin\theta + \cos\beta\sin^3\beta((2C_{66} + C_{23} - C_{33})\cos\theta\sin^3\theta + \\
&\quad + (-2C_{66} - C_{23} + C_{22})\cos^3\theta\sin\theta + (2C_{55} - 2C_{44})\cos\theta\sin\theta) \\
\tilde{C}_{14} &= \cos\beta\sin^3\beta(C_{22}\cos^4\theta - (C_{21} + 2C_{44})\cos^2\theta - (4C_{66} + 2C_{23})\cos^2\theta\sin^2\theta + \\
&\quad + (C_{13} + 2C_{55})\sin^2\theta + C_{33}\sin^4\theta) + \cos^3\beta\sin\beta((C_{13} + 2C_{55})\sin^2\theta + (C_{12} + 2C_{44})\cos^2\theta - C_{11}) \\
\tilde{C}_{15} &= \sin^3\beta((2C_{66} + C_{23} - C_{33})\cos\theta\sin^3\theta + (-2C_{66} - C_{23} + C_{22})\cos^3\theta\sin\theta) + \\
&\quad + \cos^2\beta\sin\beta(2C_{44} - 2C_{55} + C_{21} - C_{13})\cos\theta\sin\theta \\
\tilde{C}_{45} &= \sin^3\beta(C_{44} - C_{55})\cos\theta\sin\theta + \cos^2\beta\sin\beta((2C_{66} + C_{23} - C_{33})\cos\theta\sin^3\theta + \\
&\quad + (-2C_{66} - C_{23} + C_{22})\cos^3\theta\sin\theta + (C_{55} - C_{44} - C_{21} + C_{13})\cos\theta\sin\theta) \\
\tilde{C}_{56} &= \cos\beta\sin\beta(C_{66}(\cos^4\theta + \sin^4\theta) + (C_{22} + C_{33} - 2C_{23} - 2C_{66})\cos^2\theta\sin^2\theta - C_{44}\sin^2\theta - C_{55}\cos^2\theta)
\end{aligned} \tag{1}$$

Functionally Graded Materials

$$\tilde{C}_{11}^k = \tilde{C}_{22}^k = \tilde{C}_{33}^k = \frac{E(1-\nu)}{(1+\nu)(1-2\nu)} \quad \tilde{C}_{44}^k = \tilde{C}_{55}^k = \tilde{C}_{66}^k = \frac{E}{2(1+\nu)} \tag{2}$$

$$\tilde{C}_{12}^k = \tilde{C}_{13}^k = \tilde{C}_{23}^k = \frac{E\nu}{(1+\nu)(1-2\nu)} \tag{3}$$

Appendix B

For a cross-section made of non-homogeneous orthotropic material, the components of the fundamental nucleus $K^{ij\tau s}$ are

$$\begin{aligned}
K_{xx} &= I_l^{i,yj} \langle F_\tau \tilde{C}_{46} F_{s,z} \rangle + I_l^{i,yj} \langle F_\tau \tilde{C}_{26} F_{s,x} \rangle + I_l^{i,yj,y} \langle F_\tau \tilde{C}_{66} F_s \rangle + \\
& I_l^{ij} \langle F_{\tau,z} \tilde{C}_{44} F_{s,z} \rangle + I_l^{ij} \langle F_{\tau,z} \tilde{C}_{24} F_{s,x} \rangle + I_l^{ij,y} \langle F_{\tau,z} \tilde{C}_{46} F_s \rangle + \\
& I_l^{ij,y} \langle F_{\tau,x} \tilde{C}_{26} F_s \rangle + I_l^{ij} \langle F_{\tau,x} \tilde{C}_{24} F_{s,z} \rangle + I_l^{ij} \langle F_{\tau,x} \tilde{C}_{22} F_{s,x} \rangle \\
K_{xy} &= I_l^{i,yj} \langle F_\tau \tilde{C}_{66} F_{s,x} \rangle + I_l^{i,yj} \langle F_\tau \tilde{C}_{56} F_{s,z} \rangle + I_l^{i,yj,y} \langle F_\tau \tilde{C}_{36} F_s \rangle + \\
& I_l^{ij} \langle F_{\tau,x} \tilde{C}_{26} F_{s,x} \rangle + I_l^{ij} \langle F_{\tau,x} \tilde{C}_{25} F_{s,z} \rangle + I_l^{ij} \langle F_{\tau,x} \tilde{C}_{46} F_{s,x} \rangle + \\
& I_l^{ij} \langle F_{\tau,z} \tilde{C}_{45} F_{s,z} \rangle + I_l^{ij,y} \langle F_{\tau,z} \tilde{C}_{43} F_s \rangle + I_l^{ij,y} \langle F_{\tau,x} \tilde{C}_{23} F_s \rangle \\
K_{xz} &= I_l^{i,yj} \langle F_\tau \tilde{C}_{46} F_{s,x} \rangle + I_l^{i,yj} \langle F_\tau \tilde{C}_{16} F_{s,z} \rangle + I_l^{i,yj,y} \langle F_\tau \tilde{C}_{56} F_s \rangle + \\
& I_l^{ij} \langle F_{\tau,z} \tilde{C}_{44} F_{s,x} \rangle + I_l^{ij} \langle F_{\tau,z} \tilde{C}_{14} F_{s,z} \rangle + I_l^{ij} \langle F_{\tau,x} \tilde{C}_{24} F_{s,x} \rangle + \\
& I_l^{ij} \langle F_{\tau,x} \tilde{C}_{21} F_{s,z} \rangle + I_l^{ij,y} \langle F_{\tau,z} \tilde{C}_{45} F_s \rangle + I_l^{ij,y} \langle F_{\tau,x} \tilde{C}_{25} F_s \rangle \\
K_{yx} &= I_l^{ij,y} \langle F_{\tau,x} \tilde{C}_{66} F_s \rangle + I_l^{ij,y} \langle F_{\tau,x} \tilde{C}_{56} F_s \rangle + I_l^{i,yj} \langle F_\tau \tilde{C}_{43} F_{s,z} \rangle + \\
& I_l^{i,yj} \langle F_\tau \tilde{C}_{23} F_{s,x} \rangle + I_l^{i,yj,y} \langle F_\tau \tilde{C}_{36} F_s \rangle + I_l^{ij} \langle F_{\tau,x} \tilde{C}_{46} F_{s,x} \rangle + \\
& I_l^{ij} \langle F_{\tau,x} \tilde{C}_{26} F_{s,x} \rangle + I_l^{ij} \langle F_{\tau,z} \tilde{C}_{45} F_{s,z} \rangle + I_l^{ij} \langle F_{\tau,z} \tilde{C}_{25} F_{s,x} \rangle \\
K_{yy} &= I_l^{ij} \langle F_{\tau,x} \tilde{C}_{66} F_{s,x} \rangle + I_l^{ij} \langle F_{\tau,x} \tilde{C}_{56} F_{s,z} \rangle + I_l^{ij} \langle F_{\tau,z} \tilde{C}_{56} F_{s,x} \rangle + \\
& I_l^{ij} \langle F_{\tau,z} \tilde{C}_{55} F_{s,z} \rangle + I_l^{ij,y} \langle F_{\tau,x} \tilde{C}_{36} F_s \rangle + I_l^{ij,y} \langle F_{\tau,z} \tilde{C}_{35} F_s \rangle + \\
& I_l^{i,yj} \langle F_\tau \tilde{C}_{36} F_{s,x} \rangle + I_l^{i,yj} \langle F_\tau \tilde{C}_{35} F_{s,z} \rangle + I_l^{i,yj,y} \langle F_\tau \tilde{C}_{33} F_s \rangle \\
K_{yz} &= I_l^{ij} \langle F_{\tau,x} \tilde{C}_{46} F_{s,x} \rangle + I_l^{ij} \langle F_{\tau,x} \tilde{C}_{16} F_{s,z} \rangle + I_l^{ij} \langle F_{\tau,z} \tilde{C}_{45} F_{s,x} \rangle + \\
& I_l^{ij} \langle F_{\tau,z} \tilde{C}_{15} F_{s,z} \rangle + I_l^{ij,y} \langle F_{\tau,x} \tilde{C}_{56} F_s \rangle + I_l^{ij,y} \langle F_{\tau,z} \tilde{C}_{55} F_s \rangle + \\
& I_l^{i,yj} \langle F_\tau \tilde{C}_{43} F_{s,x} \rangle + I_l^{i,yj} \langle F_\tau \tilde{C}_{13} F_{s,z} \rangle + I_l^{i,yj,y} \langle F_\tau \tilde{C}_{35} F_s \rangle \\
K_{zx} &= I_l^{i,yj} \langle F_\tau \tilde{C}_{45} F_{s,z} \rangle + I_l^{i,yj} \langle F_\tau \tilde{C}_{25} F_{s,x} \rangle + I_l^{i,yj,y} \langle F_\tau \tilde{C}_{56} F_s \rangle + \\
& I_l^{ij} \langle F_{\tau,x} \tilde{C}_{44} F_{s,z} \rangle + I_l^{ij} \langle F_{\tau,x} \tilde{C}_{24} F_{s,x} \rangle + I_l^{ij} \langle F_{\tau,z} \tilde{C}_{21} F_{s,x} \rangle + \\
& I_l^{ij} \langle F_{\tau,z} \tilde{C}_{14} F_{s,z} \rangle + I_l^{ij,y} \langle F_{\tau,x} \tilde{C}_{46} F_s \rangle + I_l^{ij,y} \langle F_{\tau,z} \tilde{C}_{16} F_s \rangle \\
K_{zy} &= I_l^{i,yj} \langle F_\tau \tilde{C}_{56} F_{s,x} \rangle + I_l^{i,yj} \langle F_\tau \tilde{C}_{55} F_{s,z} \rangle + I_l^{i,yj,y} \langle F_\tau \tilde{C}_{35} F_s \rangle + \\
& I_l^{ij} \langle F_{\tau,z} \tilde{C}_{16} F_{s,z} \rangle + I_l^{ij} \langle F_{\tau,z} \tilde{C}_{15} F_{s,z} \rangle + I_l^{ij} \langle F_{\tau,x} \tilde{C}_{46} F_{s,x} \rangle + \\
& I_l^{ij} \langle F_{\tau,x} \tilde{C}_{45} F_{s,z} \rangle + I_l^{ij,y} \langle F_{\tau,x} \tilde{C}_{43} F_s \rangle + I_l^{ij,y} \langle F_{\tau,z} \tilde{C}_{13} F_s \rangle \\
K_{zz} &= I_l^{i,yj} \langle F_\tau \tilde{C}_{45} F_{s,x} \rangle + I_l^{i,yj} \langle F_\tau \tilde{C}_{15} F_{s,z} \rangle + I_l^{i,yj,y} \langle F_\tau \tilde{C}_{55} F_s \rangle + \\
& I_l^{ij} \langle F_{\tau,x} \tilde{C}_{44} F_{s,x} \rangle + I_l^{ij} \langle F_{\tau,x} \tilde{C}_{14} F_{s,z} \rangle + I_l^{ij} \langle F_{\tau,z} \tilde{C}_{14} F_{s,x} \rangle + \\
& I_l^{ij} \langle F_{\tau,z} \tilde{C}_{11} F_{s,z} \rangle + I_l^{ij,y} \langle F_{\tau,x} \tilde{C}_{45} F_s \rangle + I_l^{ij,y} \langle F_{\tau,z} \tilde{C}_{15} F_s \rangle
\end{aligned}$$

Bibliography

- Albano, E., Rodden, W., 1969. A doublet-lattice method for calculating lift distributions on oscillating surfaces in subsonic flows. *AIAA Journal* 7, 279–285.
- Ballhause, D., D'Ottavio, M., Kröplin, B., Carrera, E., 2004. A unified formulation to assess multilayered theories for piezoelectric plates. *Computers and Structures* 83, 1217–1235.
- Banerjee, J., 2000. Free vibration of centrifugally stiffened uniform and tapered beams using the dynamic stiffness method. *Journal of Sound and Vibration* 233, 857–875.
- Banerjee, J., 2001. Dynamic stiffness formulation and free vibration analysis of centrifugally stiffened timoshenko beams. *Journal of Sound and Vibration* 247, 97–115.
- Banerjee, J., 2003. A simplified method for the free vibration and flutter analysis of bridge decks. *Journal of Sound and Vibration* 260, 829–845.
- Banerjee, J., Cheung, C., Morishima, R., Perera, M., Njuguna, J., 2007. Free vibration of a three-layered sandwich beam using the dynamic stiffness method and experiment. *International Journal of Solids and Structures* 44, 7543–7563.
- Banerjee, J., Su, H., 2004. Development of a dynamic stiffness matrix for free vibration analysis of spinning beams. *Computers and Structures* 82, 2189–2197.
- Banerjee, J., Su, H., Jackson, D., 2006. Free vibration of rotating tapered beams using the dynamic stiffness method. *Journal of Sound and Vibration* 298, 1034–1054.
- Bauchau, O., 1981. Design, manufacturing and testing of high speed rotating graphite/epoxy shafts PhD Thesis, Department of Aeronautics and Astronautics, MIT.
- Bauer, H., 1980. Vibration of a rotating uniform beam, part 1: Orientation in the axis of rotation. *Journal of Sound and Vibration* 72, 177–189.
- Bennet, R., Edwards, J., 1998. An overview of recent developments in computational aeroelasticity. *AIAA Paper-98-2421*.
- Bert, C., Kim, C., 1992. The effect of bending-twisting coupling on the critical speed of a drive shaft Presented at 6th Japan-U.S. Conference on Composite materials, Orlando, FL.
- Bert, C., Kim, C., 1995. Whirling of composite-material driveshafts including bending-twisting coupling and transverse shear deformation. *Journal of Vibration and Acoustics* 17, 17–21.
- Bielawa, R., 1992. Rotary wing structural dynamics and aeroelasticity. *AIAA*.

- Bir, G., Chopra, I., 1994. Aeromechanical stability of rotorcraft with advanced geometry blades. *Mathl. Comput. Modelling* 19, 159–191.
- Bisplinghoff, R., Ashley, H., Halfman, R., 1996. *Aeroelasticity*. Dover Publications, INC.
- Boukhalfa, A., 2011. Dynamic analysis of a spinning laminated composite-material shaft using the hp- version of the finite element method. *Advances in Vibration Analysis Research*, 161–186.
- Brischetto, S., Carrera, E., 2010. Advanced mixed theories for bending analysis of functionally graded plates. *Computers and Structures* 88, 1474–1483.
- Carrera, E., 2002. Theories and finite elements for multilayered, anisotropic, composite plates and shells. *Archives of Computational Methods in Engineering* 9.
- Carrera, E., 2003. Theories and finite elements for multilayered plates and shells: a unified compact formulation with numerical assessment and benchmarking. *Archives of Computational Methods in Engineering* 10.
- Carrera, E., 2004. Assessment of theories for free vibration analysis of homogeneous and multilayered plates. *Shock and Vibration* 3–4, 261–270.
- Carrera, E., Boscolo, M., Robaldo, A., 2007. Hierarchic multilayered plate elements for coupled multifield problems of piezoelectric adaptive structures: Formulation and numerical assessment. *Archives of Computational Methods in Engineering* 14, 383–430.
- Carrera, E., Cinefra, M., Petrolo, M., Zappino, E., 2014a. *Finite Element Analysis of Structures through Unified Formulation*. Wiley.
- Carrera, E., Cinefra, M., Petrolo, M., Zappino, E., 2014b. *Finite Element Analysis of Structures through Unified Formulation*. Wiley.
- Carrera, E., Filippi, M., 2014. Variable kinematic one-dimensional finite elements for the analysis of rotors made of composite materials. *ASME J Gas Turb Pwr* 136, 092501, doi: 10.1115/1.4027192.
- Carrera, E., Filippi, M., Zappino, E., 2013a. Analysis of rotor dynamic by one-dimensional variable kinematic theories. *Journal of engineering for gas turbines and power* 135, 092501, doi: 10.1115/1.4024381.
- Carrera, E., Filippi, M., Zappino, E., 2013b. Free vibration analysis of laminated beam by polynomial, trigonometric, exponential and zig-zag theories. *Journal of Composite Materials*.
- Carrera, E., Filippi, M., Zappino, E., 2013c. Free vibration analysis of rotating composite blades via carrera unified formulation. *Composite Structures* 106, 317–325, doi: 10.1016/j.compstruct.2013.05.055.
- Carrera, E., Filippi, M., Zappino, E., 2013d. Laminated beam analysis by polynomial, trigonometric, exponential and zig-zag theories. *European Journal of Mechanics - A/Solids* 41, 58–69, doi: 10.1016/j.euromechsol.2013.02.006.

-
- Carrera, E., Giunta, G., 2008. Hierarchical models for failure analysis of plates bent by distributed and localized transverse loadings. *Journal of Zhejiang University. Science A* 9, 600–613.
- Carrera, E., Giunta, G., 2009. Hierarchical evaluation of failure parameters in composite plates. *AIAA Journal* 47, 692–702.
- Carrera, E., Giunta, G., 2010. Refined beam theories based on a unified formulation. *International Journal of Applied Mechanics* 2, 117–143.
- Carrera, E., Giunta, G., Nali, P., Petrolo, M., 2010a. Refined beam elements with arbitrary cross-section geometries. *Computers and Structures* 88.
- Carrera, E., Giunta, G., Nali, P., Petrolo, M., 2010b. Refined beam elements with arbitrary cross-section geometries. *Computers and Structures* 88.
- Carrera, E., Giunta, G., Petrolo, M., 2011a. *Beam Structures. Classical and Advanced Theories*. Wiley.
- Carrera, E., Nali, P., Brischetto, S., 2008. Variational statements and computational models for multifield problems and multilayered structures. *Mechanics of Advanced Materials and Structures* 15, 182–198.
- Carrera, E., Petrolo, M., 2011a. On the effectiveness of higher-order terms in refined beam theories. *Journal of Applied Mechanics* 78.
- Carrera, E., Petrolo, M., 2011b. Refined beam elements with only displacement variables and plate/shell capabilities. *Meccanica* DOI: 10.1007/s11012-011-9466-5.
- Carrera, E., Petrolo, M., 2011c. Refined one-dimensional formulations for laminated structure analysis. *AIAA Journal* Doi: 10.2514/1.J051219.
- Carrera, E., Petrolo, M., Nali, P., 2011b. Unified formulation applied to free vibrations finite element analysis of beams with arbitrary section. *Shock and Vibrations* 18.
- Carrera, E., Petrolo, M., Varello, A., 2012a. Advanced beam formulations for free vibration analysis of conventional and joined wings. *Journal of Aerospace Engineering* 25.
- Carrera, E., Petrolo, M., Wenzel, C., Giunta, G., Belouettar, S., Sept. 2009. Higher order beam finite elements with only displacement degrees of freedom, 1–11XIX Congresso AIMETA, Ancona (IT).
- Carrera, E., Petrolo, M., Zappino, E., 2012b. Performance of cuf approach to analyze the structural behavior of slender bodies. *Journal of Structural Engineering* 138, 285–298.
- Carrera, E., Varello, A., Demasi, L., 2013e. A refined structural model for static aeroelastic response and divergence of metallic and composite wings. *CEAS Aeronautical Journal* 4.
- Carrera, E., Zappino, E., 2014a. Aeroelastic analysis of pinched panels in supersonic changing with altitude. *Journal of Spacecraft and Rockets* 51.
- Carrera, E., Zappino, E., 2014b. Aeroelastic analysis of pinched panels in supersonic flow changing with altitude. *Journal of Spacecraft and Rockets* 51.

- Carrera, E., Zappino, E., Filippi, M., 2013f. Free vibration analysis of thin-walled cylinders reinforced with longitudinal and transversal stiffeners. *Journal of Vibration and Acoustics* 135.
- Carrera, E., Zappino, E., Patočka, K., Komarek, M., Ferrarese, A., Montabone, M., Kotzias, B., Huermann, B., Schwane, R., 2014c. Aeroelastic analysis of Versatile Thermal Insulation (VTI) panels with pinched boundary conditions. *CEAS Space Journal* 6, 23–35, doi: 10.1007/s12567-013-0054-5.
- Catapano, A., Giunta, G., Belouettar, S., Carrera, E., 2011. Static analysis of laminated beams via a unified formulation. *Composite Structures* 94, 75–83.
- Cesnik, C., Hodges, D., Patil, M., 1996. Aeroelastic analysis of composite wings. In *Proceedings of the 37th Structures, Structural Dynamics and Materials Conference*, Salt Lake City, Utah.
- Chandiramani, N., Librescu, L., Shete, C., 2002. On the free-vibration of rotating composite beams using a higher-order shear formulation. *Aerospace Science and Technology* 6, 545–561.
- Chandiramani, N., Librescu, L., Shete, C., 2003. Vibration of higher-order-shearable pretwisted rotating composite blades. *International Journal of Mechanical Sciences* 45, 2017–2041.
- Chang, M., Chen, J., Chang, C., 2004. A simple spinning laminated composite shaft model. *International Journal of Solids and Structures* 41, 637–662.
- Chatelet, E., Lornage, D., Jacquet-Richardet, G., 2002. A three dimensional modeling of the dynamic behavior of composite rotors. *International Journal of Rotating Machinery* 8, 185–192.
- Chen, L., Peng, W., 1998. The stability behavior of rotating composite shafts under axial compressive loads. *Composite Structures* 41, 253–263.
- Chen, M., Liao, Y., 1991. Vibrations of pretwisted spinning beams under axial compressive loads with elastic constraints. *Journal of Sound and Vibration* 147, 497–513.
- Chen, Y., Zhao, H., Shen, Z., Grieger, I., Kröplin, B.-H., 1993. Vibrations of high speed rotating shells with calculations for cylindrical shells. *Journal of Sound and Vibration* 160, 137–160.
- Choi, S.-T., Wu, J.-D., Chou, Y.-T., 2000. Dynamic analysis of a spinning timoshenko beam by the differential quadrature method. *AIAA Journal* 38, 851–856.
- Cicala, P., 1934-1935. Le azioni aerodinamiche sui profili di ala oscillanti in presenza di corrente uniforme. *Mem. R. Accad. Torino*.
- Combescure, D., Lazarus, A., 2008. Refined finite element modelling for the vibration analysis of large rotating machines: Application to the gas turbine modular helium reactor power conversion unit. *Journal of Sound and Vibration* Doi:10.1016/j.jsv.2008.04.025.
- Conlisk, A., 1997. Modern helicopter aerodynamics. *Annu. Rev. Fluid. Mech.* 29, 515–567.
- Curti, G., Raffa, F., Vatta, F., 1991. The dynamic stiffness matrix method in the analysis of rotating systems. *Tribology Transactions* 34, 81–85.

- Curti, G., Raffa, F., Vatta, F., 1992. An analytical approach to the dynamics of rotating shafts. *Meccanica* 27, 285–292.
- Daoud, S., Carrera, E., Zenkour, A., Al Khateeb, S., Filippi, M., 2014. Free vibration of fgm layered beams by various theories and finite elements. *Composites: Part B* 59.
- Dat, R., 1973. Aeroelasticity of rotary wing aircraft. Agard Lecture Series No. 63 on Helicopter Aerodynamics and Dynamics 4.
- Demasi, L., Livne, E., 2009. Dynamic aeroelasticity of structurally nonlinear configurations using linear modally reduced aerodynamic generalized forces. *AIAA Journal* 47, 71–90, doi: 10.2514/1.34797.
- Dowell, E., Clark, R., Cox, D., Curtiss Jr, H., Edwards, J. W., Hall, K. C., Peters, A., Scanlan, R., Simiu, E., Sisto, F., Strganac, W., 2004. *A modern course in aeroelasticity: Fourth Revised and Enlarged Edition*. Kluwer Academic Publishers.
- Ellenberger, G., 1936. Bestimmung der luftkräfte auf einen ebenen tragflügel mit querruder. *Z. angew. Math. Mech.*
- Endo, M., K., K., M., S., O., T., 1984. Flexural vibration of a thin rotating ring. *Journal of Sound and Vibration* 92, 261–272.
- Epps, J., Chandra, R., 1996. The natural frequencies of rotating composite beams with tip sweep. *Journal of the American Helicopter Society* 41, 29–36.
- Farhadi, S., Hosseini-Hashemi, S., 2011. Aeroelastic behavior of cantilevered rotating rectangular plates. *International Journal of Mechanical Sciences* 53.
- Friedmann, P., 1976. Aeroelastic modeling of large wind turbines. *J. Am. Helicopter Soc.* 21, 17–27.
- Friedmann, P., 1980. Aeroelastic stability and response analysis of large horizontal-axis wind turbines. *Journal of Industrial Aerodynamics* 5, 373–401.
- Friedmann, P., 2004. Rotary-wing aeroelasticity: current status and future trends. *AIAA Journal* 42, 1953–1972, doi: 10.2514/1.9022.
- Friedmann, P., Hodges, D., 1977. Recent developments in rotary-wing aeroelasticity. *Journal of Aircraft* 14, 1027–1041, doi: 10.2514/3.58887.
- Friedmann, P., Hodges, D., 2003. Rotary wing aeroelasticity - a historical perspective. *Journal of Aircraft* 40, 1019–1046, doi: 10.2514/2.7216.
- Friedmann, P., Yuan, C., 1977. Effect of modified aerodynamic strip theories on rotor blade aeroelastic stability. *AIAA Journal* 15, 932–940.
- Gem, F., Librescu, L., 1998. Static and dynamic aeroelasticity of advanced aircraft wings carrying external stores. *AIAA Journal* 36, 1121–1129.
- Gem, F., Librescu, L., 2000. Aeroelastic tailoring of composite wings exhibiting nonclassical effects and carrying external stores. *Journal of Aircraft* 37, 1097–1104.

- Genta, G., 2005. Dynamics of rotating systems. Springer, New York.
- Giunta, G., Belouettar, S., Carrera, E., 2010. Analysis of fgm beams by means of classical and advanced theories. *Mechanics of Advanced Materials and Structures* 17, 622–635, dOI: 10.1080/15376494.2010.518930.
- Giunta, G., Biscani, F., Belouettar, S., Ferreira, A., Carrera, E., 2013. Free vibration analysis of composite beams via refined theories. *Composites: Part B* 44, 540–552, dOI: 10.1016/j.compositesb.2012.03.005.
- Giunta, G., Crisafulli, D., Belouettar, S., Carrera, E., 2011. Hierarchical theories for the free vibration analysis of functionally graded beams. *Composite Structures* 94, 68–74.
- Greenberg, J., 1947. Airfoil in sinusoidal motion in a pulsating stream. NACA TN 1326.
- Gubran, H., Gupta, K., 2005. The effect of stacking sequence and coupling mechanisms on the natural frequencies of composite shafts. *Journal of Sound and Vibration* 282, 231–248.
- Guo, D., Chu, F., Zheng, Z., 2001. The influence of rotation on vibration of a thick cylindrical shell. *Journal of Sound and Vibration* 242, 487–505.
- Guo, D., Zheng, Z., Chu, F., 2002. Vibration analysis of spinning cylindrical shells by finite element method. *International Journal of Solids and Structures* 39, 725–739.
- Guo, S., Banerjee, J., Cheung, C., 2003. The effect of laminate lay-up on the flutter speed of composite wings. *Proc. of IMechE, Part G, J. of Aerospace Eng.* 217, 115–122.
- Guo, S., Cheng, W., Degang, C., 2006. Aeroelastic tailoring of composite wing structures by laminate layup optimization. *Technical Notes, AIAA Journal* 44, 3146–3149.
- Ham, H., 1973. Helicopter blade flutter. Agard report No. 607 (revision of part III of the Agard Manual on aeroelasticity) 10.
- Hansen, M., Sorensen, J., Voutsinas, S., Sorensen, N., Madsen, H., 2006. State of the art in wind turbine aerodynamics and aeroelasticity. *Progress in Aerospace Sciences* 42, 285–330, dOI: 10.1016/j.paerosci.2006.10.002.
- Hodges, D., 1990. Review of composite rotor blade modeling. *AIAA Journal* 28, 561–565.
- Hodges, D., Rutkowski, M., 1981. Free-vibration analysis of rotating beams by a variable-order finite-element method. *AIAA Journal* 19, 1459–1466.
- Hodges, D., Shang, X., Cesnik, C., 1996. Finite element solution of nonlinear intrinsic equations for curved composite beams. *Journal of the American Helicopter Society* 41, 313–321.
- Hollowell, S., Dugundji, J., 1984. Aeroelastic flutter and divergence of stiffness coupled, graphite/epoxy cantilevered plates. *Journal of Aircraft* 21, 69–76, dOI: 10.2514/3.48224.
- Howson, W., Zare, A., 2005. Exact dynamic stiffness matrix for flexural vibration of three-layered sandwich beams. *Journal of Sound and Vibration* 282, 753–767.
- Hua, L., Khin-Yong, L., Then-Yong, N., 2005. *Rotating Shell Dynamics*. Elsevier, studies in Applied Mechanics.

- Huang, C. L., Lin, W. Y., Hsiao, K. M., 2010. Free vibration analysis of rotating euler beams at high angular velocity. *Computers and Structures* 88, 991–1001.
- Huttsell, L., Schuster, D., Volk, J., Giesing, J., Love, M., 2001. Evaluation of computational aeroelasticity codes for loads and flutter. *AIAA Paper* 2001-0569.
- Ibrahim, S., Carrera, E., Petrolo, M., Zappino, E., 2012. Buckling of composite thin walled beams by refined theory. *Composite Structures* 94, 563–570.
- Jean Wu-Zheng, Z., P.S. Han, R., 1992. Natural frequencies and normal modes of a spinning timoshenko beam with general boundary conditions. *Journal of Applied Mechanics* 59, 197–204.
- Ji-Seok, S., Jeonghwan, C., Seog-Ju, C., Sungsoo, N., Qin, Z., 2013. Robust aeroelastic instability suppression of an advanced wing with model uncertainty in subsonic compressible flow field. *Aerospace Science and Technology* 25, 242–252.
- Jung, S. N., Nagaraj, V., Chopra, I., 1999. Assessment of composite rotor blade modeling techniques. *Journal of the American Helicopter Society* 44, 188–205.
- Jung, S. N., Nagaraj, V., Chopra, I., 2001. Refined structural dynamics model for composite rotor blades. *AIAA Journal* 39, 339–348.
- Kalman, T., Rodden, W., Giensing, J., 1970. Application of the doublet-lattice method to non-planar configurations in subsonic flow. *Journal of Aircraft* 8, 406–413.
- Kameyama, M., Fukunaga, H., 2007. Optimum design of composite plate wings for aeroelastic characteristics using lamination parameters. *Computers and Structures* 85, 213–224, dOI: 10.1016/j.compstruc.2006.08.051.
- Kaza, K., C.E., H., 1976, May. Investigation of flap-lag stability of wind turbine rotors in the presence of velocity gradients and helicopters in forward flight. 17th Structures, Structural Dynamics, and Materials Conference.
- Kim, C., Bert, C., 1993. Critical speed analysis of laminated composite, hollow drive shafts. *Composites Engineering* 3, 633–644.
- Kussner, H., 1936. Zusammenfassender bericht über den instationären auftrieb von flügeln. *Luftfahrtforsch.*
- Lan, C., 1979. The unsteady quasi-vortex-lattice method with applications to animal propulsion. *Journal of Fluid Mechanics* 93, 747–765.
- Lee, S., Kuo, Y., 1993. Bending frequency of a rotating timoshenko beam with generally elastically restrained root. *Journal of Sound and Vibration* 162, 243–250.
- Librescu, L., Khdeir, A., 1988. Aeroelastic divergence of swept-forward composite wings including warping restraint effect. *AIAA Journal* 26, 1373–1377.
- Livne, E., 2003. Future of airplane aeroelasticity. *Journal of Aircraft* 40, 1066–1092.
- Loewy, R., 1957. A two-dimensional approach to the unsteady aerodynamics of rotary wings. *Journal of the Aeronautical Sciences* 24, 81–92.

- Loewy, R., 1969. Review of rotary-wing v/stol dynamic and aeroelastic problems. *Journal of the American Helicopter Society* 14, 3–23.
- Marzocca, P., Librescu, L., Chiochia, G., 2002. Aeroelastic response of a 2-d airfoil in a compressible flow field and exposed to blast loading. *Aerospace Science and Technology* 6, 259–272.
- Masjedi, P., Ovesy, H., 2014. Aeroelastic instability of composite wings by the consideration of different structural constitutive assumptions. *Journal of Fluids and Structures*In print.
- Mei, C., 2008. Application of differential transformation technique to free vibration analysis of a centrifugally stiffened beam. *Computers and Structures* 86, 1280–1284.
- Mote, C., Nieh, L., 1971. Control of circular-disk stability with membrane stresses. *Experimental Mechanics* 11, 490–498.
- Murakami, H., 1986. Laminated composite theory with improved in-plane responses. *Journal of Applied Mechanics* 53, 661–666.
- Na, S., Librescu, L., Shim, J., 2003. Modeling and bending vibration control of nonuniform thin-walled rotating beams incorporating adaptive capabilities. *International Journal of Mechanical Sciences* 45, 1347–1367.
- Na, S., Yoon, H., Librescu, L., 2006. Effect of taper ratio on vibration and stability of a composite thin-walled spinning shaft. *Thin-Walled Structures* 44, 362–371.
- Neves, A., Ferreira, A., Carrera, E., Cinefra, M., Roque, C., Jorge, R., Soares, C., 2012a. Free vibration analysis of functionally graded shells by a higher-order shear deformation theory and a radial basis functions collocation, accounting for through-the-thickness deformations. *European Journal of Mechanics/ A Solids*Accepted Manuscript.
- Neves, A., Ferreira, A., Carrera, E., Cinefra, M., Roque, C., Jorge, R., Soares, C., 2012b. Static, free vibration and buckling analysis of isotropic and sandwich functionally graded plates using a quasi-3d higher-order shear deformation theory and a meshless technique. *Composites: Part B*In press.
- Nguyen, N., 2009. Flight dynamics of flexible aircraft with aeroelastic and inertial force interactions. *AIAA Atmospheric Flight Mechanics Conference* 6045.
- Ormiston, R., 1973. Rotor dynamic considerations for large wind power generator systems. *Proc. Wind Energy Conversion Systems Workshop, National Science Foundation, NSF/RA/W-73-006*.
- Ozge, O. O., Kaya, M. O., 2006. Flapwise bending vibration analysis of double tapered rotating euler-bernoulli beam by using the differential transform method. *Meccanica* 41, 661–670.
- Pagani, A., Petrolo, M., Carrera, E., 2014. Flutter analysis by refined 1D dynamic stiffness elements and doublet lattice method. *Advances in Aircraft and Spacecraft Science* 1.
- Palacios, R., Epureanu, B., 2011. An intrinsic description of the nonlinear aeroelasticity of very flexible wings. In *Proceedings of the 52nd AIAA/ASME/ASCE/AHS/ASC Structures, Structural Dynamics and Materials Conference, Denver, Colorado*.

- Patil, M., 1997. Aeroelastic tailoring of composite box beams. In Proceedings of the 35th Aerospace Sciences Meeting and Exhibit, Reno, Nevada.
- Petrolo, M., 2011. Advanced aeroelastic models for the analysis of lifting surfaces made of composite materials. Ph.D. Dissertation.
- Petrolo, M., 2012. Advanced 1D structural models for flutter analysis of lifting surfaces. *International Journal of Aeronautical and Space Sciences* 13.
- Petrolo, M., 2013. Flutter analysis of composite lifting surfaces by the 1d carrera unified formulation and the doublet lattice method. *Composite Structures* 95, 539–546, doi: 10.1016/j.compstruct.2012.06.021.
- Petrolo, M., Zappino, E., Carrera, E., 2012. Refined free vibration analysis of one-dimensional structures with compact and bridge-like cross-sections. *Thin-Walled Structures* 56, 49–61, doi: 10.1016/j.tws.2012.03.011.
- Piccione, E., Bernardini, G., Gennaretti, M., 2010. A finite element model for structural and aeroelastic analysis of rotary wings with advanced blade geometry. Proceedings of the COMSOL Conference 2010 Paris.
- Qin, Z., Librescu, L., 1985. Flutter and divergence aeroelastic characteristics for composite forward swept cantilevered wing. *Journal of Aircraft* 22, 1001–1007.
- Qin, Z., Librescu, L., 2003. Aeroelastic instability of aircraft wings modelled as anisotropic composite thin-walled beams in incompressible flow. *Journal of fluids and structures* 18, 43–61.
- Qin, Z., Librescu, L., Marzocca, P., 2002. Aeroelastic instability and response of advanced aircraft wings at subsonic flight speeds. *Aerospace Science and Technology* 6, 195–208.
- Ramezani, S., Ahmadian, M., 2009. Free vibration analysis of rotating laminated cylindrical shells under different boundary conditions using a combination of the layerwise theory and wave propagation approach. *Transaction B: Mechanical Engineering* 16, 168–176.
- Rao, J., 1985. *Rotor Dynamics*. Wiley Eastern, Delhi, India.
- Rao, S., Gupta, R., 2001. Finite element vibration analysis of rotating timoshenko beams. *Journal of Sound and Vibration* 242, 103–124.
- Rasmussen, F., Hansen, M.H., Thomsen, K., Larsen, T., Bertagnolio, F., Johansen, J., Madsen, H., Bak, C., Hansen, A., 2003. Present status of aeroelasticity of wind turbines. *Wind Energy* 6, 213–228, doi: 10.1002/we.98.
- Raville, M., Ueng, E.-S., Lei, M.-M., 1961. Natural frequencies of vibration of fixed-fixed sandwich beams. *Journal of Applied Mechanics* 83, 367–371.
- Rodden, W., 2012. *Theoretical and Computational Aeroelasticity*. Crest Publishing.
- Rodden, W., Taylor, P., McIntosh Jr., S., 1998. Further refinement of the subsonic doublet-lattice method. *Journal of Aircraft* 35, 720–727.
- Sheu, G., Yang, S., 2005. Dynamic analysis of a spinning rayleigh beam. *International Journal of Mechanical Sciences* 47, 157–169.

- Singh, S., Gupta, K., 1996. Composite shaft rotordynamic analysis using a layerwise theory. *Journal of Sound and Vibration* 191, 739–756.
- Sino, R., Baranger, T., Chatelet, E., Jacquet, G., 2008. Dynamic analysis of a rotating composite shaft. *Composite Science and Technology* 68, 337–345.
- Song, O., Librescu, L., 1997a. Anisotropy and structural coupling on vibration and instability of spinning thin-walled beams. *Journal of Sound and Vibration* 204, 477–494.
- Song, O., Librescu, L., 1997b. Structural modeling and free vibration analysis of rotating composite thin-walled beams. *Journal of the American Helicopter Society* 42, 358–369.
- Song, O., Librescu, L., Jeong, N.-H., 2000. Vibration and stability of pretwisted spinning thin-walled composite beams featuring bending-bending elastic coupling. *Journal of Sound and Vibration* 237, 513–533.
- Song, O., Oh, S., Librescu, L., 2002. Dynamic behavior of elastically tailored rotating blades modeled as pretwisted thin-walled beams and incorporating adaptive capabilities. *International Journal of Rotating Machinery* 8, 13–25.
- Srinivasan, A., Lauterbach, G., 1971. Traveling waves in rotating cylindrical shells. *Journal of Engineering for Industry* 93, 1229–1232.
- Stoykov, S., Ribeiro, P., 2013. Vibration analysis of rotating 3d beams by *p*-version finite element method. *Finite Elements in Analysis and Design* 65, 76–88.
- Theodorsen, T., 1935. General theory of aerodynamic instability and the mechanisms of flutter. N.A.C.A. report 496.
- Tsai, M. H., Lin, W. Y., Hsiao, K. M., 2011. Investigation on steady state deformation and free vibration of a rotating inclined Euler beam. *International Journal of Mechanical Sciences* 53, 1050–1068.
- Varello, A., Carrera, E., Demasi, L., 2011. Vortex lattice method coupled with advanced one-dimensional structural models. *Journal of Aeroelasticity and Structural Dynamics* 2.
- Varello, A., Lamberti, A., Carrera, E., 2013. Static aeroelastic response of wing-structures accounting for in-plane cross-section deformation. *International Journal of Aeronautical and Space Sciences* 14.
- von Karman, T., Burgers, J., 1943. General aerodynamic theory of perfect fluids. *Aerodynamic Theory II*, originally published in 1934.
- Wang, H., Williams, K., Guan, W., 1998. A vibrational mode analysis of free finite-length thick cylinders using the finite element method. *Journal of Vibration and Acoustics* 120, 371–377.
- Wu, C., Kuo, C., 2013. A unified formulation of pvd-based finite cylindrical layer methods for functionally graded material sandwich cylinders. *Applied Mathematical Modelling* 37, 916–938, doi: 10.1016/j.apm.2012.03.025.
- Yoo, H. H., Lee, S. H., Shin, S. H., 2005. Flapwise bending vibration analysis of rotating multi-layered composite beams. *Journal of Sound and Vibration* 286, 745–761.

- Yuan, C., Friedmann, P., 1995. Aeroelasticity and structural optimization of composite helicopter rotor blades with swept tips. NASA report.
- Yurkovich, R., 2003. Status of unsteady aerodynamic prediction for flutter of highperformance aircraft. *Journal of Aircraft* 40, 832–842.
- Zhao, X., Liew, K., Ng, T., 2002. Vibrations of rotating cross-ply laminated circular cylindrical shells with stringer and ring stiffeners. *International Journal of Solids and Structures* 39, 529–545.
- Zinberg, H., Symmonds, M., 1970. The development of an advanced composite tail rotor drive-shaft Presented at 26th Annual National Forum of American Helicopter Society, Washington, DC.
- Zorzi, E., Giordano, J., 1985. Composite shaft rotor dynamic evaluation. ASME paper no. 85, 1–8 Presented at ASME Design Engineering Conference on Mechanical Vibrations and Noise.

Curriculum Vitae

Personal Information

Name	Matteo
Surname	Filippi
Date of Birth	October 13, 1984
Place of Birth	Cuneo, Italy
Nationality	Italian

Education

- 2012 - Present - **PhD in Fluid Dynamics**, Politecnico di Torino, Turin, Italy. PhD Topic: Aeroelasticity.
- 2009 - 2011 - **MSc in Aerospace Engineering**, Politecnico di Torino, Turin, Italy. Master variant: Aerospace Structures. Thesis title: *Advanced one-dimensional models for the analyses of reinforced shell structures*.
- 2003 - 2009 - **BSc in Aerospace Engineering**, Politecnico di Torino, Turin, Italy. Thesis title: *Structural study of a propeller*.

Publications

International Journals and Book Chapters

- E. Carrera **M. Filippi** (2015) "Vibration analysis of thin/thick, composites/metallic spinning cylindrical shells by refined beam models", *Journal of Vibration and Acoustics - ASME DC*, DOI: <http://dx.doi.org/10.1115/1.4029688>, Accepted Manuscript.
- **M. Filippi**, E. Carrera, A.M. Zenkour (2014) "Static Analyses of FGM Beams by Various Theories and Finite Elements", *Composites: Part B*, Vol. 72, pp. 1–9. DOI: <http://dx.doi.org/10.1016/j.compositesb.2014.12.004>.
- **M. Filippi**, E. Carrera (2014) "Aerodynamic and mechanical hierarchical aeroelastic analysis of composite wings", *Mechanics of Advanced Materials and Structures*, In press.

- E. Carrera , **M. Filippi**, P.K. Mahato, A. Pagani(2014) “Advanced models for free vibration analysis of laminated beams with compact and thin-walled open/closed sections”, *Journal of Composite Materials*, <http://10.1177/0021998314541570>.
- E. Carrera , **M. Filippi**(2014) “Variable Kinematic one-dimensional finite elements for the analysis of rotors made of composite materials”, *Journal of Engineering for Gas Turbines and Power - ASME DC*, Vol. 136.
DOI: <http://dx.doi.org/10.1115/1.4027192>.
- D.S. Mashat, E. Carrera, A.M. Zenkour, S.A. Al Khateeb, **M. Filippi** (2014) “Free Vibration of FGM Layered Beams by Various Theories and Finite Elements”, *Composites: Part B*, Vol. 59, pp. 269–278.
DOI: <http://dx.doi.org/10.1016/j.compositesb.2013.12.008>.
- E. Carrera , **M. Filippi**, E. Zappino (2013) “Free vibration analysis of laminated beam by polynomial, trigonometric, exponential and zig-zag theories”, *Journal of Composite Materials*.
DOI:<http://dx.doi.org/10.1177/0021998313497775>
- E. Carrera , **M. Filippi**, E. Zappino (2013) “Laminated beam analysis by polynomial, trigonometric, exponential and zig-zag theories”, *European Journal of Mechanics A/Solids*, Vol. 41, pp. 58–69.
DOI:<http://dx.doi.org/10.1016/j.euromechsol.2013.02.006>
- E. Carrera , **M. Filippi**, E. Zappino (2013) “Free vibration analysis of rotating composite blades via Carrera Unified Formulation”, *Composite Structures*, Vol. 106, pp. 317–325.
DOI:<http://dx.doi.org/10.1016/j.compstruct.2013.05.055>
- E. Carrera , **M. Filippi**, E. Zappino (2013) “Analysis of Rotor Dynamic by One-Dimensional Variable Kinematic Theories”, *Journal of Engineering for Gas Turbines and Power - ASME DC*, Vol. 135(9).
DOI:<http://dx.doi.org/10.1115/1.4024381>
- E. Carrera , **M. Filippi**, E. Zappino (2012) “Free Vibration Analysis of Thin-Walled Cylinders Reinforced With Longitudinal and Transversal Stiffeners”, *Journal of Vibration and Acoustics - ASME DC*, Vol. 135(1).
DOI:<http://dx.doi.org/10.1115/1.4007559>

Conference Proceedings

- E. Carrera, **M. Filippi**, A. Pagani, M. Petrolo, E. Zappino (2012) “On the use of refined 1D structural models for reinforced cylinders with ends sealed”, In: *Fifth International Symposium on Design Modeling and Experiments on Adaptive Structures and Smart Systems DeMEASS V*, Ulrichsberg (AUSTRIA), October 28-31, 2012.
- **M. Filippi**, A. Pagani, E. Carrera, M. Petrolo, E. Zappino (2012) “Advanced models for static and dynamic analysis of wing and fuselage structures”, In: *8th Pegasus-AIAA Student Conference*, Poitiers (France), 11-13 April 2012.

- E. Carrera, **M. Filippi**, E. Zappino (2013) "Static and Dynamic Analysis of Composite Beams by 1-D Variable Kinematic Theories", In: *17th International Conference on Composite Structures*, Porto (Portugal), 17-21 April 2013.
- E. Carrera, **M. Filippi**, E. Zappino (2013) "Free Vibration Analysis of Rotating Structures by 1D-Variable Kinematic Theories", In: *Proceedings of the ASME 2013 International Mechanical Engineering Congress & Exposition*, San Diego (California, USA), 15-21 November 2013.
- E. Carrera, **M. Filippi** (2014) "Free Vibration Analysis of Rotating Composite Structures by 1D-Variable Kinematic Theories", In: *Mechanics Composites Conference*, Stony Brook (New York, USA), 08-13 June 2014.
- **M. Filippi**, E. Carrera (2014) "Free Vibration Analysis of Rotating Structures by 1D-Variable Kinematic Theories", In: *11th World Congress on Computational Mechanics WCCM XI*, Barcelona (Spain), 20-25 July 2014.
- **M. Filippi**, E. Carrera (2014) "Capabilities of 1D CUF-based models to analyze metallic/composite rotors", In: *8th Australian Congress on Applied Mechanics, ACAM8*, Melbourne (Australia), 23-26 July 2014.
- E. Carrera, **M. Filippi**, P.K. Mahato and A. Pagani (2014) "One-dimensional CUF models for the analysis of laminated structures", In: *8th Australian Congress on Applied Mechanics, ACAM8*, Melbourne (Australia), 23-26 July 2014.